CHAPTER

SEVEN

TEMPERATURE FIELD MEASUREMENT IN BUOYANCY-DRIVEN FLOWS USING INTERFEROMETRIC TOMOGRAPHY

K. Muralidhar

ABSTRACT

Optical methods of measurement are known to have specific advantages in terms of spanning a field-of-view and being inertia-free. Though in use for over half a century, optical methods have seen a resurgence over the past decade. The main factors responsible are the twin developments in the availability of cost-effective lasers along with high-performance computers. Laser measurements in thermal sciences have been facilitated additionally by the fact that fluid media are transparent and heat transfer applications in fluids are abundant. Whole-field laser measurements of flow and heat transfer in fluids can be carried out with a variety of configurations: shadowgraph, schlieren, interferometry, speckle, and PIV, to name a few. In the present review, temperature field measurements in fluids by laser interferometry has been addressed.

The ability to record interferograms on a PC using CCD cameras has greatly simplified image analysis. It is possible to enhance image quality and perform operations such as edge detection and fringe thinning by manipulating the numbers representing the image. Image analysis techniques have also been discussed in the present article.

When combined with holography, laser interferometry can be extended to map three-dimensional fields. Holographic interferometry can be cumbersome in some applications due to the need of holographic plates, particularly when large regions have to be scanned. This difficulty is circumvented by using an analytical technique called tomography. Here the interferograms are viewed as projection data of the thermal field. The three-dimensional field is then reconstructed by suitable algorithms. In principle, tomography can be applied to a set of projection data recorded by shadowgraph, schlieren, interferometry or any of the other configurations. The present review covers tomography applied to interferograms recorded with a Mach–Zehnder interferometer.

As applications, several buoyancy-driven flow experiments have been discussed.

NOMENCLATURE

c_0	speed of light in vacuum
d	wavelength of the roll pattern
f	function to be reconstructed
g	acceleration due to gravity
h	height of the cavity
H	height of the heater block
L	distance traversed by the laser beam through the test cell
M	number of pixels
N	number of rays
Nu	Nusselt number (line-of-sight and surface averaged)
n	refractive index of the fluid
p	experimental projection data
$\tilde{p}$	numerically computed projection data
PL	optical path length traversed by the light ray
Pr	Prandtl number of the fluid, (ν/α)
r	radial coordinate
R	spatial frequency in the CBP algorithm
Ra	Rayleigh number
s	in-plane coordinate required for projections other than 0 and 90°.
T	temperature
ΔT_ε	temperature difference between successive fringes
W	total value of weight function along a ray
w_{ij}	weight function computed on a local grid for the i-th ray and j-th pixel
x, y, z	Cartesian coordinates, with z parallel to the direction of propagation of light
α	thermal diffusivity of the fluid (also, the angle of refraction)
β	coefficient of volume expansion of the fluid
γ	wavenumber, $2\pi d/h$
λ	wavelength of the laser
μ	relaxation factor
ν	kinematic viscosity of the fluid
ϕ	polar angle in the CBP algorithm
τ	dimensionless time period of flow oscillation
θ	projection angle

Subscripts

avg	average of the three-dimensional temperature field along the ray
cold	cold wall
hot	hot wall
i	ray number

ic	ray number of all the rays passing through the j-th pixel
j	pixel number
ref	ambient reference temperature

Superscript

k	iteration number

1 INTRODUCTION

Nonintrusive techniques are being extensively used in engineering measurements. These techniques employ radiation sources as probes. All radiation-based measurements share a common feature in that they generate images of a cross-section of the physical domain. This is to be contrasted with mechanical probes which are concerned with measurements at a point in space and can accomplish this task only after the field to be studied has been physically perturbed. Radiation methods are also inertia-free. Hence, the scanning of a cross-section of the physical region using radiation-based probes results in a large volume of information with practically no time delay.

1.1 Applications

Laser-based optical techniques have reached a high degree of maturity. Optical methods such as laser Doppler velocimetry and particle image velocimetry have replaced traditional methods such as pitot tubes and hot-wire anemometry. Flow visualization methods of the past have evolved to a point where it is now possible to gain qualitative as well as quantitative understanding of the flow and transport phenomena. Sophisticated measurement techniques such as Rayleigh and Mie scattering for temperature and concentration measurements and Raman spectroscopy for detection of chemical species in reacting flows are routinely employed in engineering research. Using satellite radar interferometry, orbiting instruments hundreds of kilometers away in space, can detect subtle buckling of the earth's crust and thus detect minerals and oil and predict volcanic eruptions. Integrating techniques of photography and video recording, digital image processing, optics and color measurement, it is now possible to map the fluid surface slopes of oceans, rivers and lakes optically into a color space. Using reconstruction techniques, the surface elevations can then be back-calculated. If the fluid surface is relatively flat, the spectrum of the reflected light contains rich information about the temperature variation over it. Radiation-based measurements form the backbone of satellite instrumentation, weather prediction programs and defence weaponry.

Buoyancy-driven convection is encountered in a large number of engineering applications such as cooling of electronic equipment, solar ponds, stratified fluid layers in water bodies, and materials processing to name a few. Studying convection

patterns is also of importance in nuclear power plants. Specific examples include passive heat removal in advanced reactor systems, stratification phenomena in steam vessels in which hot and cold water streams mix, and thermal pollution in reservoirs. The liquid metal pools in fast breeder reactors is also subjected to stratification.

Measurements of the shape of the fluid surface and temperature distribution over it are critical for studies of near surface dynamics. There has long been interest in understanding the behavior of short surface wind waves because of their importance in mass, momentum, and energy exchanges at the air-sea interface, in microwave remote sensing of the sea surface, and in the theory of wave-wave interactions. Associated problems of great interest are (a) the interaction of a free vortex with the free surface, (b) behavior of turbulence near the free surface, and (c) the effect of a variable surface tension on the shape of the free surface. A free vortex approaching the free surface may deform the surface and cause the vortex line to be connected to it. Thus, bursts originating from the lower heated wall can modify the air-water interface and significantly alter the local transport rates.

A special application where laser optics can be profitably used is growth of a crystal from its supersaturated aqueous solution. Crystals with a high degree of perfection are required for important and sensitive high-technology applications. Examples are the semiconductor industry for making computer chips and optically transparent materials for making high-power lasers. Growing methods for high-quality crystals include melt growth, flux growth, and solution growth. Each of the crystal-growing processes is determined by principles of physico-chemical hydrodynamics and is extraordinarily complex. To control the process and ensure growth of large high-quality crystals, it is important to understand the physical phenomena involved during crystal growth. These include all modes of heat transfer, phase change, interfacial transport, and turbulence in complex geometries. Hence, there is a need to understand the thermofluid mechanics of the crystal growth mechanisms.

Measurements of the temperature and concentration fields around a crystal growing from an aqueous solution, the surface morphology, and the kinetics of major faces of the crystal is a critical engineering application. The crystal is grown in a specially-designed growth cell under controlled temperature conditions. Under growing conditions, spatio-temporal fields of temperature and concentration are setup around the crystal. The growth mechanism of the crystal, as well as its morphology, are intricately linked to the temperature and concentration gradients at the crystal surface. Since these gradients setup a density field as well, the crystal will experience buoyancy-driven fluid motion around it. The solution around the crystal can be optically mapped to generate the full three-dimensional information of the scalar fields. They can be controlled *online* with the objective of enhancing the *in situ* quality of the growing crystal.

1.2 Optical Methods

When the wavelength of the radiation used is in the visible range, the measurement procedure classifies as an *optical technique* and the region being scanned appears on

a screen as an *image* that is visible to the naked eye. In thermal sciences, a revival of optical techniques for temperature and velocity measurements in fluids has occurred. Possible reasons for this development are:

1. Commercially available lasers have a high degree of coherence (both spatial and temporal) and are cost-effective.

2. Optical images can be recorded conveniently through computers and can be processed as a string of numbers through numerical algorithms.

The implications are that coherence generates stable image patterns, which truly reflect the flow behavior, and computer programs now simplify and replace very tiring microscope operations. The image formation can be related to the patterns formed by solid particles suspended in the fluid, attenuation of radiation, scattering or the dependence of reflectivity, and refractive index on temperature. Optical methods that utilize the dependence of *refractive index* of light on quantities such as density, concentration, and temperature can be configured in many different ways. Three available routes are:

1. Shadowgraph, where the reduction in light intensity on beam divergence is employed,

2. Schlieren, where light deflection in a variable refractive-index field is captured, and

3. Interferometry, where the image formation is related to changes in the refractive index with respect to a reference environment.

For a wide class of applications where temperature differences are within certain bounds, interferometry appears to be a versatile tool for accurate measurement of three-dimensional unsteady temperature fields, and with some modification, for velocity fields. Many examples involving free, mixed, and forced convective heat transfer are included in this category. Worth mentioning is the satellite-based imaging of the planetary atmosphere using coherent optics. In this context, issues such as evaluation of model constants in weather prediction codes, and stabilizing these codes using images of the flow field are being addressed.

The author's experience is with a Mach–Zehnder interferometer for studying two-and three-dimensional temperature fields in buoyancy-driven flows with air as the working fluid. Steady as well as slowly evolving fields have been considered. Flow configurations that have been addressed are:

1. Natural convection from a discrete protruding heater mounted on a vertical wall.

2. Rayleigh–Benard convection in a two-dimensional square cavity.

3. Tomographic reconstruction of three-dimensional temperature fields using interferograms.

4. Rayleigh–Benard convection in a horizontal fluid layer at high Rayleigh numbers.

5. Buoyancy-driven convection in axisymmetric geometries.

The Mach–Zehnder interferometer used in the present work employs a 35 mW He-Ne laser and 150 mm (diameter) optics. Interferograms are recorded using a CCD camera with a 512×512 pixel resolution. The camera is interfaced with a PC

through an 8-bit A/D card which digitizes light intensity levels over a range of 0 to 255. Image acquisition is at video rates (50 frames/s).

1.3 Image Processing and Tomography

The fringe patterns produced by the interferometer need to be converted into records of the fluid temperature. This step requires identifying intensity minima within fringes (*fringe thinning*), locating fringe edges (*edge detection*), determining fringe order, and measuring distances between fringes. Since the image is recorded through a computer, these operations can be performed with computer programs. In most real-life experiments, this step is difficult since operations such as locating fringe minima and edges result in ambiguity. One of the factors that causes difficulties in identification is *speckle,* a form of noise. Elaborate procedures must then be employed to remove speckle from the interferometric images. Examples of cleaning strategies are Fourier-filtering using band-pass filters, histogram specification, and Laplacian smoothing.

Let $n(x)$ and $T(x)$ be the refractive index and temperature fields, respectively, in the physical domain being studied. Let n_0 and T_0 be their reference values, as encountered by the reference beam. The interferogram is a fringe pattern arising from the optical path difference

$$\Delta PL = \int (n - n_0) ds \tag{1}$$

which in terms of temperature is

$$\Delta PL = \frac{dn}{dT} \int (T - T_0) ds \tag{2}$$

The integral is evaluated along the path of a light ray. Neglecting refraction effects, this path will be a straight line and the integral evaluation is greatly simplified. As a special case, if the flow field is two-dimensional (say in the x-y plane), then the light beam can be oriented in the z-direction and the equation above reduces to

$$\Delta PL = \frac{dn}{dT} (T - T_0) L \tag{3}$$

where L is the length of the test cell parallel to the direction of the light beam.

In a more general setting, when the temperature field is three-dimensional, recovering $T(x)$ from a single image is not possible. This image can, however, be viewed as a *projection* of the temperature field in the s-direction. If the original field is

three-dimensional, its projection is a field in a dimension reduced by unity, i.e., two for the present case. It is theoretically possible to record a very large number of projections of the test field in many directions and subsequently reconstruct the original temperature function to a good degree of accuracy. This process of three-dimensional reconstruction from two-dimensional projections is called *tomography.*

In practical problems, it is not possible to record too many projections, either due to limitations of the experimental setup or due to cost. A new subject has now evolved which is concerned with reconstruction with only a few views and is called *limited-view tomography.* Some of the popular methods used here are algebraic reconstruction technique (ART), multiplicative algebraic reconstructive technique (MART), and maximum entropy (MENT). These techniques are *iterative* in nature and reconstruct the unknown function over a grid.

1.4 Scope of the Present Work

Laser interferometry is a powerful measurement technique to record temperature fields in a fluid medium. Combined with tomographic algorithms, the method can reconstruct three-dimensional temperature fields. The review covers interferometric measurements, image processing operations for enhancement of interferograms, evaluation of fringe patterns, and limited-view tomographic algorithms. Experimental results for a variety of buoyancy-driven flow problems have also been presented. The paper is organized under the following sections: Review of literature, laser interferometry, Image processing, Data reduction, Computerized tomography, and Applications.

2 REVIEW OF LITERATURE

2.1 Interferometry

Optical methods have been employed sporadically for heat transfer measurements over the past 50 years. The convenience of lasers as light sources and computers for data acquisition and processing has resulted in a resurgence of this technique in the past decade. Recent developments have been summarized in a special issue of *Optics & Laser Technology* (February, 1999) on "Optical Methods and Data Processing in Heat and Fluid Flow". In a more general setting, new and novel measurement technologies can be seen in the proceedings of the biennially held *International Symposium on Flow Visualization* and the *Pacific Symposium on Flow Visualization and Image Processing.* A survey of interferometry as applied to natural convection problems is presented below.

An early review of optical methods in heat transfer has been presented by Hauf and Grigull [1]. Chu and Goldstein [2] have reported a study of turbulent convection in a horizontal layer of water for the classical Rayleigh–Benard problem. Mach–Zehnder interferometer was employed by the workers for flow visualization. Lewis et al. [3] have investigated the development of mixing-layers in laboratory experiments con-

cerning salt-stratified solutions that are initially stable, but are destabilized by a temperature difference in the vertical direction. Goldstein [4] has surveyed optical techniques for flow and temperature measurement. Lauterborn and Vogel [5] have reviewed the status of optical techniques in fluid mechanics. Mayinger [6, 7] has reviewed image forming optical techniques in heat transfer and computer-aided data processing. Tolpadi and Kuehn [8] have reported a computational and experimental study of a three-dimensional temperature field in an asymmetric geometry. The heat transfer problem involves conjugate conduction-convection and the thermal field in both the solid and fluid phases have been visualized using interferometry. These authors have compared the performance of several reconstruction algorithms applied to experimental data against the numerical solution. The Grid method was found to have the greatest accuracy. Naylor and Tarasuk [9] have presented a computational technique for processing interferograms that are seen in buoyancy-driven convection. Muralidhar et al. [10] have studied the transient natural convection in a square cavity in the intermediate Rayleigh number range using a Mach–Zehnder interferometer. Evaluation of interferograms in high-speed compressible flows has been discussed by Bartels–Lehnoff et al. [11]. Chandrasekhara et al. [12] have discussed a high-speed phase-locked interferometry system that has been designed and developed for real-time measurements of dynamic stall flow over a pitching aerofoil. Zhong and Squire [13] have used interferometry to evaluate organized structures in high-speed flow past a circular cylinder. They have reported the similarities between compressible and incompressible wakes as well as similarities in the turbulent structures. Dupont et al. [14] have discussed the use of electronic speckle interferometry for visualizing isotherms as well as streamlines in a Rayleigh–Benard configuration. Dietz and Balkowski [15] have discussed the estimation of refraction errors in two-dimensional supersonic boundary layers. Most recently, optical methods for flow and heat transfer have been reviewed by Lehner and Mewes [16].

2.2 Holographic Interferometry

Mapping of three-dimensional temperature fields can be accomplished using principles of holography. An algorithm for evaluating holographic interferograms has been presented by Aparicio et al. [17]. Applications of holographic interferometry to heat transfer can be seen in the work of Matulka and Collins [18], Shattuck et al. [19], Spatz and Poulikakos [20], and Shen and Poulikakos [21]. Beer [22] has reported interference fringes in growing steam and refrigerant bubbles from a heated surface. Temperature fields within the bubble also have been presented in this work. Faw and Dullforce [23] have investigated convective heat transfer beneath a heated horizontal plate in air using holographic interferometry. The application of tomography to holographic interferometry has been reported by Ostendorf et al. [24]. Bahl and Liburdy [25] have studied three-dimensional temperature reconstruction above a horizontal heated disk in air using holographic interferometry. Computerized holographic measurements in supersonic flow past bluff objects has been discussed by Lanen [26] and Lanen et al. [27]. The author of this article has experienced difficulties with the holo-

graphic route, primarily due to unavailability of the plates necessary for recording holograms. This has led to the route of storing interferograms on computers, followed by a tomographic inversion to recover the three-dimensional temperature field.

2.3 Computerized Tomography

A considerable amount of literature is presently available in the area of tomographic algorithms. These algorithms work with a set of projections of the field being investigated and reconstruct it to a certain degree of approximation [28]. They can be broadly classified as: (a) Transform methods, (b) Series expansion methods, and (c) optimization techniques. The first leads to the explicit calculation of the reconstructed field via the *Radon Transform*. Practical implementation of this method involves the use of convolution integrals and is called the *convolution backprojection* (CBP) algorithm [28]. The second and third are iterative in nature and have been developed with a view towards handling a limited number of projections. In interferometry applied to measurement of temperature fields in fluids, the series expansion method is best suited. Censor [29] has reviewed the series expansion methods in terms of their rate of convergence and accuracy. Gull and Newton [30] have discussed the use of maximum entropy principle in tomographic reconstruction. A method of encoding prior information has been discussed. Verhoeven [31] has reported the performance of state-of-the-art implementation of a MART (Multiplicative Algebraic Reconstruction Technique) algorithm to multidimensional interferometric data. Subbarao et al. [32] have compared ART (Algebraic Reconstruction Technique), MART, and entropy-based optimization algorithms for three-dimensional reconstruction of temperature fields. A detailed error analysis has been presented: The principal finding of their study is that MART gives the best all around performance even with as few projections as two.

2.4 Interferometric Tomography

Snyder and Hesselink [33] introduced the idea of combining holographic optical elements with tomography, thus permitting high-speed, high-resolution flow visualization. In a similar work aimed at recording microsecond events at a high-speed, Zoltani et al. [34] have used a flash X-ray source. Gmitro and Gindi [35] have described an electrooptical device that can perform reconstruction with the CBP algorithm at video-rates. The idea here is to use optical elements to carry out some of the numerical integration needed for three-dimensional reconstruction. Tomography applied to interferometric data can be seen in the work of Faris and Byer [36] for supersonic jets where refraction effects have been accounted for. Snyder [37] has studied species concentration in a co-flowing jet using tomographic interferometry. Liu et al. [38] used speckle photographs to initiate tomographic reconstruction and have applied the method to axisymmetric and asymmetric helium jets. Watt and Vest [39] studied structures of turbulent helium jets in air by recording the path integral images based on the refractive index variation using a pulsed phase-shifted interfer-

ometer. The advantage of this method is that one can record the phase of the light wave as continuous data, rather than discrete fringes. This greatly improves the spatial resolution of the measurement, being the pixel size rather than the fringe spacing. Subsequently, the authors have tomographically reconstructed the helium concentration field. Tomographic measurement techniques and the appropriate reconstruction algorithms suitable for the process industry have been discussed by Mewes et al. [40]. Michael and Yang [41] have discussed three-dimensional reconstruction of the temperature field using an iterative technique. A Mach–Zehnder interferometer was used in this work on Rayleigh–Benard convection with water as the working fluid. Bahl and Liburdy [42] have discussed tomographic reconstruction for a synthetic temperature field. Soller et al. [43] applied iterative tomographic techniques to study interaction of supersonic jets and independently to buoyancy-driven convective flow around a light bulb. They have noted significant advantages in the tomographic approach, particularly when the recorded data is incomplete. Sato and Kumakura [44] developed the dual plate Fourier transform interferometry to improve the spatial resolution of the measurement by introducing a carrier frequency that modulates the usual fringe patterns. This instrument has then been used to map the thermal field in premixed flames.

2.5 Crystal Growth

Optical methods have been employed in crystal growth research for around half a century. The exploitation of lasers as light sources and computers for data acquisition and processing is very recent. Laser-interferometry is evolving as a powerful technique in studying online and *in situ* crystal growth phenomena. This application is of considerable importance because the grown crystals can be used in high-technology applications, i.e., solid-state lasers. The crystal growth technology being referred to here is the growth of crystals from their supersaturated aqueous solution. Once the growth process is initiated, temperature, and concentration gradients are setup in the liquid phase around the crystal. These in turn can lead to buoyancy-driven currents and influence the crystal quality. The objectives behind measurement are then to monitor the flow, thermal and concentration fields in the solution, and also the surface topography of the grown crystal. The thermal and concentration fields can be mapped using refractive index-based techniques; it is interesting to note that the crystal surfaces can be mapped using differences in the geometric path length, as in a Michelson interferometer. A brief survey of laser-interferometry applied to research on fluid mechanics and transport phenomena during crystal growth is presented below.

The observation of growth spirals using phase contrast microscopy (PCM) was first reported by Verma [45]. Similar microscopy studies were carried out by Sunagawa [46] on mineral crystals and summarized later by the author [47]. Extensive work on the surface microtopographic investigations of solution grown crystals using PCM and DICM (differential interference contrast microscopy) has been carried out by Bennema and coworkers [48]. They observed the spirals on crystals

growing from the liquid state. Tsukamoto et al. [49, 50] demonstrated that by combining optical phase contrast microscopy and differential interference contrast microscopy with a conventional TV system, mono-molecular spiral growth steps on crystals can be observed during the growth in aqueous solution. Onuma et al. [51–53] have carried out a study of crystal growth at the microscopic level on barium nitrate and K-alum using Schlieren and Mach–Zehnder interferometry. They studied the effect of buoyancy driven convection and forced flow rate on the microtopography of the crystal growing from solution. Maiwa et al. [54] studied the growth kinetics of faces of barium nitrate crystals using micro-Michelson interferometery in conjunction with the differential interference contrast microscopy. Onuma et al. [55–56] developed a real-time phase shift interferometer, an improvement over the DICM, and applied it to the measurement of the concentration field through a micro-Mach–Zehnder interferometer. Simultaneouly they used a micro-Michelson interferometer to study the growth kinetics. Later Sunagawa [57] reviewed the research carried out by his coworkers on interferometric analysis of crystal grown from the solution.

In addition to the Japanese researchers listed above, the work carried out by Chernov, Rashkovich, and Vekilov and their coworkers in Russia has helped in understanding the mechanisms of solution-grown crystals. Rashkovich et al. [58–64] developed a Michelson interferometer for studying the growth rate, slope of growth hillock, step velocity, and the hydrodynamics of the solution around crystals growing from it. Their experimental setup can be used for studying crystals as small as a few millimeters to as large as several centimeters. Vekilov [65–67] applied Michelson interferometry to the study of KDP and ADP crystal growth kinetics, as well as to understand protein crystal growth mechanisms. Sherwood and his coworkers at Glasgow have also used interferometry for studying crystal growth rates [68–69]. They have used synchrotron X-radiation for assessment of the strain in crystals and its relation to growth rate dispersion.

2.6 Other Techniques

Schlieren and shadowgraph are the other two techniques besides interferometry, that can be used to form images of the thermal field using refractive index changes. The advantages of these methods are a simpler optical configuration, better spatial resolution since the image is an intensity distribution rather than fringes, and suitability for large thermal gradients. The disadvantage arises from the fact that the intensity variation is related to the derivatives of the refractive index field, rather than the refractive index itself. Specifically, a schlieren system can capture the temperature gradient, while a shadowgraph yields the second derivative of the temperature distribution. These distributions can be evaluated in three dimensions, once again by using principles of tomography. The temperature field in principle, can be determined by integrating the gradient field. In practice this can be cumbersome and these two methods continue to be in use primarily for flow visualization. In some problems, the temperature gradient itself may be the primary quantity of interest, for example the local

Nusselt number on a solid wall. The schlieren image generates a visual picture of the local heat transfer rates, and hence, on occasion can be a superior measurement technique in comparison to interferometry. A review of schlieren and shadowgraph techniques can be seen in the edited books of Goldstein [4] and Mayinger [6].

The application of the schlieren technique to problems of practical importance have been reported by the following authors. Kosugi et al. [70] have experimentally recorded gas temperature profiles in the shock region of excimer lasers and correlated them to the xenon concentration in a helium gas. Koreeda et al. [71] have studied shock structures in air at very high Mach numbers (up to 35) using schlieren signals recorded by a split photodiode. Agrawal et al. [72] have developed a color schlieren technique coupled with tomography for measurement of temperature in gas flows. Bystrov et al. [73] report extraction of the density and temperature fields in shock tube experiments using schlieren signals.

Coherent structures in a mixing layer were visualized using shadowgraphy by Brown and Roshko [74] in an early pioneering experiment. Images of shocks in high-speed gas flow can be seen in the exhaustive compilation of Van Dyke [75]. Convective flow in a water-filled square cavity with differentially heated side walls has been visualized by a shadowgraph technique by Schopf et al. [76]. The images have been quantitatively evaluated by comparison to a numerical solution of an identical problem.

Schlieren and shadowgraph are popular measurement techniques in the aerospace industry where qualitative yet reliable information is required on shocks, boundary-layers, and wakes and their interaction.

2.7 Text Organization

In the following sections, principles of laser interferometry, image processing, data analysis, and computerized tomography have been discussed. Interferometric experiments of buoyancy-driven flow have been separately discussed in detail. The discussion in the following sections contains material drawn from Darbhe and Muralidhar [77], Muralidhar et al. [10], Mishra et al. [78], and Mishra et al. [79–82].

3 LASER INTERFEROMETRY

The primary instrument used in the present work for temperature measurement in the fluid medium is the Mach–Zehnder interferometer. Figure 1 is a schematic drawing of the interferometer. The optical components present in it, namely the beam splitters BS1 and BS2 and mirrors M1 and M2, are oriented at an angle of 45 degrees with respect to the laser beam direction. The first beam splitter BS1 splits the incoming collimated beam into two equal parts – the transmitted and the reflected beams. The transmitted beam 2 is labelled as the test beam and the reflected beam 1 as the reference beam. The test beam passes through the physical region where the convection process is in progress. It is reflected by the mirror M1 and recombines with the ref-

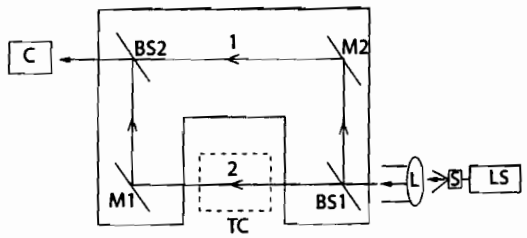

M Mirror
BS Beam splitter
C CCD camera
L Convex lens
LS Laser source
S Spatial filter
1 Reference beam
2 Test beam

Figure 1 Schematic drawing of the Mach–Zehnder interferometer.

erence beam on the plane of the second beam splitter (BS2). The reference beam undergoes a reflection at mirror M2 and passes through the reference medium unaltered and is superimposed with the test beam at, BS2. The two beams on superposition at the second beam splitter BS2, produce an interference pattern. This pattern contains the information of the variation of refractive index in the test region. For measurements in air, the reference medium is simply the ambient. For liquids, a compensation chamber is required to introduce an appropriate reference environment. The mirrors and beam splitters employed in the present configuration are of 150 mm diameter. The beam splitter has 50% reflectivity and 50% transmitivity. The mirrors are coated with 99.9% pure silver and employ a silicon dioxide layer as a protective layer against oxidation.

The Mach–Zehnder interferometer can be operated in two modes, namely the (a) infinite fringe setting, and the (b) wedge fringe setting. In (a) the test and reference beams are set to have identical geometrical path lengths and fringes form due to density, and so temperature, changes alone. (In this discussion, changes in density due to changes in pressure are taken to be of secondary importance; this assumption is valid for many buoyancy-driven flow experiments). Since each fringe is a line of constant phase, it is also a line of constant refractive index, a line of constant density, and hence temperature, and hence an isotherm. It can also be shown that the fringe thickness is an inverse measure of the local temperature gradient, being small where gradients are high. The infinite fringe setting is employed for high-accuracy temperature measurements in the fluid. In (b), the mirrors and beam splitters are deliberately misaligned to produce an initial fringe pattern of straight lines. When a thermal disturbance is introduced in the path of the test beam, these lines deform and represent the temperature profiles in the fluid. The wedge fringe setting is commonly employed for wall heat flux measurements.

The specifications of the components of a Mach–Zehnder interferometer employed by the author are presented below.

Table 1 Specifications of the Helium-Neon Laser

Make	Spectra-physics
Model	Spectra-physics 127
Output power	60 mW (maximum), 35 mW average output
Wavelength	632.8 nm
Color	Orange red
Coherence length	20–30 cm
Power consumption	≈ 0.1 kW of electrical power
Efficiency	0.01–0.1%
Beam diameter	1.25 ± 0.10 mm
Beam divergence	0.66 ± 0.06 mrad
Amplitude noise, 10 Hz–2 MHz	< 1% rms
Amplitude ripple, 45 Hz–1 kHz	< 1% rms
Life time	≈ 20,000 hours of operation

3.1 Laser Source

A 35 mW, continuous wave He-Ne laser ($\lambda = 632.8$ nm) is employed as the coherent light source for the interferometer. This laser is sturdy in construction, economical, and stable in operation. The original laser beam is of 2 mm diameter. A spatial filter along with a convex lens or a concave mirror is required to expand the beam to any convenient size. In the present study, the expanded beam diameter is 70 mm. The spatial filter is a lens-pinhole arrangement with two adjustable screws. The distance between the pin hole and the lens is also adjustable. These screws determine the in-plane location of the pin hole and have to be adjusted so that the small laser beam is focussed on the pin-hole and the outgoing beam is expanded. The specifications of the laser used in the present work are given in Table 1.

3.2 CCD Camera

A CCD (charged coupled device) camera (Pulnix, model: T5 565) of spatial resolution of 512×512 pixels has been used to capture the interferometric images. The fringes formed at the second beam splitter of the Mach–Zehnder interferometer are projected on to a screen. The selection of the screen material and collection of interferometric images from it is an important step. This is because the clarity in the images will reduce the uncertainty in the subsequent calculations. For this purpose, tracing sheet has been used to display the interferometric images in the present work. The attenuation of the laser beam through the thickness of the paper was found to be small. It was observed that two screens used together with one of them physically perturbed led to distinctly clear images on the video monitor. This effect can be understood as a spatial averaging of the image over the two screens which suppresses noise by superposition and makes the fringe pattern clear.

The CCD camera is connected to a PC-based image processing system through an 8 bit A/D card (Pip 1024 Matrox). The fringe pattern is stored in an integer matrix

form with intensities varying between 0 to 255 (the gray scale), where 0 indicates black and 255 indicates white. With the present setup the image acquisition speed is at video rates, namely 50 frames per second. The digital output of the CCD camera is projected to a high-resolution video monitor to visualize, localize, and focus the fringe patterns.

3.3 Pneumatic Isolation Mount

The optical components of the interferometer are extremely sensitive to vibrations. This can be experienced from the movement of the fringes which form on the screen. To avoid ground vibration from reaching the optics, the entire interferometer is placed over four pneumatic isolation mounts. These mounts are connected to an air compressor for pressurization. Once the mounts are pressurized the entire interferometer floats over the mounts. This stabilizes the interferometric images and facilitates image acquisition. An air compressor of rated capacity 10 atmospheres has been used throughout the experiment to pressurize the mounts. The operating pressure for the mounts is 5 kg/cm^2. A regulator valve was used to supply air to the mounts at the right pressure. The compressor in turn was located sufficiently far away from the interferometer to eliminate motor vibrations.

3.4 Alignment of the Interferometer

Before the start of the experiment the interferometer has to be aligned. Though the initial alignment of the interferometer is generally not disturbed from one experiment to the other, periodic fine tuning is essential to ensure that the interferometer is operating at its highest sensitivity. The initial alignment of the interferometer is carried out as per the following steps:

1. The light output of the spatial filter is adjusted so that the diffraction rings, which appear with the expanded beam, vanish. This requires adjustment of the screws on the spatial filter. In most experiments, the diffraction ring formed a complete circle and remained outside the periphery of the expanded beam.

2. The laser-power output is measured using a light meter. The laser-power output is generally not a stable quantity and changes with time. This change in power output is not a transient phenomena. Instead, it decreases steadily with the hours of operation. During the present work, the laser output was in the range 30–32 mW over two years.

3. The convex lens is adjusted from the pinhole of the spatial filter so that the distance of separation is the focal length of the lens. This produces a parallel laser beam needed for the experiments.

4. All the optical components of the interferometer are adjusted until their centers fall on a horizontal plane. Once this is accomplished, the first beam splitter (BS1) is adjusted until it is at 45 degrees to the incoming light rays. All the remaining optical components are then made parallel to one another by turning one at a time. The mirrors and beam splitters being of 150 mm in diameter, the expanded beam of 70 mm diameter is made to pass through the central portion of the optical components.

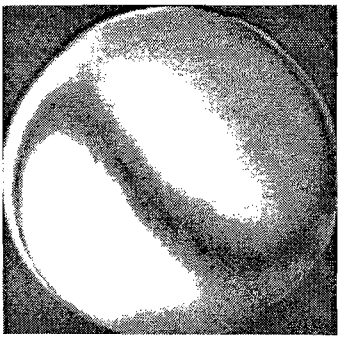

Figure 2 Infinite fringe setting of the interferometer.

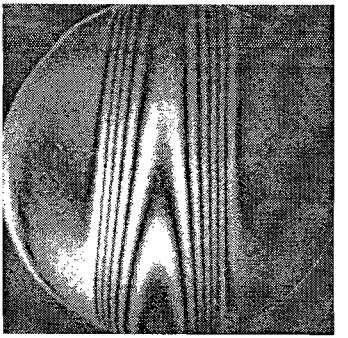

Figure 3 Candle flame in the infinite fringe setting.

5. Adjustment for the infinite fringe setting is delicate and requires effort. In the infinite fringe setting, the initial field-of-view is one of complete brightness since interference is constructive. The geometrical and the optical path lengths of the test and reference beams are then the same in the absence of any thermal disturbances in the path of the test beam. Owing to imperfect adjustment of the mirrors and beam splitters by screws movement, the exact infinite fringe setting in a theoretical sense may not be realized. As the interferometer approaches the infinite fringe setting, the distance between the fringes increases and the number of fringes decreases until the illuminated spot is spanned by one or two broad fringes. In the present work, it was possible to reduce the number of fringes to unity at the start of all the experiments (Fig. 2).

To illustrate fringe formation in the infinite fringe setting, a candle flame was put in the path of the test beam and the interferogram was recorded. The candle flame in

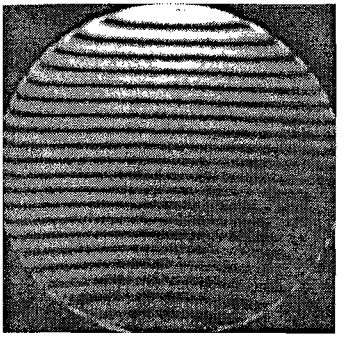

Figure 4 Wedge fringe setting of the interferometer.

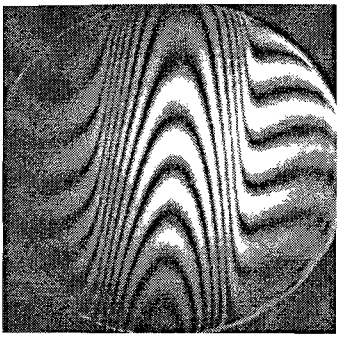

Figure 5 Candle flame in the wedge fringe setting.

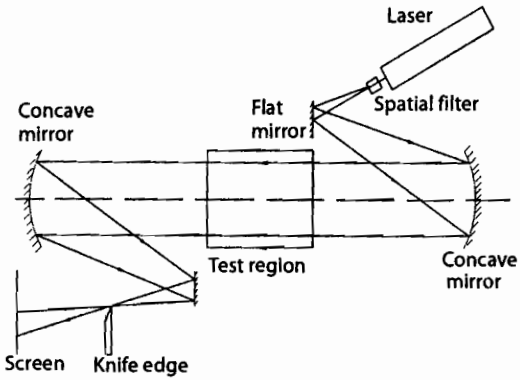

Figure 6 Schematic drawing of a schlieren apparatus.

the infinite fringe setting is shown in Figure 3. The fringes can be seen to correspond to isotherms around the candle flame.

The wedge fringe setting is comparatively easier to setup than the infinite fringe setting. Here the initial fringes form due to deliberate misalignment between the optical components. The orientation of the fringes can be changed by adjusting the inclination of the optical components. Initially the fringes are adjusted so that they are perfectly straight. Figure 4 shows the initial wedge fringe setting of the interferometer. If a thermal disturbance is introduced in the path of the test beam, the fringes get displaced to an extent depending on the nature of the temperature profile. Hence the fringes in the wedge fringe setting of the interferometer are representative of the temperature profile in the fluid medium under study. The candle flame experiment is shown in the wedge fringe setting mode in Figure 5. Here the fringes are the temperature profile inside the flame. Note the symmetry in the temperature profile along the center-line of the flame.

For completeness, the schlieren and shadowgraph configurations are shown in Figures 6 and 7, respectively. A combined Mach–Zehnder and Michelson interferometer for simultaneous measurement of thermal convection and crystal topography is shown in Figure 8.

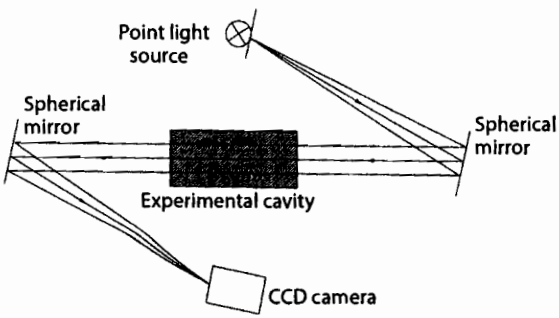

Figure 7 Schematic drawing of a shadowgraph apparatus.

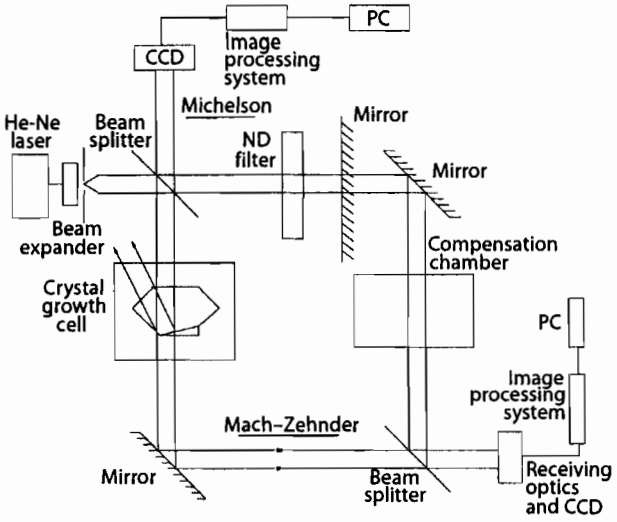

Figure 8 Combined Mach–Zehnder and Michelson interferometry for crystal growth from a solution (courtesy: Sunil Verma, CAT, Indore, India).

3.5 Recording Interferometric Projections

When the method of axial tomography is employed, projection data of the field to be reconstructed has to be recorded from various angles. The experiments with the differentially heated fluid layer (Section 7.3) were conducted by turning the convection test cell with reference to the light source. The position of the light source and the detector remained fixed in all the experiments. The experiments were conducted at various angles and for each angle the full width of the fluid layer was scanned. The width of the fluid layer being 500×500 mm in plan, required several translations with the traversing mechanism to scan the complete fluid width for one projection angle. This is because the diameter of the laser beam was only 70 mm. The data thus recorded in the form of images were joined together using computer programs to generate one complete image corresponding to a given projection angle.

4 IMAGE PROCESSING

The information generated by the Mach–Zehnder interferometer is available in the form of interference fringes. The interferograms contain information about the temperature itself in two-dimensional fields. In three-dimensional problems, interferograms must be recorded at various projection angles and must scan the complete fluid domain. Temperature distribution can subsequently be determined by interpreting the interferometric images as path integrals and applying principles of

three-dimensional reconstruction. Tomographic algorithms are applicable in this context. Tomography falls in the class of inverse techniques and its performance is characterized by a definite dependence on noise levels in the prescribed data. Specifically, errors in data can be amplified during the reconstruction process. It is thus natural to examine the sensitivity of the reconstructed temperature field to uncertainties and errors that are intrinsic to image enhancement operations that required processing the interferograms. For both two- and three-dimensional measurements, the fringe patterns thus have to be analyzed in detail.

One of the operations required most often is the extraction of the fringe skeleton from the dark and bright bands of the fringes. When the interferometer is operated in the infinite fringe setting, the fringes are a set of curves that are the locus of points having an identical path difference. This can be interpreted as follows: For rays having a certain path difference, the corresponding pixels in the interferometric image will have identical light intensity. One of the direct ways to locate a typical locus of points is to connect all minimum intensity pixels within a dark band or the maximum intensity pixels within a bright band. The minimum intensity will appear at a point of complete destructive interference and hence will have a zero intensity. Similarly, a maximum in intensity will appear at a point where interference is constructive.

In experiments, the original as well as partially processed images have superimposed noise. Hence the distribution of intensity across fringes will be ambiguous. Specifically, the minimum intensity will not strictly be a zero and in 8-bit digitization, the maximum will not be 255. Hence the strategy that is preferred is to trace the minima within dark bands and maxima within bright bands, rather than search for points of known intensity. This is the closest approximation that can be achieved in tracking a series of pixels having low-or high-intensities. When a laser is used, one must also take into account the overall Gaussian profile of the light output. Hence, determination of extrema in intensity becomes a local operation in the image domain. Subsequently, the locus of minima or maxima need to be connected within a fringe band across the image, to get a curve on which temperature itself or a temperature-dependent function is a constant.

It is clear that under experimental conditions, only intensity minima can be traced since intensity itself is not precisely defined. In practice, one observes a greater noise level in the high-intensity regions, possibly owing to device saturation in the recording medium. This makes locating intensity maxima a difficult task. Hence, fringe thinning operations referred in the present work are related solely to the location of intensity minima in the dark fringe bands.

Several fringe thinning methods are available in the literature. Most of the fringe tracing algorithms that have been suggested are problem-specific and cannot be accepted as generally valid. A large number of published algorithms are based on edge detection by global thresholding, but these are specific to a class of problems and appear to be inapplicable for interferometric images. In the presence of an non-uniform average level of illumination with superimposed noise, the opinion of the present author is that the task of automatic extraction of the fringe skeleton is difficult. This has been experienced even with the well-behaved fringe tracing algo-

rithms given by Robinson [83] and Krishnaswamy [84] for interferometric fringes and by Ramesh and Singh [85] for photoeleastic fringe patterns. Funnell [86] has suggested an easy to implement, but not a fully automatic, technique to trace the fringes. His method is likely to yield good results for low-quality images. In the present study, an algorithm that is similar in approach has been proposed. This algorithm is automatic in the sense that no user input is required at any intermediate stage of the calculation. It is based on the actual two-dimensional grey-level variations and the fringe skeleton is traced by searching along the minimum intensity direction while simultaneously maintaining connectivity of the points traced.

In the present section, the performance of the fringe thinning algorithms has been evaluated in the context of interferometric images. These images were generated by a Mach–Zehnder interferometer. The experiment performed was one involving Rayleigh–Benard convection. The experiment comprised of a layer of air confined between two horizontal surfaces. The lower surface was heated while the upper surface was cooled, both being maintained respectively at constant temperatures. The vertical side walls that defined the boundaries of the fluid layer were thermally insulated. The temperature differential across the fluid layer led to buoyancy-driven motion, whose pattern could be captured from the fringe patterns. This experiment is described in detail in Section 7.3.

The interferograms represent the projection of the three-dimensional temperature field on to a plane. However, the data contained in them must be transferred to a uniform grid before tomographic algorithms can be applied. Several intermediate steps involving image processing operations have to be performed to reach this stage. To start with, interferograms recorded using the CCD camera contain superimposed noise, speckle being the most significant. While speckle is associated with the optical components of the interferometer, the images also carry thermal noise due to edge effects in the fluid layer. Speckle, as well as thermal noise can be conveniently removed in the Fourier domain by a band-pass filter. An example of the original intensity distribution and that obtained after Fourier-filtering is shown in Figure 9. The filter is two-dimensional and can remove the high-wave number components of the spectra of the light intensity. The resulting image has blurred edges and must be processed further. The image quality of the filtered image has been enhanced by using utilities such as histogram equalization and high-boost image preparation [87].

The present discussion is focussed towards fringe thinning and the associated errors. The thinning operations have been carried out with the filtered and enhanced interferograms. Three different approaches have been adopted in this regard: (a) Search of the minimum intensity points within the dark bands, (b) curve fitting through the centers of the dark band, and (c) freehand tracing of the fringe skeleton using a paintbrush option available in Windows-95. These three methods are discussed below in detail.

The temperatures corresponding to the individual fringes have been computed using the two known wall temperatures and the temperature difference between two successive fringes as discussed in Section 5.3. Refraction errors have been estimated to be quite small in the present experiments. The information available about tem-

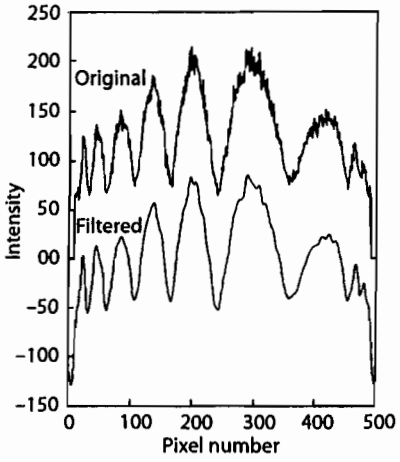

Figure 9 Original and filtered intensity distributions in an interferogram.

peratures at fringe locations has been transferred to a two-dimensional grid by using two-dimensional quadratic interpolation. Interpolation errors have been found to be less than 0.1%. The major source of error between the original interferograms and the data on the interpolated grid was found to be due to fringe thinning alone, other errors owing to filtering for example, being negligible.

The temperature available at this stage for each grid point is a line integral of the temperature field and constitutes the input to the tomographic algorithm. Since refraction errors are small in the present set of experiments, projection data on different horizontal planes can be taken to be independent. Hence, a sequential plane-by-plane reconstruction has been carried out to cover the three dimensions of the cavity. The present discussion on the influence of fringe thinning on tomographic reconstruction is based on two projection angles. Since the number of projections is limited, the algebraic reconstruction technique as against the transform method has been employed. The use of two orthogonal projection angles is not a limitation because these can still be used to determine the overall features of the dependent variable [88]. Subbarao et al. [32] have evaluated the performance of the algebraic reconstruction techniques for interferometric projection data of the temperature field. They have concluded that the multiplicative algebraic reconstruction technique (MART) is best suited in terms of errors and computer time. Hence, in the present work the multiplicative reconstruction technique has been used.

4.1 Fringe Thinning Algorithms

Three fringe thinning algorithms suitable for interferograms recorded using the Mach–Zehnder interferometer are presented in this section. The first is an automatic

technique for fringe thinning using the intensity minima within a dark band and does not require user intervention. This has been compared to two other methods of approximately locating the intensity minima. These are: (1) the midpoint search within a dark band, and (2) paintbrush drawing using a personal computer.

4.1.1 Automatic Fringe Thinning Algorithm. The algorithm under discussion is similar to the one proposed by Funnell [86], but in view of certain differences in the details, the full algorithm is presented below. It consists of tracing of the fringes in the direction of the minimum intensity. The direction is decided by using the intensity information over a template of pixels. The computer code developed in the present study can run using different sizes of templates and handle complex fringe shapes. The input required for the code are the starting points arbitrarily selected for each of the fringes.

The algorithm uses the following ideas. The direction of the tracings are defined as: (a) forward, and (b) backward (Fig. 10). The turning of fringes by more than ±90 degrees results in a change of direction and is a special case. Such areas of the fringes where a turning occurs has to be predefined in the form of a rectangle covering the area. These cases are classified into four categories depending on the angle of turning: (a) while in forward direction turning backward up, (b) while in forward direction turning backward down, (c) while in backward direction turning forward up, and (d) while in backward direction turning forward down (Fig. 11). To locate the point of minimum intensity, eight directions of movement (1–8) are defined (Fig. 12). The direction in which the minima should be searched is located by placing a template whose size is user-specified at the concerned pixel. While the directions of movement are defined on a 3×3 template, the intensity minima are computed independently. The choice of size of the template for minimum intensity calculation is related to the fringe thickness. The near wall fringes in the present study were very thin owing to large heat flux. Hence, the choice of template size was limited to the minimum possible, namely a 3×3 square. Use of a bigger template is likely to interfere with neighboring fringes and is, hence, undesirable. However, a large template can be used when the fringe bands spread over several pixels. Use of a template as

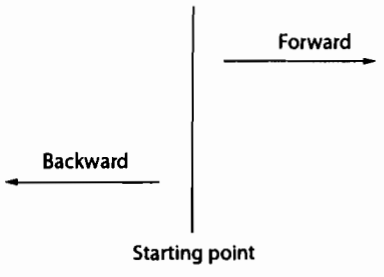

Figure 10 Two major directions for tracing of fringes.

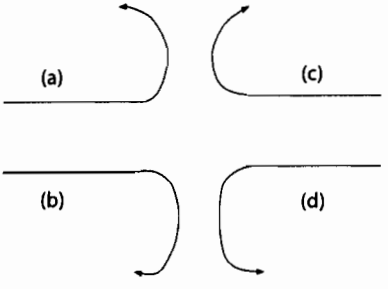

Figure 11 Four possible turning options of fringes.

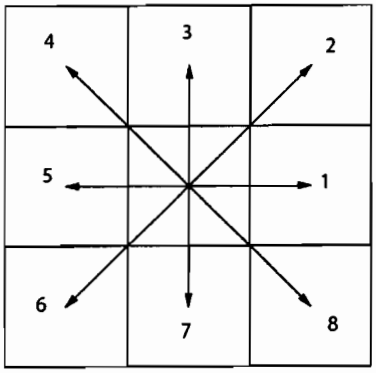

Figure 12 Eight possible directions for movement.

big as 7×7 and 9×9 results in an average direction of minimum intensity and tends to produce a smooth tracing. On the other hand, local unphysical variations can be bypassed by using a large template. Hence a 5×5 template appears to be an optimal choice for interferometric fringes.

The direction in which the fringe is to be traced is determined as follows. The sum of the intensities in each of the eight directions are computed and the two sequences of numbers along which the minima occur are searched. The directions producing the minimum intensity sums are accepted as the minimum intensity directions within a fringe band. One of these is the previous direction already identified. Hence the new direction is the one along which the fringe curve has to be extended. In practice the two intensity sums may not be identical since the average intensity level of the image is not constant. Any given pixel will be connected to two neighboring pixels in a thinned image. Hence the past direction of movement has to be preserved to decide the future connection points. Because of residual noise present in the image, it is likely that a pixel may show two new directions in addition to its last movement. In such a case the sum of intensities that is closer to the previous direction is ignored and the other direction is accepted for the next movement.

The above algorithm can produce loops if precautions are not taken. If a fringe is in the forward tracing mode and the special turning case is not supplied, the fringe is forced to move in the specified direction of (1, 2, 3, 7, and 8) and not (4, 5, and 6), the backward direction (Fig. 12). Similarly in backward tracing, the direction (1, 2 and 8) is not allowed. If one of the directions that is not permissible during forward tracing is encountered as the final direction of movement, a loop-like structure is formed. Tracing may not be completed in some cases. In Funnell's algorithm [86], user intervention is suggested to circumvent the difficulty. In the present work, the ambiguity is resolved by an iterative procedure as described below.

To avoid the formation of loops the nearest forward direction is found iteratively as follows. Once a reverse direction of movement is encountered, the nearest possible direction is adopted in its place. For example, if the direction of movement is 4 while the tracing is in the forward direction, the direction nearest to 4 is 3. Similarly

7 can be replaced by 6. If the direction found is 5, then both 3 and 7 are equally likely. In such a case, the unbiased estimate to 5 is direction 1.

Reallottment of a direction as described above may result in a wrong movement. For example, the direction of movement identified may be one of the previously detected points on the thinned image. In such a case the above steps are repeated and the next closest direction is searched. If the new pixel located falls in one of the four special cases for turning, the image is rotated by 90 degrees in the clockwise direction. Then depending on one of the four cases, one may have to move temporarily in forward or backward directions. During implementation, the code is prepared in a modular fashion to trace forward (to the right) and backward fringes. Rotation of the image enables one of the modules to be used without any change in the marked areas of the fringes.

The boundaries of the image, i.e. the window size are to be prescribed as an input to the computer code. On reaching the boundary, control in the computer code is transferred to the starting point so that the rest of the fringe in the opposite direction can be traced.

The algorithm used for fringe tracing is summarized below:

1. Initialize the thinned image as black (intensity 0).
2. Read the image containing the interferogram including the boundary.
3. Read the starting point data for all the fringes in the image. These points can lie in the interior of the image.
4. Specify the desired template size at the starting point.
5. Specify the initial direction of movement to the left or right.
6. Obtain the intensity sums in the eight directions and find the two minima.
7. Start tracing in the direction of the minimum intensity.
8. At the boundary, transfer control to starting point.
9. Start tracing in the opposite direction until the boundary is reached.
10. Assign a grey level of 255 to the traced pixels.
11. Repeat the process for all the fringes.

Figure 13 shows the thinned image developed using the procedure given above. Both zero and 90 degree projections are shown. Figure 14 shows the superposition of the fringe skeleton and the interferograms and the agreement can be seen to be satisfactory. The fringe immediately adjacent to the top wall (90°) could not be resolved in

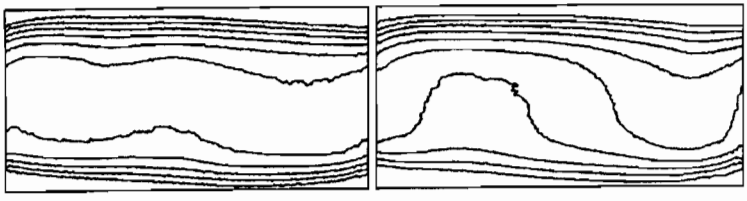

Figure 13 Thinned images, 0° (left) and 90° (right), automatic fringe thinning.

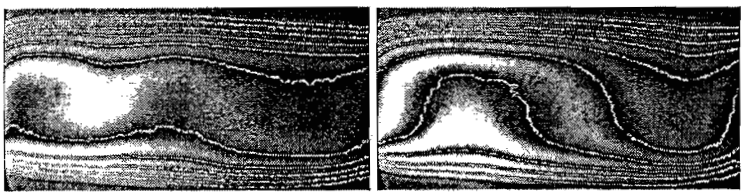

Figure 14 Superimposed thinned images (automatic fringe thinning) with original images, 0° (left) and 90° (right).

the sense that a minimum intensity direction could not be identified in certain parts of the image. This could have been taken care of by manually joining the two segments of the fringe. Instead, the unresolved fringe has been deliberately taken to be lost. As discussed later, this was not seen to introduce errors in the tomographically reconstructed temperature field. A closer evaluation of the thinning process is taken up in Section 4.2.

4.1.2 Curve Fitting Approach. In this method, the intensity minima are assumed to coincide with the center of the fringe bands. Specifically, the variations in the grey levels are not made use of. This is equivalent to the classical microscope route of fringe analysis. A few points within each band are collected using a pixel viewing utility available on workstations. The number of points to be collected over an entire fringe depends on the nature of the function to be fitted through the fringe curve. A greater number of points is chosen in the region of sharp changes in the fringe slope. Relatively fewer points are chosen when the fringe shape varies uniformly or is a constant. In the present work, a cubic spline has been fitted through sets of four points while maintaining slope continuity between adjacent data sets. While this method has the disadvantage of not identifying the minimum intensity location, it does offer certain advantages. These are, thinning of all fringes with no loss and smoothness of the fringe skeleton.

Figure 15 shows the thinned images obtained using the curve fitting approach corresponding to the interferograms in Figure 13. In the interferogram for the 90 degree

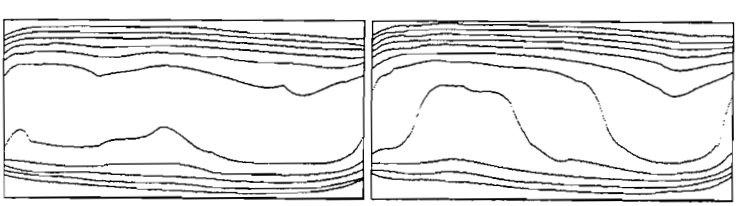

Figure 15 Thinned images, 0° (left) and 90° (right), curve fitting method for fringe thinning.

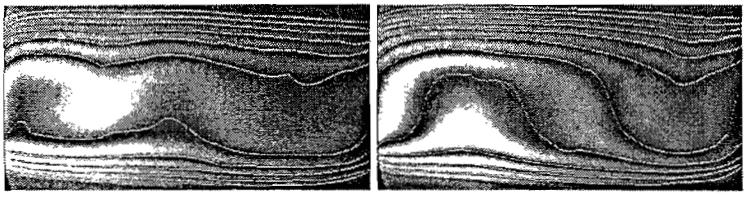

Figure 16 Superimposed thinned images (curve fitting method) with original images, 0° (left) and 90° (right).

projection, an extra fringe can be seen to be captured. This could not be resolved using the automatic fringe thinning approach. Figure 16 shows the thinned images superimposed with the original interferograms. The match is again seen to be good.

4.1.3 Paintbrush Drawing. This is a freehand drawing technique where the midpoints within a dark band of the interferogram are approximately located and joined by a smooth curve. It relies exclusively on eye judgement. The paintbrush utility of the Windows-95 operating system has been employed in this study. The image containing the fringe curves and the original image are subtracted to get the fringe skeleton. Figure 17 shows the thinned images corresponding to the interferograms shown in Figure 13. Owing to the manual user-interactive approach, the 90 degree projection has an extra fringe over the image generated by the automatic thinning method (Figure 13). The superposition of the original interferogram and the fringe skeleton is shown in Figure 18. The paintbrush approach has the disadvantage of not locating the minimum intensity location, but does not require code development and hence is reasonably fast.

4.2 Comparison of Fringe Thinning Algorithms

An implementation of the three thinning algorithms to interferometric fringes reveals the following. The automatic thinning approach is unambiguous and repeat-

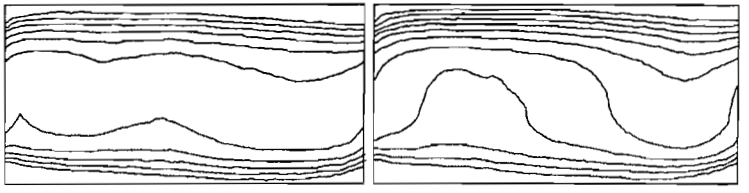

Figure 17 Thinned images, 0° (left) and 90° (right), paintbrush drawing method for fringe thinning.

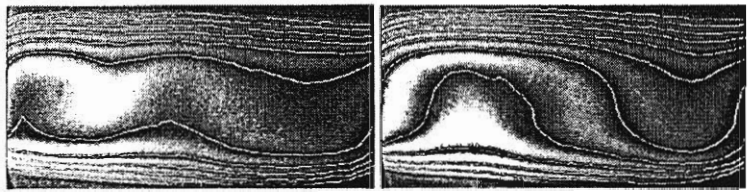

Figure 18 Superimposed thinned images (paintbrush method) with original, images 0° (left) and 90° (right).

able, in the sense that the thinned fringes do not depend on the starting point specified by the user. The curve fitting and paintbrush approaches are sensitive to the user input. On the other hand, they do not require elaborate code preparation time and can be adopted if thinning is only sporadically required.

A preliminary examination of the thinned images (Figs. 14, 16, and 18) shows that the three methods produce qualitatively similar results. An independent assessment of these techniques is taken up in the present section. The first criterion adopted is the comparison of the width-averaged temperature profile for each projection. Under nominally steady conditions, i.e., after sufficient time is allowed to elapse, the width-averaged temperature profile in the fluid plotted as a function of the vertical coordinate can be shown to be independent of the projection angle. This is because the total energy transferred across any horizontal plane in the fluid layer is a constant. These profiles are shown in Figure 19, for all the three algorithms studied. The S-shaped curve, characteristic of buoyancy-driven convection can be seen in this figure. Within experimental limits, a close match between the zero and 90 degree profiles is seen to be realized when the first fringing thinning approach is employed. This match confirms the accuracy of fringe thinning, temperature allocation to fringes (Section 5), and the absence of interpolation errors while transferring the data to a rectangular grid. Figure 19 also shows that the fringe lost during thinning

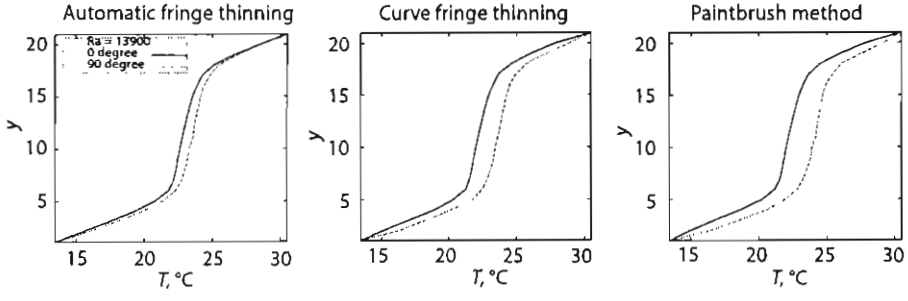

Figure 19 Width-averaged temperature profile of the projection temperature field inside a roll.

near the top wall does not degrade energy balance. The agreement in case of the curve-fitting method is partial, while it is unsatisfactory with the paintbrush method.

The tomographic reconstruction of the temperature field using two projections is considered next. The three fringe thinning algorithms are quantitatively evaluated. The three-dimensional temperature field in the fluid layer has been reconstructed using the MART algorithm. The MART algorithm converged asymptotically to a

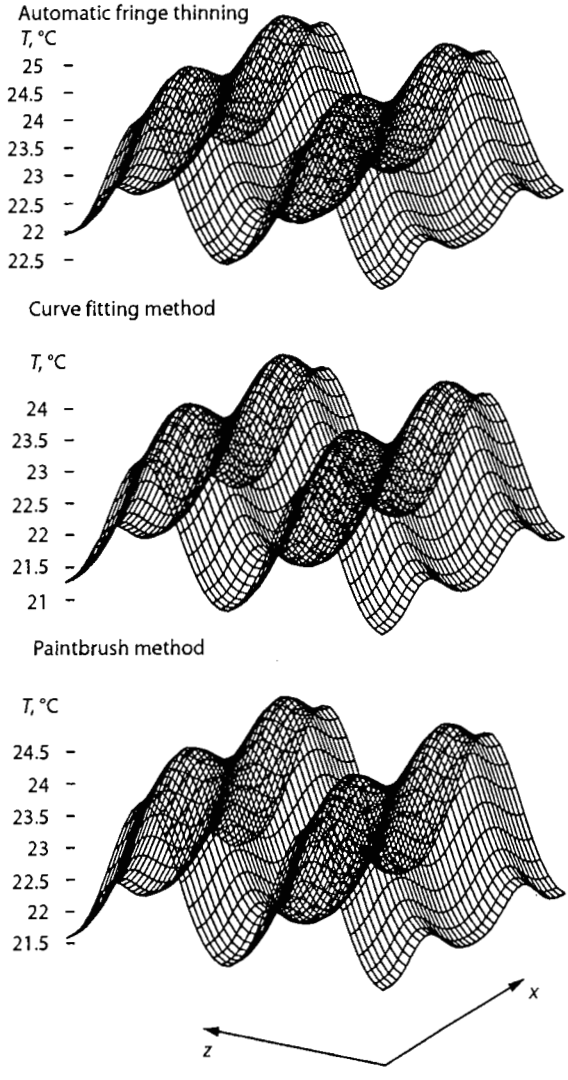

Figure 20 Reconstructed temperature surface within the cavity at the central horizontal plane.

solution for all the three thinning algorithms. Since a correction corresponding to the average of all the rays passing through a pixel was used, a relaxation parameter of unity was used for reconstruction (see Section 6 for details). A convergence criterion of 0.01% between successive updates was employed for stopping the iterations. For each horizontal plane, the number of iterations required was in the range of 30 to 50.

Figure 20 shows the reconstructed temperature surfaces along the central plane for all the three thinning algorithms. These surfaces show the formation of rolls. The rolls show only a minor variation in the x direction and accordingly, may be classified as longitudinal, with the roll axis being parallel to the x coordinate. Qualitatively all the three methods display similar results for the temperature field. The formation of longitudinal rolls can be seen with greater clarity with isotherms. The isotherm plots along the midplane of the fluid layer from the automatic thinning algorithm is shown in Figure 21. The stretching of isotherms in one direction clearly brings out the orientation of the rolls.

A quantitative assessment of the reconstructed temperature field is taken up next. To compute errors, a reference solution is required. Since this is not available for experimental data, the following strategy has been adopted. The temperature field obtained by merging the S-shaped curves in the two projections has been taken as the reference solution. The temperature field thus developed satisfies exactly the energy balance criterion. Errors have been determined between the temperature field developed from the thinning algorithms and the reference solution. Errors reported are the absolute maximum error (E_1, in °C), the RMS error (E_2 in °C) and the percentage RMS error (E_3). The percentage RMS error has been calculated with respect to the temperature difference across the fluid layer. The complete fluid layer has been considered while obtaining these quantities. The errors for each thinning algorithm have been summarized in Table 2.

An examination of Table 2 shows that errors associated with the automatic thinning algorithm are uniformly small. The absolute maximum errors with the other algorithms are larger, being in excess of 1°C. This may not be acceptable in many applications. A comparison of the absolute maximum and RMS errors shows the latter to be

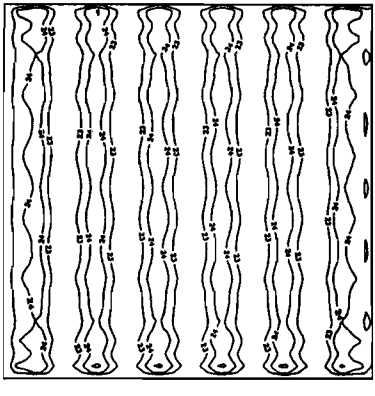

Figure 21 Isotherms on the midplane of the fluid layer.

Table 2 Reconstruction Errors from the Three Fringe Thinning Algorithms

Error	Automatic fringe thinning	Curve fitting method	Paintbrush method
E_1, °C	0.034	1.51	1.03
E_2, °C	0.011	0.60	0.34
E_3, %	0.066	3.51	2.01

smaller, by more than a factor of two. This suggests that large errors are localized over the flow field. The percentage RMS error is truly small for the automatic thinning algorithm, while it is in the range 2–3.5% for the curve fitting and paintbrush methods. This range may still be acceptable in engineering measurements.

The extent to which large errors are localized over a plane of the fluid layer has been examined next. To this end, the percentage fractional area over which a range of error values are to be found, has been computed (Table 3). Error bands considered are 95–100%, 75–95%, and 50–75% of the maximum errors. All three algorithms show that the largest error are confined to only a small area, being 0.19, 0.43, and 0.24 percent respectively, for the three algorithms. This shows that all three thinning algorithms are acceptable in principle. The final choice depends on the need for a high-accuracy measurement on one hand, and the time available for code development on the other.

A comparison of the wall heat transfer rates determined from the temperature field is presented next. The dimensionless form of the heat flux, namely the Nusselt number has been determined in the present study. For reasons discussed below, heat fluxes have been computed over one as well as two roll widths at the wall. The wall heat flux is simply the gradient of the field temperature in the near-wall region. It is possible to define a Nusselt number for each of the hot and cold walls. The average Nusselt number can be computed from the slope of the S-shaped curve shown in Figure 19. For comparison, the benchmark result for Nusselt number has been taken from Gebhart et al. [89]. This reference value is based on a wide variety of experiments reported in the literature and has an uncertainty level of 20%.

Figure 22 shows the local Nusselt number variation with the z-coordinate over one roll for the three thinning algorithms. Both the hot and cold walls have been considered. The view angle is 90 degrees and so the roll formation is visible in this projection. The roll being inclined, the Nusselt number variation on the two walls are of opposite orientation. The three thinning algorithms qualitatively reproduce these

Table 3 Fractional Distribution of the E_1 Error over a Horizontal Plane

Number of points (%) having error in the range	Automatic fringe thinning	Curve fitting method	Paintbrush method
> 95%	0.19	0.43	0.24
75–95%	2.09	0.24	2.0
50–75%	13.4	7.24	4.47

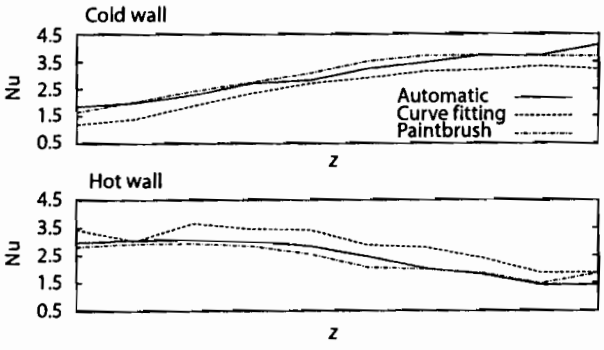

Figure 22 Local Nusselt number variation over the hot and cold plates; comparison of the three thinning algorithms.

trends. The Nusselt number profile predicted by the automatic thinning algorithm can be seen to be the smoothest of the three. Differences among the three algorithms can be seen to have increased in Figure 22, compared to the errors reported in Table 2. This is because the Nusselt number is calculated as the derivative of the temperature field. The local Nusselt numbers calculated from the three algorithms are within ±10% of one another.

Table 4 presents the Nusselt number averaged over a single roll in the fluid layer. The automatic fringe thinning algorithm gives Nusselt numbers that are comparatively close on the two walls. For the zero degrees projection, the average Nusselt number over the two plates differs for both the curve-fitting and the paintbrush methods. The roll in the present study is seen to be formed parallel to the zero degrees axis. There is a considerable mismatch in the average Nusselt number over a single roll as viewed along the 90° projection data. The cavity-averaged Nusselt number, however, is close to the predictions of Gebhart et al. [89].

To stretch the automatic thinning algorithm to a problem of much greater difficulty, the following strategy was adopted. Instead of two, six independent view angles were considered. For each projection, the entire width of the cavity (namely

Table 4 Comparison of Average Nusselt Number Based on the Width of a Single Roll

	Automatic fringe thinning	Curve fitting method	Paintbrush method	Gebhart et al. [89]
0°, cold	2.37	2.01	1.81	
0°, hot	2.38	3.14	3.11	
90°, cold	2.99	2.53	3.02	
90°, hot	2.41	2.88	2.34	
Cavity average	2.53	2.64	2.57	2.59

Table 5 Average Nusselt Number over the Full Width of the Cavity

Projection Angle in Degree	Nu (Cold)	Nu (Hot)	Nu (Average) from all angles
0	2.18	1.94	
30	2.33	2.02	
60	1.99	2.34	
90	2.00	2.17	
120	2.19	2.32	
150	2.27	1.95	
			2.14

500 mm) was scanned. The average Nusselt number obtained for each projection and for each wall is presented in Table 5. The total average Nusselt number seen here is lower than that predicted by the one-roll data. It is however within the experimental uncertainty of the reference value. As a second check on data reduction, experiments were conducted at a Rayleigh number of 40200. The Nusselt number calculated for the entire fluid layer using the automatic thinning algorithm was found to be 3.32. This value is within 3% of the correlation given by Gebhart et al. [89].

4.3 Closure

Three fringe thinning algorithms based on a search for minimum intensity, curve fitting, and the paintbrush option available on PCs have been compared in the context of tomographic inversion. The main conclusions that have been drawn from the present study are:

1. The three methods of fringe thinning produce qualitatively similar temperature fields.

2. Quantitative analysis shows differences in the results, but large errors are localized and over 95% of the fluid region, errors are smaller than 1%.

3. The loss of a wall fringe during the automatic fringe thinning does not increase errors either in the reconstructed temperature field or the Nusselt number.

4. The automatic fringe thinning algorithm requires the most code preparation time. It is however superior to the other two methods since it is repeatable and takes the minimum computer time for execution. It is also physically meaningful since it closely satisfies the energy balance criterion.

5 DATA REDUCTION

Principles of interferometry and the evaluation of interferograms for the determination of fringe temperature are discussed in the present section. It is shown that fringes in the

infinite fringe setting are isotherms when the flow field is two-dimensional. More generally, fringes are isocontours of a path integral function of temperature.

5.1 Interferometry

In the infinite fringe setting, the optical path difference between the test and the reference beam is zero in the absence of any thermal disturbance. Hence interference is constructive and a bright field-of-view is obtained. The image obtained is practically fringe-free, but may show imperfections associated with the spatial filter and the interferometer optics in the form of a single broad fringe. When non-isothermal conditions prevail in the path of the test beam (i.e., a candle flame) each ray of light undergoes a change of phase, depending on the extent of change of the refractive index of the medium. Hence an optical path difference is established between the test and the reference beams, resulting in a fringe pattern. In the wedge fringe setting, the optical components are deliberately misaligned to produce a set of line fringes of any convenient spacing. In the presence of a thermal disturbance the fringes would be displaced towards regions of higher temperatures, thus producing a fringe pattern that resembles the temperature profile itself.

In the present discussion, attention is restricted to image patterns that form in the infinite fringe setting. Here, the test beam records information about the variation of the refractive index of the fluid. To make temperature measurement possible, the refractive index variation must be related to temperature. The relationship between the refractive index n and temperature T is established as follows. For transparent media, the Lorenz–Lorentz relationship

$$\frac{n^2 - 1}{\rho(n^2 + 2)} = \text{constant} \tag{4}$$

holds. For gases, the refractive index is close to unity and the expression reduces to the Gladstone-Dale equation

$$\frac{n - 1}{\rho} = \text{constant} \tag{5}$$

where ρ is density [4]. Hence $dn/d\rho$ = constant. For moderate changes in temperature, typically ≤ 20 K and nearly uniform bulk pressure, density varies linearly with temperature as

$$\rho = \rho_0(1 - \beta(T - T_0)) \tag{6}$$

It follows that dn/dT is also a constant, being purely a material property. Hence changes in temperature simultaneously result in changes in refractive index and from principles of wave optics, lead to changes in the phase of the wave. This is the origin of fringe formation in interferometric images.

If temperature differences within the physical region being studied are large, two factors arise which limit the usefulness of interferometry. These are: (1) the linearity of relationship between density and temperature, and (2) beam deflection due to a refractive index gradient. These factors complicate the data reduction process and make interferometry more of a qualitative tool. However, fringes continue to form and images can be used for flow visualization. In the present study, temperature differences between the test section and the ambient are within 20 K and the linear relation between refractive index and temperature has been taken to be valid.

Let $n(x, y)$ and $T(x, y)$ be the refractive index and temperature fields respectively, the physical domain being a two-dimensional horizontal plane. A three-dimensional region can be visualized as a collection of two-dimensional horizontal planes. Let n_0 and T_0 be the reference values of n and T respectively as encountered by the reference beam. Let L be the total geometric path length covered individually by the test and reference beams. The interferogram is a fringe pattern arising from the optical path difference

$$\Delta PL = \int_0^L (n(x, y) - n_0) ds \tag{7}$$

Differences between $n(x, y)$ and n_0 occur only over the length of the test cell. Hence L can be taken directly to be the length of the test cell. In terms of temperature, the difference in the path length can be expressed as

$$\Delta PL = \frac{dn}{dT} \int_0^L (T(x, y) - T_0) ds \tag{8}$$

The integral is evaluated along the path of a light ray given by the coordinate s. Neglecting refraction effects, this path will be a straight line and the integral evaluation is greatly simplified. The fringes seen on the interferograms are a locus of points having the same optical path difference. Hence on any given fringe the optical path difference ΔPL is a constant and

$$\int_0^L (T(x, y) - T_0) ds = \frac{\Delta PL}{dn/dT} = \text{constant}$$

Hence,

$$\int_0^L T(x, y)ds - T_0 L = \text{constant}$$

The integral $\int_0^L T(x, y)ds$ is defined as $\bar{T}L$, where $\bar{T}$ is the average value of $T(x, y)$ over the length L of the laser beam through the test cell. This is also the line integral of the function $T(x, y)$. Hence

$$L(\bar{T} - T_0) = \text{constant} \tag{9}$$

In the infinite fringe setting Equation (9) holds good for all fringes. When L is constant for all the rays, Equation (9) implies that $\bar{T}$ is a constant over the fringe and hence each fringe represents a locus of points over which the average of the temperature field along the direction of the ray is a constant; in this sense, fringes are isotherms.

Consider a geometry where the length of the ray through the test cell changes for each ray. The line integral of the function $T(x, y)$ $(= \bar{T}_2)$ at a location which corresponds to a length L_2 can be given in terms of the line integral of the function $T(x, y)$ $(= \bar{T}_1)$ at some other location corresponding to a ray length of L_1 as

$$\bar{T}_2 = T_0 + \frac{L_1}{L_2}(\bar{T}_1 - T_0) \tag{10}$$

Since the change in path length per fringe shift is a constant, the temperature drop per fringe shift is also a constant. Defining the function $L(\bar{T} - T_0)$ in Equation (9) as $f(\bar{T}, L)$, the fringe temperature on two successive fringes for same value of L can be given as

$$\text{fringe 1} \qquad f_1(\bar{T}, L) = \frac{\Delta PL}{dn/dT}$$

$$\text{fringe 2} \qquad f_2(\bar{T}, L) = \frac{(\lambda + \Delta PL)}{dn/dT}$$

where λ is the wavelength of the laser used. From these two equations, the temperature change per fringe shift can be calculated as

$$\Delta T_\varepsilon = \frac{1}{L}(f_2(\bar{T}, L) - f_1(\bar{T}, L)) = \frac{\lambda/L}{dn/dT} \tag{11}$$

The interferograms reflect the equation

$$\Delta PL = \frac{dn}{dt}\int_0^L (T - T_0)ds$$

This shows that the fringe patterns contain information about the line integral of the temperature field. The set of all line integrals (an interferogram, in the present study) defines a projection of the temperature field. The interferograms can be numerically processed so that the left side of the above equation is a known quantity. The mathematical problem now is one of solving the temperature field from its projections. If the original field is three-dimensional, its projection is a field in a dimension reduced by unity, i.e., two for the present case. It is theoretically possible to record a large number of projections of the test field at various angles and reconstruct the original temperature function with accuracy. This process of three-dimensional reconstruction from two-dimensional projections, called tomography, is discussed in Section 6.

The above derivation of temperature difference between successive fringes will be modified in the presence of a strong refracting field. In the present context, a strong refracting field will arise when a large transverse temperature gradient is present. The light ray will not travel in a single horizontal plane, and depending on the sign of the temperature gradient, the ray will bend in the vertical plane owing to refraction effects. Refraction, thus will introduce an additional optical path length to the test beam. Refraction effects can be precisely computed and accounted for. The extent of refraction determines the type of the three-dimensional reconstruction algorithm that can be used in a particular experiment. In the present work, refraction errors were found to be negligible and hence a sequential plane-by-plane reconstruction approach was possible.

An estimate of the increase in path length due to refraction is developed here. Following Goldstein [4], consider the path of the light ray AB through a test cell (Fig. 23) when it is affected by the refraction effects. Let α be the bending angle at a location P of the test cell. The optical path length from A to B is given by:

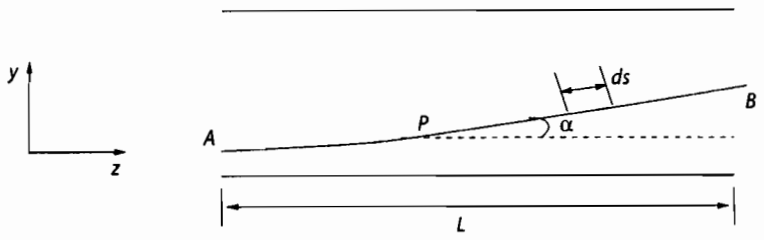

Figure 23 Calculation of bending angle of light ray due to refraction effects.

$$AB = \int_0^L n(x, y, z)ds = \int_0^L n(x, y, z)\frac{ds}{\cos\alpha}$$

Here y is a coordinate parallel to the gravity vector and z is parallel to the direction of propagation of light. Assuming α is small, $\cos\alpha$ can be expressed as

$$\cos\alpha = (1 - \alpha^2)^{1/2}$$

and further using the first two terms of the binomial expansion

$$\cos\alpha \approx 1 - \frac{\alpha^2}{2}$$

Hence the optical path length is given by

$$AB = \int_0^L n(x, y, z)\left(1 - \frac{\alpha^2}{2}\right)^{-1} dz = \int_0^L n(x, y, z)\left(1 + \frac{\alpha^2}{2}\right)dz$$

The angle $\alpha(z)$ at any location z can be calculated as described below.

Consider Figure (24) where two wave fronts at times τ and $\tau + \Delta\tau$ are shown. At time τ the ray is at a position z. After a time interval of $\Delta\tau$, the light has moved a distance of Δz. Hence

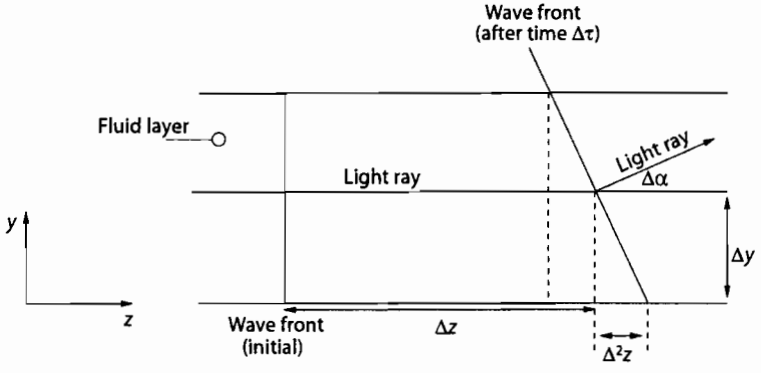

Figure 24 Bending of a light ray in a stratified fluid medium due to refraction.

$$\Delta z = \Delta\tau \frac{c_0}{n}$$

where c_0 is the velocity of light in vacuum. There is a gradient in the refractive index along the y direction. The gradient in n results in a bending of the wave front due to refraction. The distance $\Delta^2 z$ is given by

$$\Delta^2 z = \Delta z_y - \Delta z_{y+\Delta y} \approx \Delta z_y - \Delta z_y + \frac{\Delta}{\Delta y}(\Delta z)\Delta y = -c_0 \frac{\Delta 1/n(x, y, z)}{\Delta y}\Delta\tau\Delta y$$

Let $\Delta\alpha$ represent the bending angle at a fixed location z. For a small increment in the angle, $\Delta\alpha$ can be expressed as

$$\Delta\alpha = \tan(\Delta\alpha) = \frac{\Delta^2 z}{\text{Deltay}} = -c_0 \frac{\Delta 1/n(x, y, z)}{\Delta y}\Delta\tau$$
$$= -n(x, y, z)\Delta z \frac{\Delta 1/n(x, y, z)}{\Delta y}$$

In the limiting case

$$d\alpha = \frac{1}{n(x, y, z)} \frac{\partial n(x, y, z)}{\partial y} dz \tag{12}$$

Hence the cumulative bending angle at any location along the z axis is

$$\alpha(z) = \int_0^z \frac{1}{n(x, y, z)} \frac{\partial n(x, y, z)}{\partial y} dz$$

From Equation (12) the optical path length from A to B is

$$AB = \int_0^L n(x, y, z)\left(1 + \frac{1}{2}\frac{1}{\bar{n}^2}\left(\frac{\partial \bar{n}}{\partial y}\right)^2 z^2\right) dz = \bar{n}(x, y, z)L + \frac{1}{6\bar{n}(x, y, z)}\left(\frac{\partial \bar{n}}{\partial y}\right)^2 L^3$$

where $\bar{n}(x, y, z)$ is the average line integral of $n(x, y, z)$ over the complete length L. Similarly the expressions $1/\overline{6n}$ and $\partial\bar{n}/\partial y$ represent average line integrals over the length L. The optical path length of the reference beam is simply

$$\text{Reference path} = \int_0^L n_0 dz = n_0 L \tag{13}$$

Hence the difference in the optical path length in the presence of refraction effects is

$$\begin{aligned}\Delta PL &= \bar{n}(x, y, z)L + \frac{1}{6\overline{n}(x, y, z)}\left(\frac{\partial \bar{n}}{\partial y}\right)^2 L^3 - n_0 L \\ &= (\bar{n}(x, y, z) - n_0)L + \frac{1}{6\overline{n}(x, y, z)}\left(\frac{\partial \bar{n}}{\partial y}\right)^2 L^3 \\ &= (\overline{T}_1(x, y, z) - T_0)L\frac{dn}{dT} + \frac{1}{6\overline{n}(x, y, z)}\left(\frac{\partial \bar{n}}{\partial y}\right)^2 L^3\end{aligned}$$

where $\overline{T}_1(x, y, z)$ represents the average line integral of the temperature field along the direction of the ray at a given point on the fringe. The corresponding ray over the next fringe traverses an additional distance of λ. Hence this can be written as

$$\Delta PL + \lambda = (\overline{T}_2(x, y, z) - T_0)L\frac{dn}{dT} + \frac{1}{6\overline{n}(x, y, z)}\left(\frac{\partial \bar{n}}{\partial y}\right)^2 L^3$$

where $\overline{T}_2(x, y, z)$ represents the average line integral of the temperature field along the direction of the ray at a point on the next fringe. The successive temperature difference between two fringes can be computed from

$$\begin{aligned}\lambda = (\overline{T}_2(x, y, z) - \overline{T}_1(x, y, z))L\frac{dn}{dT} + \frac{1}{6\overline{n}(x, y, z)}\left(\frac{dn}{dT}\right)^2 \\ \times\left(\left(\frac{\partial T}{\partial y}\bigg|_2\right)^2 - \left(\frac{\partial T}{\partial y}\bigg|_1\right)^2\right)L^3\end{aligned} \tag{14}$$

and the temperature drop per fringe shift is

$$\Delta T_\varepsilon = \frac{1}{Ldn/dT}\left(\lambda - \frac{1}{6\overline{n}(x, y, z)}\left(\frac{dn}{dT}\right)^2\left(\left(\frac{\partial T}{\partial y}\bigg|_2\right)^2 - \left(\frac{\partial T}{\partial y}\bigg|_1\right)^2\right)L^3\right) \tag{15}$$

Since the gradient in the temperature field is not known before the calculation of the fringe temperature the factor $\left(\frac{\partial T}{\partial y}\Big|_2\right) - \left(\frac{\partial T}{\partial y}\Big|_1\right)$ must be calculated from a guessed

temperature field. Thus, the final calculation of ΔT_ε relies on a series of iterative steps with improved estimates of the temperature gradients.

The refraction errors in the present set of experiments can be shown to be quite small. As a conservative estimate, the temperature gradient term can be replaced by its value at the wall. This would give an upper bound on the refraction error. For the following numerical values: $\lambda = 632.8$ nm, $L = 0.5$ m, dn/dT for air at 20°C and 1 bar $= -0.927 \cdot 10^{-6}$ (°C)$^{-1}$ and refractive index of air at 20°C = 1.0, the contribution of the refractive index term in Equation (14) can be evaluated as $2.617 \cdot 10^{-8}$ m. This value is small as compared to the wavelength ($= 6328 \cdot 10^{-8}$ m).

The number of fringes expected in a projection can be estimated directly from the relation

$$\text{Number of fringes} = \frac{T_{\text{hot}} - T_{\text{cold}}}{\Delta T_\varepsilon}$$

This equality was seen to be satisfied in all the experiments reported in the work. This also indicates that refraction errors in the present experiments are negligible.

5.2 Evaluation of Interferograms

The thinned fringes essentially carry the information of the path integrated temperature field. Hence, to extract temperature profiles and heat transfer rates from the interferogram, it is the fringe skeleton rather than the fringe bands that is needed. In the context of three-dimensional reconstruction of the temperature field, the line integral of the temperature field is required over a uniform grid so that tomographic algorithms can be applied. Consequently the calculation of temperature associated with the fringes is an important step in interferometry. The methodology adopted for the calculation of fringe temperature is presented in this section. The technique has been discussed in the context of an experiment with a differentially heated fluid layer (Section 7.3).

For definiteness, consider the fringe skeleton as shown in Figure 25. The upper and lower walls as shown in the figure have known temperatures. It is possible that high temperature gradients near the wall produce a large number of thin fringes. Hence during the recording and processing of the interferogram a few near wall fringes could be lost. The loss of near wall fringes could be due to the finite resolution of the CCD camera, and loss of signal information during filtering and other image processing operations. The first fringe seen in a thinned interferogram near the wall will thus be of arbitrary order. One cannot assign a temperature to the fringes directly from the wall temperature by using Equation (15) though the wall itself is an isotherm. Even when no near-wall fringe is lost, assigning a temperature to the first fringe is not straight-forward since the wall (though an isotherm) need not

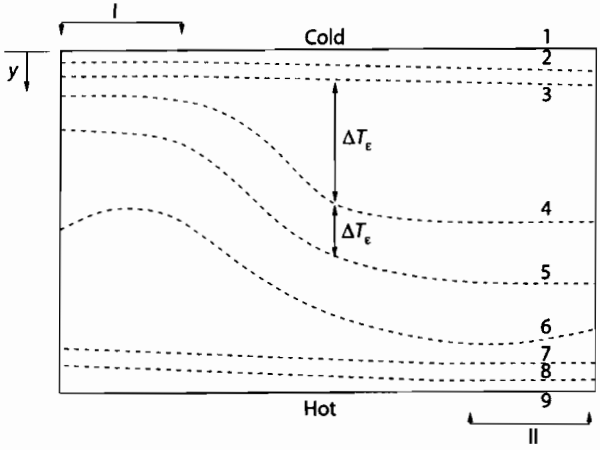

Figure 25 Calculation of the fringe temperature from an idealized fringe skeleton.

be a fringe, i.e., a site for destructive interference. The following procedure has been adopted in the present work to derive temperature values at the fringes.

Over the interferograms, two regions were selected, one where the fringes are close to the cold wall (marked I in Fig. 25) and the other where the fringes are close to the hot wall (marked II in Fig. 25). Two sets of independent calculations were performed to obtain all the fringe temperatures in the interferogram. The estimates of fringe temperature from both regions were found to be within 1%. The fringe temperatures then allotted was the average of the two estimates. Consider the fringes marked 2, 3, 4 (region I, cold wall) in Figure 25. Fitting a function of the type

$$T(y) = a + by + cy^2$$

where y is a vertical coordinate, one obtains

$$\Delta T_\varepsilon = T_2 - T_3 = b(y_2 - y_3) + c(y_2^2 - y_3^2)$$

$$\Delta T_\varepsilon = T_3 - T_4 = b(y_3 - y_4) + c(y_3^2 - y_4^2)$$

These two equations can be solved for the constants b and c. Here, ΔT_ε is the temperature change per fringe shift and y is a local coordinate measured from the upper wall.

The local wall temperature gradient is simply $(\partial T/\partial y)_{y=y_1}$. From Equation (15), this gradient can be expressed as $(b + 2cy_1)$. The gradient in the temperature field

very near the wall is likely to be constant since conduction heat transfer is dominant. Hence the gradient in temperature field at the first fringe (fringe marked 2 in Fig. 25) is expected to be same as the gradient at the wall in region I. The gradient in temperature field at the first fringe is $(b + 2cy_2)$. The wall temperature gradient is allotted as an extrapolation step, the average of the two gradients. Once the gradient at the wall is known, the first fringe temperature near the cold wall can be calculated as

$$T_2 = (y_2 - y_1)\frac{(b + 2cy_1) + (b + 2cy_2)}{0.5} + T_1$$

Since ΔT_ε, the temperature difference between successive fringes is known, the subsequent fringe temperatures are found out by simply adding or subtracting the amount from the first fringe temperature depending upon the sign of the temperature gradient. Since the image is available in the form of a matrix, the above procedure for calculating the fringe temperature can be implemented at any column. The column where the near-wall fringes are dense (as in regions I and II) is preferred for this purpose. Column-to-column variation in the computed fringe temperatures was found to be generally small for the interferograms recorded in the experiments.

5.3 Temperature Data over a Grid

Once the absolute fringe temperatures are obtained, this data must be transferred to a two-dimensional uniform grid over the fluid region. This is required to apply tomographic algorithms for the reconstruction of the three-dimensional temperature field. The data transfer is achieved by interpolation as described below. The nine different points where the fringes intersect the column (Fig. 26) are first mapped to a uniform rectangular grid using a quadratic polynomial as a basis. Temperature at any point (such as *P*, Fig. 26) can be computed by using two-dimensional quadratic interpolation again [90]. Interpolation using a higher order schemes can produce oscillations in the interpolated data. Consequently, the interpolated value in the interior may exceed the values at boundary points and is thus undesirable. Though rare, this may occur when the data spacing is large. In the present study, such overshoot and undershoot have been taken care of by using the idea of universal limiters [91]. The limiter used is one-dimensional in the sense that it is applied only along the vertical direction. Once the interpolated value at a point on the superimposed grid is obtained, its value is compared with the two nearest vertically separated fringes. If the interpolated temperature is outside the range of the two fringe temperatures, the limiter is switched on to force the interpolated value to be one of the temperatures closest to the interpolated value. Interpolation errors in the present work were found to be negligible (< 0.1%).

The collection of thinned images from the Rayleigh–Benard experiment at a 90 degrees projection angle is shown in Figure 27. Interpolation has been carried over the entire image by superimposing a two-dimensional grid on it. The grid has 120

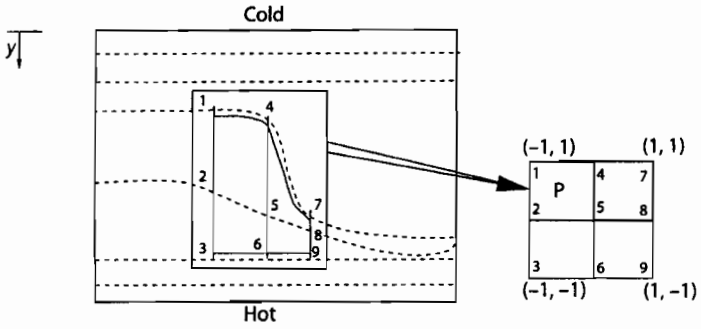

Figure 26 Data transfer from an interferogram to a two-dimensional grid.

points along the horizontal and 21 points along the vertical direction. Once the interpolation is complete isotherms have been drawn to represent the fringes in the original image. This is shown in Figure 28. It can be seen here that the temperature data on the grid follows closely the pattern of the original thinned image and interpolation errors are negligible. The isotherms based on the interpolated grid data are seen to capture the lost fringe in the interferogram as well. Hence the isotherms in Figure 28 show all the fringes with continuity throughout the width of the cavity.

The correctness of fringe thinning, assigning fringe temperatures, and a check on the magnitude of interpolation errors have been examined by using the following result: At steady state, the width-average of the line integrals of temperature field plotted as a function of the vertical coordinate is independent of the projection angle. This is because the total energy transferred across the cavity is unchanged from one horizontal plane to the next. Figure 29 shows the variation of line integrals of the temperature field averaged over a horizontal plane as a function of the vertical coordinate. The line integrals are simply the temperature as computed from the interferograms. The y coordinate is measured from the cold top wall. Both zero and 90 degrees projections have been shown and the Rayleigh number based on the temper-

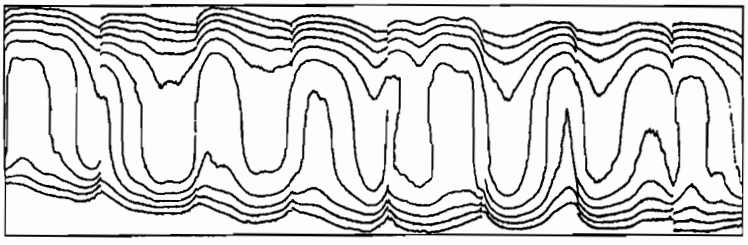

Figure 27 Collection of thinned images.

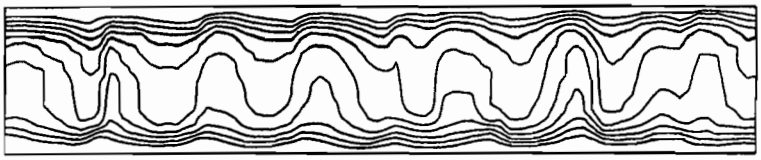

Figure 28 Isotherms obtained from the interpolated data.

ature difference across the fluid layer is 13900. The corresponding graph for Ra = 40200 is shown in Figure 30. The S-shaped curve, characteristic of buoyancy-driven convection can be seen in all the figures. The curves for the two projections match closely and their slopes at the hot and cold walls are practically equal. Temperatures in the zero and 90 degrees data have been subsequently corrected to ensure that between the two projections, the S-shaped curve is strictly unique. This step does not alter the isotherms in the projection data to any significant degree, but is expected to improve the convergence of the tomographic inversion process.

6 COMPUTERIZED TOMOGRAPHY

The three-dimensional temperature field can be reconstructed from its interferometric projections using principles of tomography. Tomography is the process of recovery of a function from a set of its line integrals evaluated along some well-defined directions. In interferometry, the source of light (the laser) and the detector (CCD camera) lie on a straight line with the test cell in between. Further a parallel beam of light is used. This configuration is called *transmission* tomography and the ray configuration as the parallel beam geometry [28]. Tomographic algorithms used in inter-

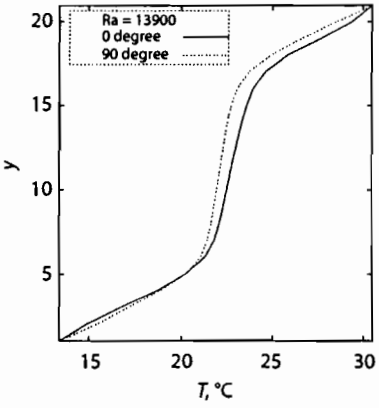

Figure 29 Width-averaged temperature profiles from the interferograms; Ra = 13900.

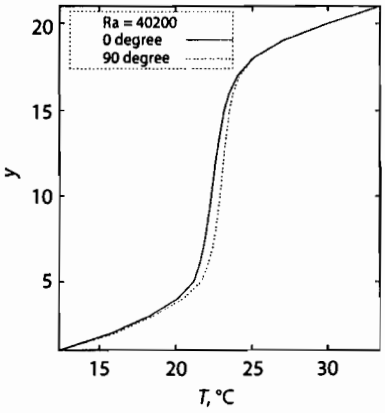

Figure 30 Width-averaged temperature profiles from the interferograms; Ra = 40200.

ferometry reconstruct two-dimensional fields from their one- dimensional projections. Reconstruction is then applied sequentially from one plane to the next until the third dimension is filled.

Tomography can be classified into: (a) transform (b) series expansion, and (c) optimization methods. Transform methods generally require a large number of projections for a meaningful answer [92]. In practice, projections can be recorded either by rotating the experimental setup or the source-detector combination. In interferometry, the latter is particularly difficult and more so with the Mach–Zehnder configuration. With the first option, it is not possible to record a large number of projections, partly owing to inconvenience and partly due to time and cost. Hence, as a rule, a large number of projections cannot be acquired with interferometry and one must look for methods that converge with just a few projections. Limited-view tomography is best accomplished using the series expansion method [29]. As limited-view tomography does not have a unique solution, the algorithms are expected to be sensitive to the initial guess of the field that start the iterations. Optimization-based algorithms are known to be independent of initial guess, but the choice of the optimization functional plays an important role in the result obtained. Depending on the mathematical definition used, the entropy extremization route may yield good results, while the energy minimization principle may be suitable in other applications.

For the algebraic techniques considered in the present study, an unbiased initial guess such as a constant profile was seen to be good enough to predict the correct temperature field. A complete random number guess can also be viewed as an unbiased initial guess. Tomography being an inverse technique, was seen to preserve (and amplify under certain conditions) the noise in the initial data. The dominant trend in the field variable was seen to be however captured during tomographic inversion.

6.1 Convolution Backprojection

The convolution backprojection (CBP) algorithm for three-dimensional reconstruction classifies as a transform technique. It has been used for medical imaging of the human brain for the past several decades. Significant advantages of this method include (a) its noniterative character, (b) availability of analytical results on convergence of the solution with respect to the projection data, and (c) established error-estimates. A disadvantage to be noted is the large number of projections normally required for good accuracy. In engineering applications, this translates to costly experimentation, and nonviability of recording data in unsteady experiments. The use of CBP continues to be seen in steady flow experiments, particularly when the region to mapped is physically small in size. The statement of the CBP algorithm is presented below.

Let the path integral equation be written as

$$p(s, \theta) = \int_C f(r, \phi) dz \tag{16}$$

where p is the projection data recorded in the experiments and f is the function to be computed by inverting the above equation. In practice, the function f is a field variable such as density, void fraction, attenuation coefficient, refractive index, and temperature. The symbols s, θ, r, and ϕ stand for the ray position, view angle, position within the object to be reconstructed, and the polar angle, respectively (Fig. 31). The integration is performed with respect to the variable z along the chord C of the ray defined by s and θ. Following Herman [28], the *projection slice theorem* can be employed in the form

$$\bar{p}(R, \theta) = \bar{f}(R\cos(\theta), R\sin(\theta)) \tag{17}$$

where the overbar indicates the Fourier transform and R is the spatial frequency. In words, this theorem states the equivalence of the one-dimensional Fourier transform of $p(s, \theta)$ with respect to s and the two-dimensional Fourier transform of $f(r, \phi)$ with respect to r and ϕ. A two-dimensional Fourier inversion of this theorem leads to the well-known Radon transform

$$f(r, \phi) = \int_0^{\pi} \int_{-\infty}^{\infty} \bar{p}(R, \theta) \exp(i2\pi R r \cos(\theta - \phi)) |R| dR d\theta$$

where

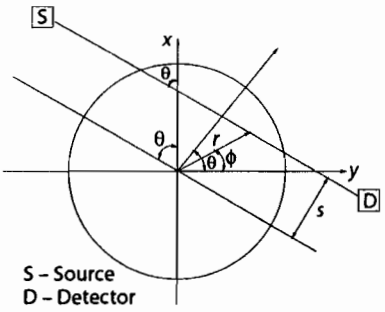

Figure 31 Nomenclature for the convolution backprojection algorithm.

$$\bar{p}(R, \theta) = \int_{-\infty}^{\infty} p(s, \theta) \exp(-i2\pi Rs) ds$$

The first integral in the form given above is divergent with respect to the spatial frequency R. Practical implementation of the formula replaces $|R|$ by $W(R)|R|$, where W is a window function that vanishes outside the interval $[-R_c, R_c]$. The cut-off frequency R_c can be shown to be inversely related to the ray-spacing for a consistent numerical calculation of the integral. When the filter is purely of the band-pass type, the Radon formula can be cast as a convolution integral [93]:

$$f(r, \phi) = \int_{0}^{\pi} \int_{-\infty}^{\infty} p(s, \theta) q(s' - s) ds d\theta \tag{18}$$

where

$$q(s) = \int_{-\infty}^{\infty} |R| W(R) \exp(i2\pi Rs) dR$$

and

$$s' = r\cos(\theta - \phi)$$

The inner integral over s is a one-dimensional convolution and the outer integral, an averaging operation over θ is called *back projection.* This implementation of the convolution backprojection algorithm is commonly used in medical imaging.

Applications of the CBP algorithm to flow and heat transfer problems have been reviewed by Munshi [94].

6.2 Iterative Techniques

Series expansion methods are perhaps the most appropriate tomographic technique for interferometry since they work with limited projection data. These methods are iterative in nature and consist necessarily of four major steps, namely:

1. initial assumption of the field to be reconstructed over a grid,
2. calculation of the correction for each pixel,
3. application of the correction, and
4. test for convergence.

The central idea behind the calculation of the correction (step 2) is the following. With the assumed field, one can explicitly compute the projection values by numerical integration. The difference between the computed projection and experimentally recorded projection data is a measure of the error in the assumed solution. This error can be redistributed to the pixels so that error is reduced to zero. Repetition of these steps is expected to converge to a meaningful solution. The series expansion techniques differ only in the manner in which the errors are redistributed over the grid.

The word *convergence* in step 4 is used in an engineering sense as a stopping criterion for the iterations, and not in the strict mathematical sense, where a formal proof is needed to show convergence of the numerical solution to the exact solution.

The iterative methods require the discretization of the plane to be reconstructed by a rectangular grid (Fig. 32). The length of the intercept of the i-th ray with the j-th cell in a given projection is known as the weight function, w_{ij}. If f_j is the field value in the j-th cell, it can be shown that

$$\phi_i = \sum_{j=1}^{N} w_{ij} f_i \qquad i = 1, 2, \ldots, M \tag{19}$$

where ϕ refers to the projection data. The number of unknowns N in most cases is much larger than the number of unknowns M. This discretization produces a matrix equation

$$[w_{ij}]\{f_j\} = \{\phi_i\} \tag{20}$$

The problem of reconstruction thus is a problem of inversion of a rectangular matrix. Iterative techniques that are used in the tomography can be viewed as developing a generalized inverse of the matrix $[w_{ij}]$. This matrix in a typical laser tomography problem has large dimensions. For the differentially heated fluid layer, the greatest matrix size encountered was 560×14400. This is a sparse matrix with many of its

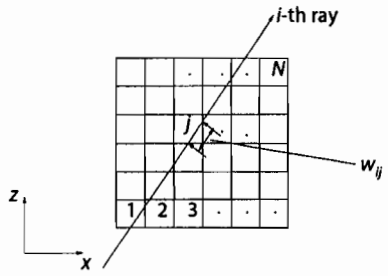

Figure 32 Discretization of a plane of fluid layer for art calculations.

elements being zero. General purpose matrix libraries cannot be used to invert such matrices since they are highly ill-conditioned and rectangular in structure. The tomographic algorithms can be seen as a systematic route towards a meaningful inversion of the matrix equation.

Series expansion methods being discussed in the present section can be classified into: ART (Algebraic Reconstruction Technique) and MART (Multiplicative Algebraic Reconstruction Technique). The optimization techniques that are also iterative in nature have been discussed with reference to maximization of the entropy and minimization of the energy functions.

The ART and MART families of algorithms differ only in the method of updating the field parameters in each iteration. In ART, the correction is additive while for MART, the correction is multiplicative. In both cases, the numerical procedure is based on the comparison of the estimated projection from an initial guess with the measured projection data obtained through experiments. This gives a correction term for the field variables. The value of the field variables are then updated. Once an iteration is over, the field value differs from the previous guess. The extent of the difference is then calculated. If the difference is within acceptable limits, the field value is taken to represent the physical field. Otherwise the iterations continue until the convergence criterion is satisfied.

Since the original field in real experiments is unknown, an estimate of the number of iterations can be found by using test functions (called *phantoms*) that are similar in nature to the original field. The test functions are also perturbed with noise to gauge the sensitivity of the algorithms to issues such as initial guess and errors in the projection data. This method can only be adopted where an exact estimate of noise in the projection data and a good knowledge of the original field is known beforehand. Variations in the noise level and nature of distribution of the noise in the projection data can alter the convergence rates.

Tomographic algorithms used in the present work are iterative in nature and intermediate steps may also involve iterations in the form of FOR loops. To identify the beginning and the ending of each iterative loop, start and close labels with statement numbers have been indicated in the description of each algorithm. These algorithms are briefly surveyed in the following sections.

6.3 ART

Various ART algorithms are available in the literature owing their origin to Kaczmarz [95] and Tanabe [96]. They differ from each other in the way the correction is applied. Those presented below have been tested successfully by the author and his coworkers in the context of interferometry.

6.3.1 Simple ART. This algorithm has been suggested by Mayinger [6]. The corrections are applied through a weight factor, computed as an average correction along a ray. The difference between the calculated projections with the measured projection data gives the total correction to be applied for a particular ray. The average correction is then the contribution to each cell falling in the path of the ray. This is computed by dividing the total correction obtained with the length of the ray. The calculated projections are computed once for a particular angle. Though the field values are continuously updated the calculated projection values remain unchanged until the completion of all the rays for a given angle. This algorithm will be referred to as ART1 in future discussions.

Let $\phi_{i\theta}$ be the projection due to the i-th ray in the θ direction of projection and $\tilde{f}_i$ be the initial guess of the field value. Numerically the projection $\tilde{\phi}_{i\theta}$ using the current field values is defined as:

$$\tilde{\phi}_{i\theta} = \sum_{j=1}^{N} w_{i\theta,j} f_j \qquad i\theta = 1, 2, \ldots, M_\theta \tag{21}$$

The individual steps in the algorithm are listed below.
Calculate the total value of weight function ($W_{i\theta}$) along each ray as:
start: 1 For each projection angle (θ):
start: 2 For each ray ($i\theta$):
start: 3 For each cell (j):

$$W_{i\theta} = \sum_{j=1}^{N} w_{i\theta,j}$$

close: 3
close: 2
close: 1
start: 4 Start iterations (k):
start: 5 For each projection angle (θ):
start: 6 For each ray ($i\theta$):
Compute the numerical projection (Equation 21)

close: 6
start: 7 For each ray ($i\theta$):
Calculate the correction as:

$$\Delta\phi_{i\theta} = \phi_{i\theta} - \bar{\phi}_{i\theta}$$

Calculate the average value of correction as:

$$\overline{\Delta\phi_{i\theta}} = \frac{\Delta\phi_{i\theta}}{W_{i\theta}}$$

close: 7
start: 8 For each ray ($i\theta$):
start: 9 For each cell (j):
If $w_{i\theta,j}$ is non-zero then:

$$f_j^{\text{new}} = f_j^{\text{old}} + \mu\overline{\Delta\phi_{i\theta}}$$

where μ is a relaxation factor.
close: 9
close: 8
close: 5
Check for convergence as:
If

$$\text{abs}\left[\frac{f^{k+1} - f^k}{f^{k+1}}\right] \times 100 \leq e$$

(where e is the prescribed convergence criteria, say 0.01%)
STOP:
Else: Continue
close: 4 (k)

6.3.2 Gordon ART. The ART algorithm contributed by Gordon et al. [97] is considered. Mayinger's ART is similar to this original version under the condition that no two rays simultaneously pass through a particular cell for a given projection. In this method corrections are applied to all the cells through which the i-th ray passes, using the weight factor which is exactly the proportion of w_{ij} to the total length of the

ray. The projection data gets updated after calculations through each ray. This procedure will be referred to as ART2. The individual steps are:
Calculate the total value of weight function ($W_{i\theta}$) along each ray as:
start: 1 For each projection angle (θ):
start: 2 For each ray ($i\theta$):
start: 3 For each cell (j):

$$W_{i\theta} = \sum_{j=1}^{N} w_{i\theta,j} \times w_{i\theta,j}$$

close: 3
close: 2
close: 1
start: 4 Start iterations (k):
start: 5 For each projection angle (θ):
start: 6 For each ray ($i\theta$):
Compute the numerical projection (Equation 21)
Calculate the correction as:

$$\Delta\phi_{i\theta} = \phi_{i\theta} - \tilde{\phi}_{i\theta}$$

start: 7 For each cell (j):
If $w_{i\theta,j}$ is non-zero then:

$$f_j^{\text{new}} = f_j^{\text{old}} + \mu \frac{\Delta\phi_{i\theta} \times w_{i\theta,j}}{W_{i\theta}}$$

where μ is a relaxation factor.
close: 7
close: 6
close: 5
Check for convergence as:
If

$$\text{abs}\left[\frac{f^{k+1} - f^k}{f^{k+1}}\right] \times 100 \leq e$$

STOP:

Else: Continue
close: 4 (k)

6.3.3 Gilbert ART. Gilbert [98] has developed independently a form of ART known as SIRT (Simultaneous Iterative Reconstruction Algorithm). In SIRT, the elements of the field function are modified after all the corrections corresponding to individual pixels have been calculated. This will be referred to as ART3. The numerically generated projections are computed once for all the angles and gets updated only after the completion of calculations through all the rays. For each ray from all angles, all the cells are examined to look for those rays which pass through a particular cell. For each cell, the rays which pass through it will contribute a correction that is decided by the weight factor w_{ij}. The algebraic average of all these corrections is implemented on the cell. This procedure will be called ART3. Its individual steps are: Calculate the total value of weight function ($W_{i\theta}$) along each ray as:
start: 1 For each projection angle (θ):
start: 2 For each ray ($i\theta$):
start: 3 For each cell (j):

$$W_{i\theta} = \sum_{j=1}^{N} w_{i\theta,j} \times w_{i\theta,j}$$

close: 3
close: 2
close: 1
start: 4 Start iterations (k):
start: 5 For each projection angle (θ):
start: 6 For each ray ($i\theta$):
Compute the numerical projection (Equation 21)
Calculate the correction as:

$$\Delta\phi_{i\theta} = \phi_{i\theta} - \tilde{\phi}_{i\theta}$$

close: 6
close: 5
start: 7 For each cell (j):
Identify all the rays passing through a given cell (j) (let Mc_j be the total number of rays passing through the j-th cell) and corresponding $i\theta$, $w_{i\theta,j}$, $W_{i\theta}$ and $\Delta\phi_{i\theta}$.

Apply correction as:

$$f_j^{\text{new}} = f_j^{\text{old}} + \frac{1}{Mc_j} \sum_{Mc_j} \mu \frac{w_{i\theta,j} \Delta\phi_{i\theta}}{W_{i\theta}}$$

where μ is the relaxation factor.
close: 7
Check for convergence as:
If

$$\text{abs}\left[\frac{f^{k+1} - f^k}{f^{k+1}}\right] \times 100 \leq e$$

STOP:
Else: Continue
close: 4 (k)

6.3.4 Anderson ART. Anderson and Kak [99] have proposed a variation to the ART algorithm. This algorithm is abbreviated as SART (Simultaneous Algebraic Reconstruction Technique). The method of implementing the correction is similar to ART1. The only difference this algorithm has from ART1 is in the calculation of correction for each cell. The weight factor used here is the exact intersection of a ray with the concerned cell. In contrast, ART1 uses the average correction for all the cells. This algorithm will be referred to as ART4. The individual steps are:
Calculate the total value of weight function ($W_{i\theta}$) along each ray as:
start: 1 For each projection angle (θ):
start: 2 For each ray ($i\theta$):
start: 3 For each cell (j):

$$W_{i\theta} = \sum_{j=1}^{N} w_{i\theta,j} \times w_{i\theta,j}$$

close: 3
close: 2
close: 1
start: 4 Start iterations (k):
start: 5 For each projection angle (θ):
start: 6 For each ray ($i\theta$):
Compute the numerical projection (Equation 21)
close: 6
start: 7 For each ray ($i\theta$):
Calculate the correction as:

$$\Delta\phi_{i\theta} = \phi_{i\theta} - \tilde{\phi}_{i\theta}$$

start: 8 For each cell (j):
If $w_{i\theta,j}$ is non-zero then:

$$f_j^{\text{new}} = f_j^{\text{old}} + \mu \frac{\Delta\phi_{i\theta} \times w_{i\theta,j}}{W_{i\theta}}$$

where μ is a relaxation factor.
close: 8
close: 7
close: 5
Check for convergence as:
If

$$\text{abs}\left[\frac{f^{k+1} - f^k}{f^{k+1}}\right] \times 100 \leq e$$

STOP:
Else: Continue
close: 4 (k)

6.4 MART

When the corrections in the iterative algorithms are multiplicative rather than additive, the algorithms are grouped under the family of MART (Verhoeven, [31]). Gordon et al. [97] and Gordon and Herman [100] have suggested different forms of MART. The MART algorithms presented below are similar to those considered by Verhoeven [31].

The major difference between ART and MART algorithms is in the method of computing the corrections. While ART uses the difference between the calculated projections and measured projections, MART uses the ratio between the two. Hence the corrections applied to each cell during calculations are via the multiplication operation. The structure otherwise is similar to Gordon's ART (ART2).
The individual steps of three versions of MART (1, 2, and 3) are summarized below.
start: 1 Start iterations (k):
start: 2 For each projection angle (θ):
start: 3 For each ray ($i\theta$):
Compute the numerical projection (Equation 21)
Calculate the correction as:

$$\Delta\phi_{i\theta} = \frac{\phi_{i\theta}}{\bar{\phi}_{i\theta}}$$

start: 4 For each cell (j):
If $w_{i\theta,j}$ is non-zero then:
MART1:

$$f_j^{\text{new}} = f_j^{\text{old}} \times (1.0 - \mu \times (\Delta\phi_{i\theta}))$$

MART2:

$$f_j^{\text{new}} = f_j^{\text{old}} \times \left(1.0 - \mu \times \frac{w_{i\theta,j}}{(w_{i\theta,j})_{\max}} \times (1.0 - \Delta\phi_{i\theta})\right)$$

MART3:

$$f_j^{\text{new}} = f_j^{\text{old}} \times (\Delta\phi_{i\theta})^{\frac{\mu w_{i\theta,j}}{(w_{i\theta,j})_{\max}}}$$

where μ is a relaxation factor.
close: 4
close: 3
close: 2
Check for convergence as:
If

$$\text{abs}\left[\frac{f^{k+1} - f^k}{f^{k+1}}\right] \times 100 \leq e$$

where e is a suitable stopping criterion.
STOP:
Else: Continue
close: 1

Steps 3 and 4 form the essence of the reconstruction algorithm. All three versions include the relaxation factor μ. Typical values of the relaxation factor reported are in the range 0.01–0.1, larger values leading to divergence. It is to be noted that the correction calculated in step 3 is the ratio of the recorded projection data ($\phi_{i\theta}$) and that calculated from the guessed field, namely $\bar{\phi}_{i\theta}$ which is being iterated. The three versions of MART differ in the manner in which the corrections are implemented. In MART1, the weight function is prescribed in binary form, being unity if a particular

ray passes through a pixel and zero otherwise. In MART2 and MART3, the weight function is precisely calculated as the ratio of the length of the ray intercepted by the pixel and the maximum dimension of a segment enclosed by it.

6.5 AVMART

The reconstruction of a function from a finite number of projections recorded at different view angles leads to an ill-posed matrix inversion problem. The problem is accentuated when the projection data is limited. The resulting matrix is rectangular with the number of unknowns being greater than the number of equations. In view of the ill-conditioning of the matrix, the convergence of the iterations to any particular solution is dependent on the initial guess, the noise level in the projection data and the under-relaxation parameter employed. In the present study, the MART algorithm has been extended so as to (1) enlarge the range of the usable relaxation factor, (2) diminish the influence of noise in the projection data, and (3) guarantee a meaningful solution when the initial guess is simply a constant.

The original MART algorithm described above has been modified in the present work to form a new approach to applying the corrections. In the proposed algorithm the corrections are calculated by considering all the rays from all the angles passing through a given pixel. Instead of a single correction obtained from individual rays, a correction that is determined as the average of all the rays is used. The difference between the conventional MART and the present implementation is the following. The correction at each pixel is updated on the basis of the N-th root of the product of all the corrections from all the N rays of all view angles passing through a pixel. This idea is based on the fact that average corrections are expected to behave better in the presence of noisy projection data. Since an average correction is introduced, the algorithm is desensitized to noise. There is however a potential drawback. Since an average pixel correction based on a set of rays is computed, the reconstructed field is not required to satisfy exactly the recorded projection data. This was seen to be no cause for concern for the three applications considered. The projection data was exactly satisfied by the reconstructed field in each case.

The modified algorithms have been identified below as AVMART, the prefix AV referring to average. The important step, namely step 4 alone is presented here, with the understanding that all other steps remain unchanged.

start: 4 For each cell (j):

Identify all the rays passing through a given cell (j). Let Mc_j be the total number of rays passing through the j-th cell.

Apply correction as:

AVMART1:

$$f_j^{new} = f_j^{old} \times \left(\prod_{Mc_j} (1.0 - \mu \times (\Delta\phi_{i\theta})) \right)^{\frac{1}{Mc_j}}$$

AVMART2:

$$f_j^{\text{new}} = f_j^{\text{old}} \times \left(\prod_{Mc_j} \left(1.0 - \mu \times \frac{w_{i\theta,j}}{(w_{i\theta,j})_{\max}} \times (1.0 - \Delta\phi_{i\theta}) \right) \right)^{\frac{1}{Mc_j}}$$

AVMART3:

$$f_j^{\text{new}} = f_j^{\text{old}} \times \left(\prod_{Mc_j} (\Delta\phi_{i\theta})^{\frac{\mu w_{i\theta,j}}{(w_{i\theta,j})_{\max}}} \right)^{\frac{1}{Mc_j}}$$

close: 4

The symbol Π in the three algorithms above represents a product over the variable Mc_j. The Mc_j-th root of this product is evaluated in each approach. The relaxation factor μ has been retained in the statements above for completeness. In all calculations, it was set equal to unity to bring out a mixture of the "smooth" and "sharp" features of the temperature field [16]. As discussed in Section 3, the proposed algorithms require a smaller CPU time per iteration, when compared to the existing ones. Section 6.7 evaluates the benefits derived by modifying step 4 for problems of practical importance.

6.6 Maximum Entropy

Based on ideas from information theory, one can perform image analysis and construct meaningful tomographic algorithms. Suppose there is a source which generates a discrete set of independent messages r_k with probabilities p_k. Then the information associated with r_k is defined logarithmically as

$$I_k = -\ln p_k$$

The entropy of the source is defined as the average information generated by the source and can be calculated as

$$\text{entropy} = -\sum_{k=1}^{L} p_k \ln p_k$$

When the source is the image, the probability can be replaced by the gray level f_j, for the j-th pixel and entropy can be redefined as

$$\text{entropy} = -\sum_{j=1}^{N} f_j \ln f_j$$

For natural systems, the organization of intensities f_j over the image can be expected to follow the second law of thermodynamics namely,

$$f_j: \qquad -\sum_{j} f_j \ln f_j = \text{maximum}$$

This is the basis of the MAXENT algorithm. For interferometric images, one can view the pixel temperature as the information content and entropy built up using their magnitudes. In the absence of any constraint, the solution of the above optimization problem will correspond to a constant temperature distribution, more generally a uniform histogram in terms of probabilities. Hence, the MAXENT algorithm is properly posed only along with the projections as constraints.

Requiring that the entropy of the system be a maximum along with the interferometric projections as constraints is known as the Maximum entropy optimization technique (MAXENT) [30]. It produces an unbiased solution and is maximally noncommittal about the unmeasured parameters. This technique is particularly attractive when the projection data is incomplete (see Censor [29]). The MAXENT algorithm is described below:

Consider a continuous function $f(x, y, z)$ with the condition $f(x, y, z) \geq 0$ and values f_j at $j = 1 \ldots N$ pixels. In the present context, the entropy technique refers to the extremization of the

$$F = -\sum_{j=1}^{N} f_j \ln |f_j| \tag{22}$$

subject to a set of constraints. In MAXENT the collected projection data and any other *a priori* information about the field to be reconstructed can be viewed as the constraints over which the entropy is to be maximized. A typical maximum entropy problem can be stated as:

$$\text{Maximize}\left(-\sum_{j=1}^{N} f_j \ln|f_j|\right)$$

$$\text{subject to } \phi_j = \sum_{j=1}^{N} w_{ij} f_j$$

$$\text{and} \quad f_j \geq 0 \tag{23}$$

Different schemes are available for optimizing a functional over some constraints, for example the Lagrange multiplier technique.

The MART algorithms have been shown to be equivalent to the maximum entropy algorithm in the literature [28, 29]. Hence the entropy algorithm has not been considered further in the present article.

6.6.1 Minimum Energy. The MAXENT algorithm can be generalized for any other function in place of entropy. Gull and Newton [30] have suggested four such functions which can be maximized with the projections as constraints to obtain the tomographic reconstruction. After entropy, the energy functions are attractive and natural for use in physical problems. The minimum energy method (MEM) can be implemented in a manner analogous to MAXENT as follows

$$\text{Maximize}\left(-\sum_{j=1}^{N} f_j^2\right)$$

$$\text{subject to } \phi_j = \sum_{j=1}^{N} w_{ij} f_j \tag{24}$$

Compared to MAXENT, MEM has a simpler implementation while using the Lagrangian multiplier technique, since it results in a set of linear equations. Gull and Newton [30] however have recommended the MAXENT over MEM, since they found that the MEM produces a field which is negatively correlated and hence produced a biased solution.

6.7 Testing of Tomographic Algorithms

The ART, MART and the optimization algorithms have been tested for variety of cases by Subbarao et al. [32]. In the examples, the temperature fields were synthetically generated. Hence it was possible to determine explicitly the convergence prop-

erties and errors for each of the methods. Among the various algorithms, the authors have identified MART3 as the best in terms of the error and CPU time requirements. The AVMART algorithms proposed by the author and his coworkers have been validated in the present section against two benchmark cases: (1) a circular region with five holes, and (2) the numerically generated three-dimensional temperature field in fluid convection. Employing a temperature field similar to that encountered in the experiments aids in the choice of the proper initial guess and the error levels to be anticipated. This also helps in selecting the proper tomographic algorithm.

6.7.1 Results and Discussion. The algorithms stated in Sections 6.4 and 6.5 have been tested for a circular region with distribution of holes and a numerically generated three-dimensional temperature field in Rayleigh–Benard convection. Sensitivity of the algorithms to noise has been tested in the context of numerically generated temperature data. Issues addressed in the sensitivity study are initial guess, noise in projection data, and the effect of increasing number of projections on the accuracy of reconstruction.

Reconstruction of a Circular Disk With Holes. A circular region with five symmetrically placed holes is considered. The object is recognized in terms of the local dimensionless density, which is zero at the holes and unity elsewhere. To implement the reconstruction algorithm, it is convenient to enclose the circular object within a square domain. The gap between the circle and the square is specified to have zero density (in calculations, a value of 0.001 has been used for zero density). The square region is discretized into 61×61 cells in the x and y directions. Projections of this object have been determined analytically and are hence exact. The recovery of the original object from a limited number of these projections using the original MART as well as the proposed AVMART algorithms is discussed below.

Projections at angles of 0, 45, 90, and 135 degrees have been considered in the present application. The initial guess for the density field was a constant value of unity. A convergence criterion of 1% for the iterations has been uniformly used. At a convergence of 0.01%, the solution was practically identical, except that errors were seen to be marginally higher. This feature of tomographic algorithms, that convergence is asymptotic (but not monotonic) has been reported earlier [28]. Such trends are to be expected in the reconstruction of fields having a step discontinuity, at the hole boundary in the present example. The relaxation factor was set at 0.1 in case of original MART while it was unity in the AVMART algorithms. All calculations were carried out on a DEC-alpha workstation with 196 MB RAM and a 233 MHz processor.

A summary of the reconstructed fields using the three original and three proposed algorithms is shown in Figure 33. In principle, all the six algorithms were seen to converge to a qualitatively meaningful solution. The void fraction, namely the fraction of the space occupied by the holes was 0.34 in the present application. In the reconstructed solution, the void fraction can be determined from the formula

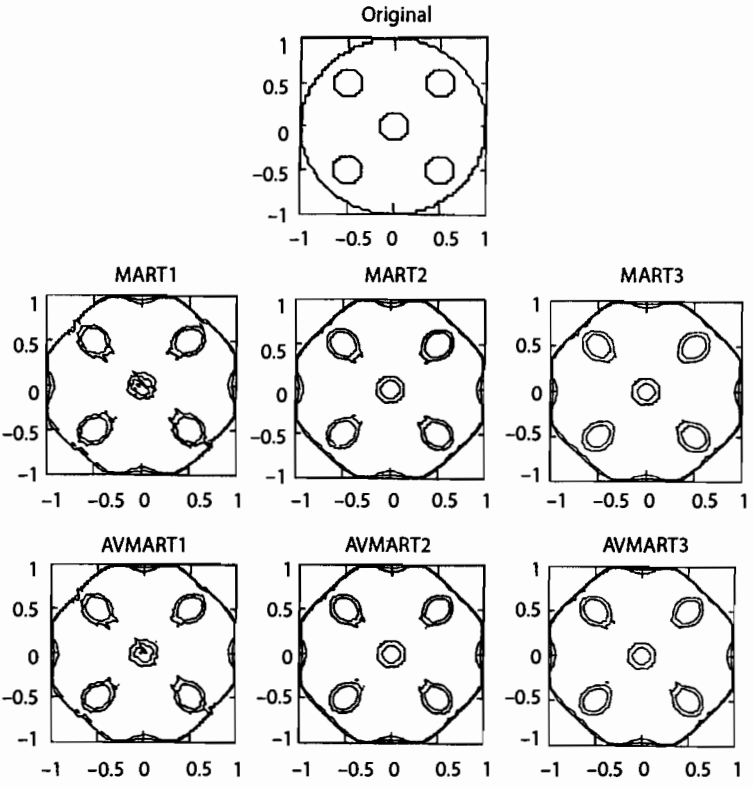

Figure 33 Original and reconstructed density fields of a circular region with holes (the outer circle appears as an octagon because of a finite number of view angles employed).

$$\text{void / / fraction} = 1.0 - \frac{\sum_{i=1}^{N} \rho_i}{N}$$

It was found that all the six algorithms reproduced a void fraction of precisely 0.34. The algorithms however differed in terms of CPU time, errors, and error distribution. The three different error norms reported in the present work are:

$$E_1 = \max[\text{abs}(\rho_{\text{orig}} - \rho_{\text{recon}})] \quad \text{Maximum of absolute difference}$$

$$E_2 = \sqrt{\frac{\sum[(\rho_{\text{orig}} - \rho_{\text{recon}})]^2}{N}} \quad \text{RMS error}$$

Table 6 Comparison of the MART Algorithms: Circular Region with Holes

Quantity	MART1	MART2	MART3	AVMART1	AVMART2	AVMART3
E_1	0.99	0.96	0.95	0.99	0.96	0.96
E_2	0.25	0.24	0.23	0.24	0.23	0.23
E_3, %	25.12	24.08	23.63	24.59	23.72	23.65
Number of points (%) having error in the range						
> 95%	0.27	0.05	0.05	0.27	0.05	0.05
75–95%	0.64	0.62	0.86	0.83	0.72	0.70
50–75%	3.90	4.11	4.43	3.47	4.00	3.98
Iterations	51	63	29	17	24	21
CPU (minutes)	9.51	11.97	5.65	0.32	0.45	0.40

$$E_3 = \frac{E_2}{\rho_{max} - \rho_{min}} \times 100 \quad \text{Normalized RMS error, \%}$$

Results for the error level distribution in the reconstructed field have also been determined. The distribution of the absolute error as a percentage of the E_1 error has been presented in the regions 95%, 75%–95%, and 50%–75%. Errors and their distribution along with the computational details are given in Table 6.

It is clear from Table 6 that the errors for all the six algorithms are practically close, with those of MART1 and AVMART1 being marginally on the higher side. An examination of the error distribution shows that large errors (>95%) are seen only over 0.27% of the physical region. Specifically, large errors are restricted to the surface of the holes, where a step change in the field property (the density in the present example) takes place. The errors are uniformly small elsewhere. The most significant difference between the original and the proposed algorithms is in terms of the number of iterations (and correspondingly in the CPU time). The proposed algorithms require fewer iterations for convergence and require a smaller CPU time. This is clear evidence of the computational efficiency of the proposed algorithms in the context of exact projection data.

Reconstruction of a Numerically Generated Thermal Field. The second application taken up for analysis comprises of a numerically generated convective thermal field in a horizontal differentially heated fluid layer. For definiteness, the wall temperatures employed are 15°C and 30°C, respectively. The three-dimensional temperature field has been determined as follows. The stream function, vorticity, and energy equations are solved in two dimensions with symmetry conditions applied on the side walls, by a finite difference method [101]. The solution thus obtained corresponds to a system of longitudinal rolls spread over an infinite fluid layer. Such geometries show a polygonal planform corresponding to a fully three-dimensional temperature field [102]. The three-dimensionality has been simulated in the present work by superimposing a sine variation in the thermal field parallel to the axis of the

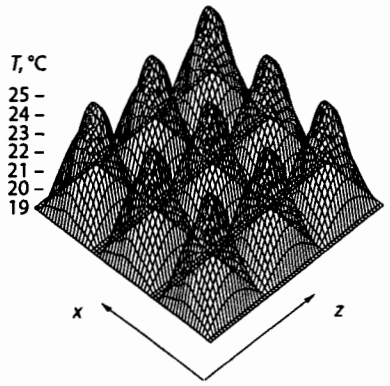

Figure 34 Temperature surface of the midplane of the fluid layer, in the form of cubic cells.

roll. A surface plot of the resulting temperature field revealed the flow to be organized in the form of cubic cells in the fluid layer (Fig. 34).

The advantages of selecting the field to be reconstructed in the particular manner outlined above are: (1) The field is continuous and hence reconstruction errors can be expected to be small, as compared to the application with holes. (2) Errors with perfect data being small, one can systematically study errors induced by the initial guess, and noise in the projection data. (3) The thermal field being analyzed is physically realizable.

For reconstruction, the fluid layer has been discretized into 11 planes and each plane into 61×61 cells. The relaxation factor for the proposed algorithms has been set to unity. Since the algorithms are being tested under conditions of limited data, only two and four projections have been considered. A convergence criterion of 0.01% has been uniformly employed in the computation. Results obtained using the proposed MART algorithms alone have been reported.

The errors reported here are on the basis of the entire fluid layer. The three different errors reported are:

$$E_1 = \max[\text{abs}(T_{\text{orig}} - T_{\text{recon}})] \quad \text{Maximum of absolute difference, °C}$$

$$E_2 = \sqrt{\frac{\sum[(T_{\text{orig}} - T_{\text{recon}})]^2}{N}} \quad \text{RMS error, °C}$$

$$E_3 = \frac{E_2}{T_{\text{hot}} - T_{\text{cold}}} \times 100 \quad \text{Normalized RMS error, \%}$$

In these definitions, T_{hot} and T_{cold} are the hot and cold plate temperatures. T_{orig} and T_{recon} are the temperature variables of the original and the reconstructed field respectively. Results for the error level distribution in the fluid layer have also been deter-

Table 7 Comparison of the AVMART Algorithms in a Differentially Heated Fluid Layer

Initial guess	Quantity	AVMART1	AVMART2	AVMART3
Constant	E_1, °C	1.97	1.97	1.97
	E_2, °C	0.49	0.48	0.49
	E_3, %	2.86	2.79	2.86
	Iterations	9	12	14
	CPU, sec	30.6	41.3	47.2
Two-dimensional longitudinal rolls	E_1, °C	1.98	1.98	1.98
	E_2, °C	0.49	0.49	0.49
	E_3, %	2.86	2.86	2.86
	Iterations	8	12	12
	CPU, sec	28.9	41.2	42.7
Random	E_1, °C	12.15	13.42	6.20
	E_2, °C	5.59	4.74	0.60
	E_3, %	32.70	27.77	3.50
	Iterations	15	17	14
	CPU, sec	52.8	59.1	47.8

mined. The distribution of the absolute error as a percentage of the E_1 error has been presented in the three zones as before namely, > 95%, 75% to 95%, and 50–75%.

Sensitivity to Initial Guess. The inversion of matrices arising from the ART family of algorithms from limited projection data is a mathematically ill-posed problem. As a rule, the number of equations here is much smaller than the number of unknowns. This makes the solution-set infinite in the sense that a unique solution is not guaranteed. Different initial guesses, may in principle, lead to different solutions of this infinite set. In the absence of any knowledge about the field being studied, it is a difficult task to prescribe the initial guess. The sensitivity of the algorithms to the initial guess has been studied with reference to three different fields, namely:

1. a constant temperature field (= 1°C)

2. temperature distribution corresponding to two-dimensional longitudinal rolls, and

3. a random field between 0°C and 1°C with an RMS value of 0.5°C.

The initial guesses 1 and 2 were seen to qualitatively reproduce the thermal field of Figure 34 quite well (the reconstructed thermal field have not been shown as they are very close to the original). The noise present in the third guess was seen to be present in the reconstructed data. But the noise could be filtered in the frequency domain using a band-pass filter function. The reconstructed field after noise-removal was seen to be similar to the original in Figure 34. The errors, number of iterations and the CPU time for the three initial guesses are presented in Table 7. The fractional distribution of errors are reported in Table 8. With initial guesses 1 and 2, the RMS and fractional errors can be seen to be small for all the three algorithms. The maximum error is larger, but with reference to Table 8, it can be seen that large errors are

Table 8 Fractional Distribution of the E_1 Error over the Fluid Layer

Initial guess	Number of points (%) having error in the range	AVMART1	AVMART2	AVMART3
(1)	> 95	0.17	0.17	0.17
	75–95	0.57	0.48	0.57
	50–75	5.76	5.15	5.73
(2)	> 95	0.17	0.17	0.17
	75–95	0.60	0.62	0.62
	50–75	5.68	5.58	5.58
(3)	> 95	0.02	0.01	0.002
	75–95	5.79	2.00	0.02
	50–75	34.46	11.92	0.30

restricted to small areas and are hence localized. Thus, in effect the initial guesses 1 and 2 may be considered to be equivalent. The errors corresponding to the third guess are uniformly higher for the proposed AVMART1 and AVMART2 algorithms, but small for AVMART3. The number of iterations for AVMART3 are also smaller. Hence, AVMART3 emerges as the best algorithm among those proposed in terms of errors and CPU time for a noisy initial guess. For an unbiased and regular initial guess, computations over a wider range of parameters show AVMART2 to be the best (see the section on Sensitivity to Noise in Projection Data).

The insensitivity of AVMART3 algorithm to noise can be explained as follows. In the other two algorithms, correction is applied by finding the Mc_j-th root of the product of all corrections arising from Mc_j rays. In the third, the root is corrected for the length of the intercept of each ray with the cell under question. This improves the estimate of the path integral.

Sensitivity to Noise in Projection Data. In measurements involving commercial grade optical components and recording and digitizing elements, the projection data is invariably superimposed with noise. Software operations such as interpolation and image processing can also contribute to errors in the projection data. Experience of the authors with interferometric experiments shows that the RMS noise level is around 5% [78].

The performance of the three proposed algorithms have been compared with noisy projection data as the input. A 5% noise level has been adopted for all calculations. The noise pattern has been generated using a random number generator, with a uniform probability density function. Results have been presented for 2 and 4 projections corresponding to view angles of (0° and 90°) and (0°,60°, 90°, and 150°), respectively. The initial guess for reconstruction with 2 projections is simply a constant; for 4 projections, the result obtained with 2 projections has been used as the initial guess.

Results with 2 projections show that all three algorithms reproduce qualitatively the temperature field of Figure 2. However quantitative differences are to be seen. The noise level in the reconstructed field is found to be slightly higher than that in

Table 9 Comparison of the AVMART Algorithms: 5% Noise in Projection Data, Two-View Reconstruction

Quantity	AVMART1	AVMART2	AVMART3
E_1, °C	4.452	4.449	4.450
E_2, °C	1.08	1.08	1.08
E_3, %	6.37	6.36	6.37
Number of points (%) having error in the range			
> 95	0.004	0.004	0.004
75–95	0.222	0.200	0.222
50–75	4.400	4.387	4.400
Inerations	9	12	14
CPU, sec	30.5	40.9	47.8

the projection data. The magnitude of the three different errors and the distribution of the fractional error over the fluid domain are presented in Table 9. All the three algorithms are practically equivalent in terms of errors, though AVMART2 is seen to be marginally better from the error point of view. However the CPU time of AVMART1 is minimum. It is to be noted that noise (in terms of E_3) in the projection data has been amplified during the reconstruction process (from 5% to 6.4%). This is in contrast to noise in the initial guess, where iterations tend to diminish errors in the converged field.

Reconstruction with 4 view angles is taken up next. Table 10 shows the error levels in the reconstructed data and the distribution of these errors within the fluid layer. It can be seen immediately that the E_3 errors with 4 projections are larger than those for 2 projections alone. The distribution of errors shows that these are at best localized, i.e., large errors may occur at a few sporadic points. The AVMART1 algorithm shows a considerable deterioration in performance, since errors as well as CPU time are substantially higher. AVMART2 and AVMART3 algorithms are seen to perform

Table 10 Comparison of the AVMART Algorithms: 5% Noise in Projection Data, Four-View Reconstruction

Quantity	AVMART1	AVMART2	AVMART3
E_1, °C	11.80	5.52	5.52
E_2, °C	1.78	1.36	1.36
E_3, %	10.41	8.00	8.00
Number of points (%) having error in the range			
> 95	0.004	0.007	0.007
75–95	0.029	0.349	0.346
50–75	0.276	5.186	5.177
Inerations	190	53	53
CPU, sec	1767.7	502.3	520.8

better than AVMART1. AVMART2 is marginally superior to AVMART3 since the error magnitudes are equal, but the former takes a smaller CPU time. Hence, a consolidated view to emerge from the discussion above is that AVMART2 exhibits the best performance.

It is of interest to compare the best proposed algorithm, namely AVMART2 with the best original MART algorithm identified by Subbarao et al. [32], namely MART3 of the present study. To this end, reconstruction was carried out using 2-views of 0° and 90° for convection in a horizontal differentially heated fluid layer, leading to two-dimensional longitudinal rolls. The projection data was superimposed with 5% noise and an initial guess of a constant temperature field was used. Errors for MART3 were seen to be amplified by a factor of 4 compared to a factor of 1.6 for MART2_new. The computer time was also higher by a factor of 4 when compared with MART2_new. However the fractional distribution of errors over the fluid layer were seen to be similar for both, thus confirming that they continued to belong to the same family of algorithms.

The following inferences can now be drawn from the discussion above:

1. The three AVMART algorithms show similar performance in the presence of noise in the projection data. AVMART2 is however marginally superior in terms of errors and CPU time.
2. The noise in the projection data persists after reconstruction.
3. Increasing the number of noisy projections amplifies the error in reconstruction.
4. AVMART2 clearly shows superiority over MART3 for noisy projection data. Hence it supersedes MART3 as the favored tomographic algorithm for the class of problems studied.

Both MART and AVMART algorithms have been tested extensively against experimental data. The errors as well as the convergence rates have been reported in Mishra et al. [81]. The conclusions drawn above carry over to experiments without any major modification. The convergence rates of all the algorithms were seen to deteriorate with increasing number of projection angles. This could be traced to the partial de-correlation among the interferometric images owing to mild unsteadiness in the convection patterns.

6.8 Closure

The MART family of algorithms available in the literature was seen to require a small relaxation factor leading to delayed convergence. To address this issue, a new set of algorithms have been proposed in the present work. The new set is conceptually similar to the original, but differs significantly in the manner in which corrections are applied. Specifically, the reconstructed field does not satisfy the projection data, pointwise. However, it can accommodate a wider range of relaxation factors and thus is better from a theoretical view point. Results with the relaxation factor set at unity have been reported in the present work.

The proposed algorithms have been evaluated in the context of three applications, namely: (1) circular disk with five holes, (2) three-dimensional convective thermal

field, and (3) interferometric data from a laboratory-scale differentially heated fluid layer experiment. The major results that emerge from the study are:

1. All six algorithms reconstruct the field variable in a qualitative sense. Differences are seen only in the numerical values.

2. The AVMART2 algorithm emerges as the best, in terms of CPU time, errors and sensitivity to initial guess and noise in the projection data.

3. The CPU time of the proposed algorithms is significantly smaller than those presently available in the literature.

4. With a limited number of projections, all algorithms show large absolute maximum errors, but these are sharply localized. Specifically, the qualitative appearance of the reconstructed field variable is acceptable from a practical viewpoint.

5. The convergence rate of the proposed algorithms is found to be better than the original, when the projection data is exact. In the presence of noise, all the six algorithms record a sharp reduction in the convergence rate. In a few cases, the proposed algorithms require a greater number of iterations compared to the original. However, in all applications, the CPU time requirement is substantially smaller for the proposed algorithms.

7 APPLICATIONS

Three sets of experiments involving (1) buoyant flow around a protruding heater [77], (2) transient convection in a square cavity [10], and (3) a differentially heated fluid layer [78–80, 82] are discussed in the present section. All of them employ interferometry, while experiment 3 is an extensive application of interferometric tomography to thermal convection.

7.1 Buoyancy-Driven Flow Around a Protruding Heater

Buoyancy-driven flow in the vicinity of a protruding heated copper block placed on a vertical wall and exposed to the ambient is experimentally studied here. The copper block is of height h, protrusion b, and a length L, which is much larger than h and b. It is located on a vertical bakelite board with its longest dimension L lying in the horizontal plane. All measurements have been carried out at steady state. The average Nusselt number as a function of Rayleigh number has been reported in this work. The thermal wake above the heated block as visualized by the Mach–Zehnder interferometer is also presented in this study.

The problem addressed here arises frequently in the thermal design of high-performance electronic components such as integrated chips in computers. An overall review of the subject for practical cooling configurations of electronic circuit boards has been presented by Incropera [103]. Heat transfer from arrays of protruding three-dimensional heaters under forced flow conditions have been experimentally studied by Garimella and Eibeck [104]. Experiments on two- and three-dimensional natural convection heat transfer from vertical, discrete, and arrays of flush and

mildly protruding heaters have been presented in the literature [105]. Nusselt number and wake size in natural convection for vertical and horizontal protruding thermal sources using thermocouple data have been studied by Kang and Jaluria [106].

The dimensionless parameters of the problem are the aspect ratio A (= h/b), Rayleigh number (Ra) and the average Nusselt number (Nu) based on the height h of the copper block. Fluid properties are evaluated at the average of the heater and room temperatures. There is some uncertainty in the form of the boundary condition at the heater surface since it can be prescribed as constant temperature or as constant heat flux. The use of a copper block would suggest the former, but since the heater size is quite small in the present study we continue to examine the constant heat flux boundary condition. The respective values of the temperature difference in the definitions of Ra and Nu are computed as $(T_c - T_{room})$ and $(q(h + 2b)/k)$ respectively. In all the data presented in this work, the aspect ratio A is equal to two.

Two different heaters of sizes (h, b, L) = (10, 5, 192) mm and (16, 8, 180) mm have been employed in the present work. Surface temperatures employed vary from 60°C to 101°C and room temperatures are in the range of 23.7–25.6°C. The copper block is electrically powered by a nichrome-wound heater placed behind it. The electrical resistance of the nichrome wire used is 95 ohms/m. The voltage applied to the heater is stabilized using a series of variances. The entire heater assembly is mounted on a bakelite sheet (Fig. 35). This sheet is placed vertically in an enclosed test cell that straightens the flow approaching the copper block.

Heat transfer from the electric heater to the ambient from the rear side of the test cell is estimated as follows. A thin copper strip of 25 mm height is firmly held against the bakelite sheet and its temperature is monitored by an array of thermocouples. The energy lost to the ambient outside the test cell is obtained by applying vertical flat plate correlations of natural convection to the copper strip. The ambient energy loss is found to be about 10% of the electrical input. Radiation losses are found to be negligible for the smaller of the copper blocks since its area is small and the surface is polished. For the larger block, radiation accounts for up to 5% of the energy input. It has been accounted for through detailed calculations including shape factors. Energy transferred in a direction parallel to the gravity vector to the bakelite

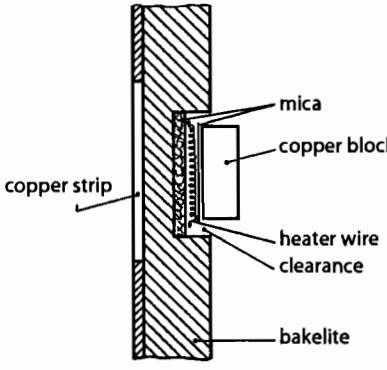

Figure 35 Schematic of the experimental apparatus of a protruding heater.

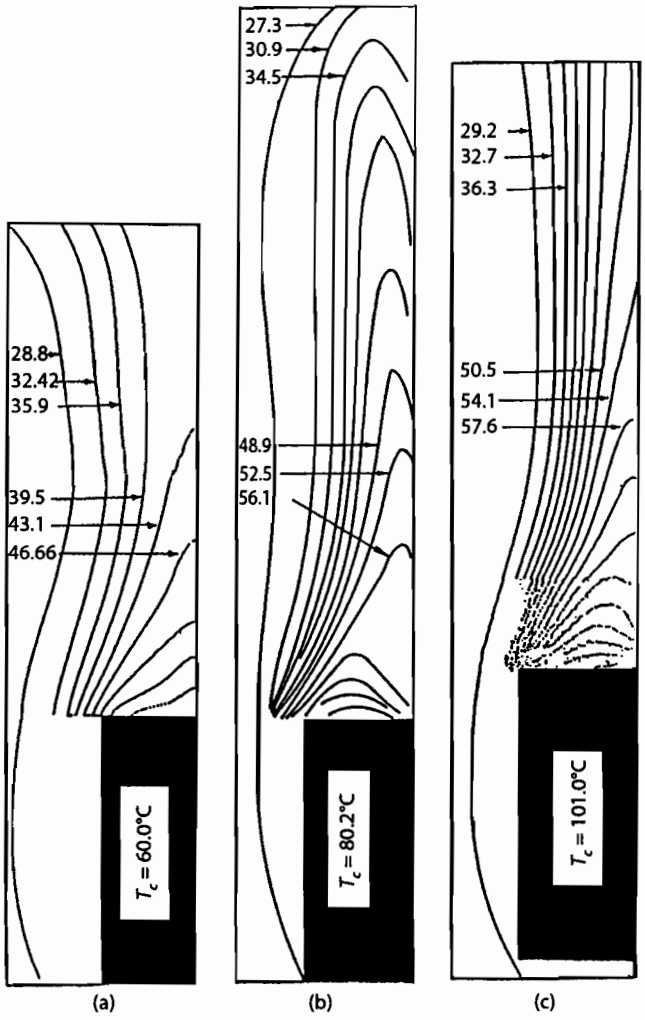

Figure 36 Thinned interferometric fringe patterns around a protruding heater on a vertical surface.

sheet supporting the copper block is not considered as a loss since it is recovered by the fluid ahead and beyond the heater.

The thermal field in the vicinity of the heater has been studied using a Mach–Zehnder interferometer. The path of the light beam is arranged to be parallel to the heater length. The interferograms are collected in the infinite fringe setting and hence the fringes are isotherms. Skeletonized fringes alone have been presented here. The fringe density near the chip is high and is corrupted by refraction errors. Hence the near-wall fringes have been removed using image processing operations. The outer most fringe representing the thermal boundary layer and all the fringes in

the wake have been preserved. For the experiments reported here the temperature drop per fringe shift is 3.5 K.

7.1.1 Interferograms. Interferometric data for the smaller copper block of height 10 mm and a protrusion of 5 mm is presented first. Figure 36 shows thinned fringes in the proximity of the heater at temperatures of 60°, 80.2°, and 101°C. Since the fluid below the lower surface is nearly stationary, fringes in this region have not been shown. The images have been recorded with varying magnifications to maintain clarity. The outermost fringe can be treated as the edge of the boundary-layer. The fringes within the boundary-layer are densely packed and as stated earlier, have been removed through image processing operations. The boundary-layer thickness δ can, however, be used for analysis. For an assumed quadratic temperature profile within the boundary-layer, the local Nusselt number for constant temperature as well as constant heat flux boundary conditions is $2h/\delta$.

An examination of Figure 36 shows the following trends. With temperature increasing from 60°C to 80.2°C, the thermal boundary-layer thickness decreases. Further increase in temperature to 101°C does not lead to any significant reduction in the boundary-layer thickness. At 60°C, the boundary-layer thickness is nonzero at the leading edge of the heated block. For the other two temperatures, δ is small at this location.

A drop in the value of boundary-layer thickness indicates an increase in the local Nusselt number. Hence the Nusselt number on the vertical face increases as one goes from 60°C to 80.2°C. This increase is only marginal between 80.2°C and 101°C. The fringe density, and hence, the heat flux over the upper horizontal face, continually increases as one moves from 60°C to 101°C. This is also a source of increasing the average Nusselt number with chip temperature.

7.1.2 Heat Transfer Rates. Figure 37 shows a plot of the local Nusselt number on the vertical face of the copper block determined using the boundary-layer thickness. The average value of the Nusselt number on the vertical face (= Nu(v)), and Nusselt number at the midpoint of the chip (= Nu(m)) corresponding to the three Rayleigh numbers are given in Table 11. Except for a block temperature of 60°C, these are

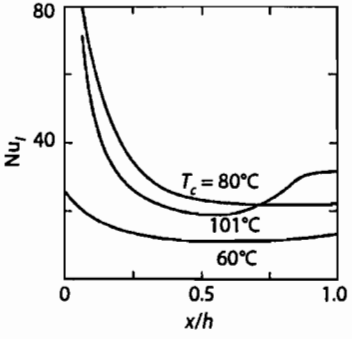

Figure 37 Local Nusselt number as a function of distance along the copper block.

Table 11 Average and Midpoint Nusselt Numbers on the Vertical Face of the Copper Block

T_c, °C	60	80.2	101
Ra (T)	2477	3349	3894
Nu (v)	13.5	30.8	28.6
Nu (m)	10.5	23.0	19.0

larger than the corresponding average values for the entire heater. At $T_c = 60°C$, the boundary-layer thickness at the leading edge is nonzero, resulting in a low Nusselt number over the vertical face of the copper block.

Table 12 gives values of Nusselt number (Nu) as a function of the Rayleigh number (Ra(T) and Ra(q)) based on the average heat transfer measurements of the present study.

It is of interest to compare the results obtained in Table 12 with correlations and data available in the literature. This comparison for buoyancy-driven flows from flush as well as protruding surfaces is presented below.

Isothermal vertical flat plate [89]

$$\mathrm{Nu} = (0.825 + 0.387F(\mathrm{Pr})(\mathrm{Ra}(T))^{1/6})^2$$

where $F(\mathrm{Pr}) = (1 + (0.492/\mathrm{Pr})^{9/16})^{-8/27}$. The minimum and the maximum Nusselt numbers computed using this equation for the limiting Rayleigh numbers in Table 12 are 4.07 and 6.11, respectively.

Constant heat flux vertical surface [107]

$$\mathrm{Nu} = 1.2G(\mathrm{Pr})^{0.2}\mathrm{Ra}(q)^{0.2}$$

where $G(\mathrm{Pr}) = \mathrm{Pr}/(4 + 9\mathrm{Pr}^{0.5} + 10\mathrm{Pr})$. The minimum and maximum Nusselt numbers from this correlation are 5.28 and 7.86, respectively.

Protruding block on a vertical surface, aspect ratio = 2.5, [106]

For $1 \cdot 10^6 < \mathrm{Ra}(q) < 4 \cdot 10^6$, Nu varies from 10 to 12.

Fully developed flow for an array of protruding blocks, aspect ratio = 2, [108]

For $10^3 < \mathrm{Ra}(T) < 10^4$, Nu varies from 5 to 8.

Cuboid Model for an isothermal block of dimensions $H \times B \times L$, $\mathrm{Ra}(T) < 10^{11}$, [109]

Table 12 Average Nusselt Number as a Function of Rayleigh Number; (Ra(T) ≥ 9290 corresponds to the larger block)

$\mathrm{Ra}(T) \cdot 10^{-3}$	2.48	3.35	3.89	9.29	13.3	14.9	17.3
$\mathrm{Ra}(q) \cdot 10^{-4}$	8.7	12.7	15.1	28.7	44.3	53.0	63.6
Nu	13.2	13.5	13.8	14.7	16.0	17.1	17.6

$$\mathrm{Nu} = \mathrm{Nu}_c + F(\mathrm{Pr})G\mathrm{Ra}^{0.25}$$

where

$$\mathrm{Nu}_c = \frac{3.192 + 1.868\left(\frac{L}{H}\right)^{0.76}}{\left(1 + 1.189\frac{L}{H}\right)^{0.5}}$$

$$G = 2^{1/8}\left(\frac{H(L+B)^2}{(LB + H(L+B))^{1.5}}\right)^{0.25}$$

$$F(\mathrm{Pr}) = \frac{0.67}{\left(1 + \left(\frac{0.5}{\mathrm{Pr}}\right)^{9/16}\right)^{4/9}}$$

For the range of Rayleigh numbers given in Table 12, this equation gives Nusselt numbers in the range of 4.75 to 7.45.

The qualitative agreement of the local Nusselt numbers of the present study with [106] is good. Discrepancies are possible in the average Nusselt number since these authors use thermocouples to determine the local Nusselt number, resulting in loss of resolution, especially near the peak values. It is clear that the flush heater correlations substantially underpredict the average Nusselt number. As discussed by Park and Bergles [105], this discrepancy is due to the inapplicability of large plate correlations for short segments, especially near the leading edge. Conduction losses to the supporting plate is significant for small surfaces and lead to a higher measured Nusselt number. The cuboid model also underpredicts the Nusselt number because it is primarily designed for a fin assembly and not an isolated copper block. The Nusselt number for a block located in an array is smaller than for a single block since the fluid approaching the block is preheated and the thermal boundary-layer over the vertical face is thick. For the isolated heated surface considered in the present work, the boundary-layer thickness (Fig. 36) is zero at the leading edge and at all Rayleigh numbers except the lowest value.

7.1.3 Closure. Heat transfer in natural convection from an isolated protruding heater is found to be larger than that computed from correlations for a flush heater, a large cuboid, and data for an array of blocks. Interferometric study shows the local Nusselt number over the vertical face of the copper block to be quite large. This factor along with conduction to the supporting plate in the vertical direction provides the reasons for this difference.

7.2 Transient Convection in a Two-Dimensional Square Cavity

An interferometric study of transient natural convection in a long air-filled square cavity is reported. The top and bottom walls of the cavity are maintained at uniform temperatures at all times in an unstably stratified configuration. Three different Rayleigh numbers namely $8.79 \cdot 10^4$, $1.98 \cdot 10^5$, and $3.38 \cdot 10^5$ have been considered. The orientation of the light beam is maintained parallel to the longest dimension of the cavity. The fringes thus obtained reveal depth-averaged isotherm patterns in the cavity at various instants of time. The image is filtered and the fringes are thinned using image processing operations. Subsequently, the local and average heat transfer parameters in the experimental setup have been computed. Results of the present study show that the onset of flow in the cavity is bicellular. However, the flow is unicellular for the most part of the transient. The flow becomes increasingly vigorous with time and the average Nusselt number of the cavity is a maximum at steady state.

Buoyancy-driven flow in an air-filled cavity heated from below is a problem of fundamental as well as practical importance. A summary of experimental and theoretical results including several correlations for buoyancy-dominated flows is presently available [89]. These results pertain essentially to steady-state situations, with only a few numerical results being available for transient convection. One of the principal difficulties associated with transient flows is the measurement of the wall heat flux. Energy balance methods require careful accounting of losses and are simple to use only after steady state has been reached. In contrast to this, optical methods of measurement have several advantages. These include non-intrusiveness, absence of inertia while following transients, and the ability of a light beam to scan a flow field rather than the flow property at a point. Besides they can be used for qualitative as well as quantitative analysis of the problem at hand since the fringe spacing or the fringe slope can be related to the fluid temperature or the temperature gradient. The fringe thickness, however, places a lower limit on the length scales that can be resolved by the image.

Interferometric study of natural convection in a two-dimensional cavity whose side walls are heated has been reported earlier [108]. A similar study for a horizontal cylindrical annulus has also been described [109]. The study that comes closest to the present work is that of Eckert and Carlson [110] where the effect of wall conduction on natural convection in a square cavity has been presented using interferometry. The bottom-heated/top-cooled configurations is one of the several arrangements considered in Eckert and Carlson [110]. Features such as plume formation and fringe symmetry about the vertical plane have been observed and these are similar to the results obtained in the present work. However, there are significant differences arising from initial and boundary conditions and in the data reduction procedures.

The present work is concerned with visualizing isotherms in a square cavity at various instants of time. The top and bottom walls of the cavity are respectively cold and hot and their temperatures are maintained constant for all time. This is the classical Rayleigh–Benard problem with confining side walls. The original problem of convection in an infinite fluid layer of small thickness admits three-dimensional cel-

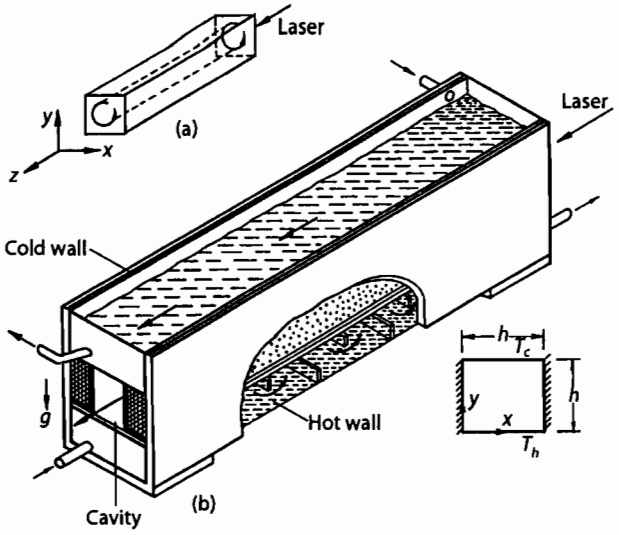

Figure 38 (a) Flow patterns in an infinite fluid layer and a square cavity; (b) schematic of the test cell.

lular flow as a solution. This is, however, considerably modified in the presence of confining side walls [111, 112] and at higher Rayleigh numbers. The formation of longitudinal rolls with their axes aligned normal to the shortest side has been observed in experiments on a horizontal fluid layer [41]. It is to be expected that when symmetry planes between adjacent cells are replaced by adiabatic walls, there will be no fundamental change in the flow pattern. This assumption has also been made implicitly in Tolpadi and Kuehn [8]. Fluid contained in the cavity whose vertical cross-section is a square and is long in the third dimension in the horizontal plane, is thus expected to exhibit cellular motion with the cell axis parallel to the longest side (Fig. 38(a)). If the length exceeds a critical value, two cells with the same direction of vorticity appear in the cavity. Since the cells are unidirectional, the temperature distribution within the two cells is similar. Hence, the average temperature distribution obtained by optical projection is representative of the flow field at any section along the cavity length.

Interferograms have been obtained in the present work by orienting the light beam parallel to the longest dimension of the cavity. Rayleigh numbers considered in the study are $8.79 \cdot 10^4$, $1.98 \cdot 10^5$, and $3.38 \cdot 10^5$. These are large in comparison to the critical Rayleigh number for the infinite fluid layer. These are, however, close to the critical value for a cavity with confining side walls [113]. Fringe patterns have been thinned using image processing operations. The thinned fringes near the cold wall have been used to compute the local Nusselt number. Images have been acquired during the transient evolution of the thermal field as well as at steady state. The images show distinct flow patterns during the early transient phase in comparison to steady state.

The apparatus used to study buoyancy-driven motion of air in a cavity is shown in Figure 38(b). The cavity is of a square cross-section with its width and height being adjustable in the range of 4 to 6 cm. The top wall is cooled with the help of chilled water from a constant temperature bath to a temperature of around 10°C, while the bottom wall is maintained at a temperature of around 25°C (close to room temperature). The temperatures of both the walls are maintained constant for the entire duration of the experiment. In the present study, special precautions have been taken so that the top and bottom walls attain a uniform temperature in a very short time. This is accomplished by making the walls out of thin brass sheets and exposing them to large volume flow rates of water. The side walls are made of 12.5-mm thick perspex sheets and padded using thermocole insulation. To avoid temperature nonuniformities at corners, the cavity is made smaller than the respective tanks containing hot and cold water. The upper wall is cooled to a temperature below the ambient value and convection is initiated in this part of the cavity. The heat transfer rates at the hot and cold walls are unequal during the transient process and approach each other at steady state. Since the active boundary in the present work is the cold upper wall, the heat transfer rates have been computed in this region.

The cavity used in the present work is 74 cm long, thus giving an aspect ratio of 15 to 20. As stated earlier, the resulting flow is expected to be in the form of cells with an axis parallel to the longer side. The light beam of the interferometer averages the temperature field along the length of the cavity. The temperatures of the hot and cold walls are measured using ten 18 gage chromel-alumel thermocouples on each surface. Temperature on each surface is found to be constant to within ±0.2°C along the path of the light beam. The hot and the cold walls of the cavity reach steady state in less than five minutes, while the flow reaches steady state in about two hours. Environmental conditions in the laboratory are stable for three hours and data is collected over this duration.

At the Rayleigh numbers considered in the present investigation the fringes in the core of the cavity are not strictly stationary even after a sufficiently long time is allowed to elapse. To estimate the extent of this uncertainty in the heat transfer data the following procedure has been adopted. Five interferometric images are recorded at the camera snapping speed of one picture every 20 minutes at predetermined instants of time. This time interval is required to transfer light intensity data over 512×512 pixels from the camera to the PC. The Nusselt number at a given time is computed as the average of the Nusselt numbers evaluated at 20 minute intervals. The uncertainty in this average Nusselt number in relation to the instantaneous value is as high as ±20% with 95% confidence.

The time required to collect five images consecutively is 100 minutes. This time is, however, small in comparison to the time scale of evolution of flow. The first image is typically collected after 8 to 10 minutes and the flow reaches steady state after 2 to 3 hours. Hence, the response time of the measurement system can be considered to be negligible.

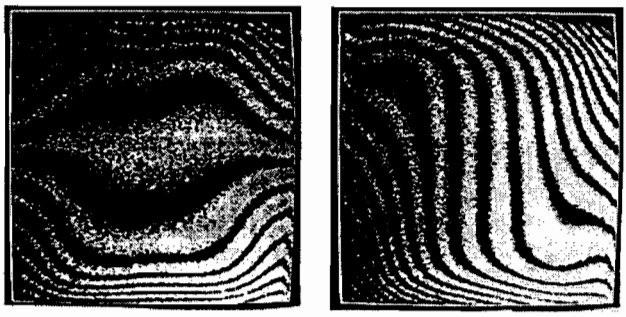

(a) (b)

Figure 39 (a) Fringe patterns at steady state in a square cavity; (b) wedge fringes at steady state in a square cavity ($Ra = 8.79 \cdot 10^3$).

7.2.1 Steady State. Results are presented below for three Rayleigh numbers namely, $8.79 \cdot 10^3$, $1.98 \cdot 10^4$, and $3.38 \cdot 10^4$ corresponding to cavity sizes of 4.0, 5.0, and 5.7 cm respectively. Figure 39(a) shows the overall distribution of fringes in the full cavity at steady state attained with a Rayleigh number of $8.79 \cdot 10^3$. The spacing among fringes near the wall is seen to be small around the midplane of the cavity and gradually increases towards its edges. Since each fringe is an isotherm a small fringe spacing gives rise to a large local heat flux. The largest local heat flux on the cavity walls at steady state occurs around the midplane of the cavity. The fluid accelerates on one side of the midplane, reaches a maximum at this point, and decelerates to small values on the other side of the cavity, as it approaches the side walls. The overall flow pattern in the cavity is hence unicellular.

Figure 39(b) shows wedge fringes in the cavity at steady state at the same Rayleigh number of $8.79 \cdot 10^3$. The wedge fringes are obtained by deliberately misaligning the mirrors of the interferometer so that under zero flow conditions a set of parallel fringes are seen. When temperature gradients are present in the test cell the fringes are curved and the fringe slope is a measure of the local heat flux. The direction in which the fringes are displaced depends on the direction of the local fluid velocity. Figure 39(b) shows that the fringes are displaced to the right near the bottom wall and to the left near the top wall. This confirms the result from the infinite fringe setting (Fig. 39(a)) that the flow in the cavity is unicellular with the roll moving in an anticlockwise direction.

The intrinsic symmetry of the cavity and associated boundary conditions affords the formation of many cells whose axes are parallel to the cavity length. A single cell is preferred over other configurations owing to several factors that include mild imperfections in the experimental apparatus. A qualitative explanation can be given in terms of the energy requirement to sustain multicellular flow. In a square cross-section and at moderate Rayleigh numbers, one can expect unicellular flow to

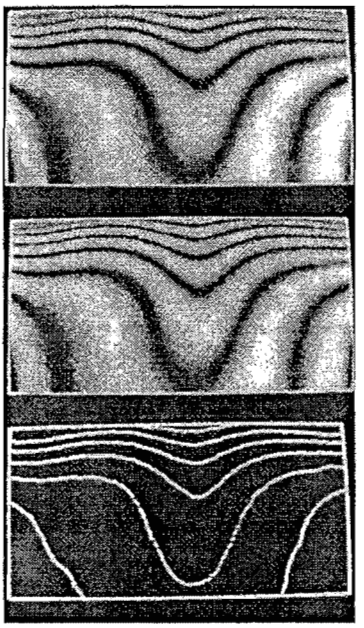

Figure 40 Fringes near the cold wall during transient convection. (a) Original, (b) Fourier-filtered, and (c) Fringe- extracted Image. Ra = $8.79 \cdot 10^3$, Fo = 6.34.

consume the least energy and hence be most likely to appear in the cavity. The present set of experiments, however, provide evidence of bicellular flow for small-time and is discussed in the following section.

7.2.2 Evolution of the Flow Field. Figures 40(a–c) respectively show the original fringe pattern, the Fourier-filtered image and, the fringe skeleton extracted using the procedure given earlier. The figure represents fringe patterns in the vicinity of the cold upper wall during the transient period at a Rayleigh number of $8.79 \cdot 10^3$ and a Fourier number of 6.34. Figures 41(a–c) show the original and the processed fringes near the cold wall for the same Rayleigh number at a Fourier number of 91.26. The near-wall fringes are nearly stationary at this time and steady state can be assumed to have been reached.

The interferograms shown above have been obtained at the infinite fringe setting and hence fringes are coincident with isotherms. At the centre of the cold wall, the isotherms in Figure 41 are straight and hence correspond to parallel flow. A displacement of the isotherms is indicative of transverse flow. This is seen near the side walls in Figure 41 where flow moves up and down in the vertical direction to complete a loop. Displacement of the isotherms is also seen at the centre of the cavity in Figure 40. This is proof of the existence of two convection cells during the early stages of evolution of fluid movement.

7.2.3 Heat Transfer. Table 13 compares the average Nusselt number computed in the present work at the end of three hours with the steady state correlation given in

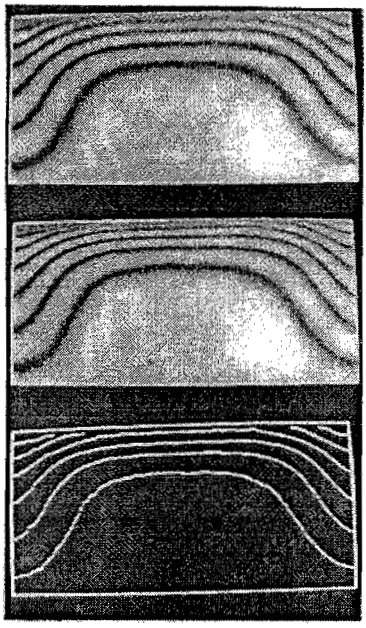

Figure 41 Fringes near the cold wall at steady state. (a) Original, (b) Fourier-filtered and (c) Fringe-Extracted Image, Ra = $8.79 \cdot 10^3$, Fo = 91.26.

Gebhart et al. [89]. This correlation is applicable for a rectangular cavity with a moderate aspect ratio, but is independent of the aspect ratio itself. It is given as

$$\mathrm{Nu} = 1 + 1.44\left[1 - \frac{1708}{\mathrm{Ra}}\right] + \left[\left(\frac{\mathrm{Ra}}{5830}\right)^{1/3} - 1\right] \tag{25}$$

for $\mathrm{Ra} < 10^6$. The comparison is seen to be fairly good, the values obtained in the present investigation being about 4 to 8% lower than the values given by the correlation.

The variation of the Nusselt number for each half of the cavity and for the cavity as a whole as a function of time are given in Table 14. A study of the transient data reveals the following features. For a given Rayleigh number, the average Nusselt number in the cavity is a maximum as steady state is reached. This is quite consistent with the fact that the flow (measured in terms of the maximum velocity or minimum stream function) is initially quiescent and increasingly becomes vigorous with the

Table 13 Average Steady State Nusselt Number in a Square Cavity

$\mathrm{Ra} \cdot 10^{-4}$	Nu (present)	Nu [89]	% difference
8.79	3.56	3.89	8.5
19.8	4.35	4.67	6.9
33.8	5.07	5.30	4.3

Table 14 Average Nusselt Number as a Function of Fourier Number

$Ra = 8.79 \cdot 10^4$				
Fo	6.34	11.5	35.7	91.3
Nu (left)	2.21	3.42	3.65	3.45
Nu (right)	2.06	3.11	2.45	3.68
Nu (cavity)	2.13	3.26	3.06	3.56
$Ra = 1.98 \cdot 10^5$				
Fo	9.14	13.7	20.3	60.94
Nu (left)	2.24	2.52	4.53	4.89
Nu (right)	2.64	2.79	3.77	3.81
Nu (cavity)	2.44	2.66	4.15	4.35
$Ra = 3.38 \cdot 10^5$				
Fo	8.93	31.9	47.4	65.7
Nu (left)	2.87	4.47	4.54	5.89
Nu (right)	3.33	4.49	4.31	4.26
Nu (cavity)	3.1	4.48	4.42	5.07

passage of time. The increase in Nusselt number is however not found to be monotonic. The thermal field is seen to be symmetric with respect to the vertical axis dividing the cavity only at the lowest Rayleigh number ($Ra = 8.79 \cdot 10^3$). It is not symmetric at higher Rayleigh numbers, both during the transient as well as steady state. This is also seen in the average Nusselt numbers obtained for each half of the cavity. Hence, analyses that assume symmetry are likely to yield incorrect results.

Table 14 shows that at any Rayleigh number the initial increase in Nusselt number is rapid. This is followed by a slow transient until steady state is reached. This behavior can be explained as follows. The initial increase in Nu is controlled by the formation of boundary-layers near the hot and the cold walls and the characteristic distance is this boundary-layer thickness. Hence, the characteristic time over which initial changes in Nu are significant is quite small. At larger times heat transfer is established across the cavity dimension and the changes in Nu occur at a slower rate.

For all three Rayleigh numbers studied, the initial fringe patterns are qualitatively identical to those shown in Figure 40(a). The fringes in this figure show a thick boundary-layer and a plume descending downwards along the vertical axis of the cavity. This suggests that the flow is initially bicellular. At later times the flow pattern reverts to a unicellular form with nearly constant boundary-layer thickness over the horizontal cavity walls (Fig. 41(a)). There is a considerable amount of uncertainty in the exact time instant at which this transition occurs. It corresponds approximately to a Fourier number of 10 while steady state is reached at around Fo = 50. Once the flow becomes unicellular, transients are characterized by the formation of newer fringes. This represents the penetration of the thermal front into the bulk of the fluid. The process continues until steady state is reached.

Figures 42(a–c) show the local Nusselt number at the cold wall of the cavity at $Ra = 8.79 \cdot 10^3$, $1.98 \cdot 10^4$, and $3.38 \cdot 10^4$ respectively. Transient as well as steady state distribu-

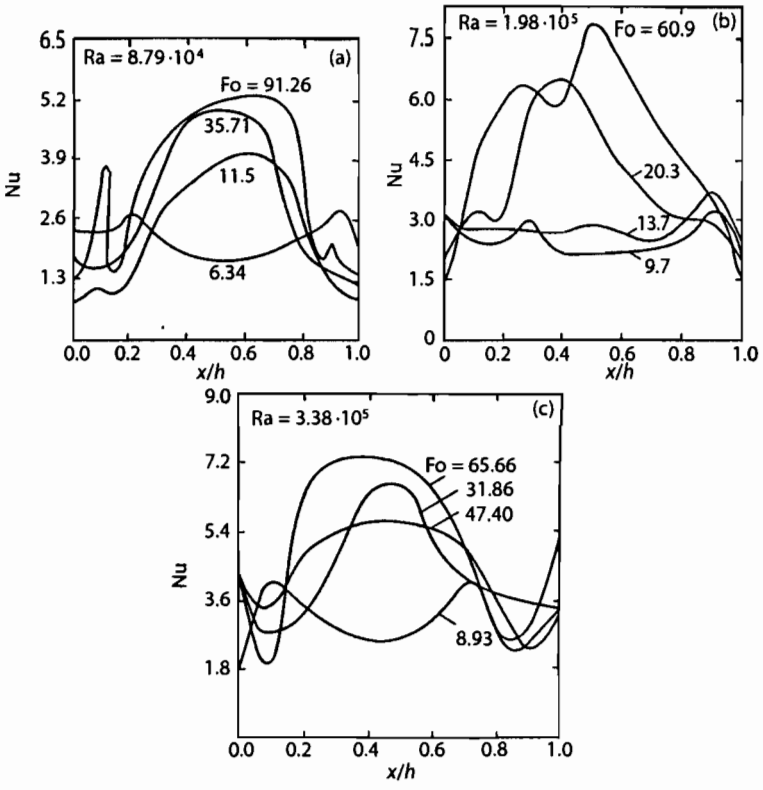

Figure 42 Local Nusselt number as a function of distance and time. (a) $Ra = 8.79 \cdot 10^3$, (b) $Ra = 1.98 \cdot 10^4$ and (c) $Ra = 3.38 \cdot 10^4$.

tions are shown in these figures. The corner regions of the cavity are zones of high heat transfer and this is seen as spikes in the distribution of the local Nusselt number. These distributions show a minimum in the local Nusselt number at the midpoint of the cavity walls during the early transient. As stated above, this corresponds to the formation of two convection cells in the test cell. In contrast, the local Nusselt number reaches a maximum around the same point at steady state. The local values of the Nusselt number differ considerably from their average computed over the cavity width. In particular the average value is sensitive to the choice of the mathematical definition of an average. An average based on Simpson's rule has been used in the present work.

7.2.4 Closure. Transient Rayleigh–Benard convection in a square cavity with rigid walls has been experimentally studied. Results show that the time-evolution of flow is initially bicellular, while it is unicellular at steady state. The sense of unicellular motion depends on the experimental bias. Experiments also show a large variation with distance in the local Nusselt number at the cold wall. The evolving flow

shows symmetry at the lowest Rayleigh number studied. Symmetry is however lost when the Rayleigh number is increased. The average cavity Nusselt number reaches a maximum at steady state.

7.3 Convection in a Horizontal Differentially Heated Fluid Layer

7.3.1 Overview. An experimental study of Rayleigh–Benard convection in an intermediate aspect ratio box that is square in plan is reported. An intermediate range of Rayleigh numbers has been considered in the study. The fluid employed is air. A Mach–Zehnder interferometer is used to collect the line-of-sight projections of the temperature field in the form of interferometric fringes. Images have been recorded after a sufficient time has elapsed for the initial transients to have been eliminated. Interferograms have been collected from four to six view angles. These are used to obtain the three-dimensional temperature field inside the cavity by using tomography. The MART algorithm has been used for the inversion of the projection data. The convergence of the iterative inversion procedure was unambiguous and asymptotic. The reconstructed temperature field with a subset of the total data was found to be consistent with the remaining unused projections.

Results for two Rayleigh numbers, namely 13900 and 40200 have been reported. These were found to correspond to two distinct flow regimes. At these Rayleigh numbers, a well-defined steady state was not observed. At the lower Rayleigh number, the fringes away from the wall showed mild unsteadiness. At the higher Rayleigh number, the fringes were found to switch between two patterns. Results for the dominant mode alone have been presented for this problem. At a Rayleigh number of 13900, three-dimensional flow structures, whose influence is equivalent to longitudinal rolls have been observed. At a Rayleigh number of 40200, cubic cells have been noted in the cavity. The associated flow pattern is inferred to be a plume rising from the heated plate. The local Nusselt number variation is seen to be consistent with the observed flow patterns.

7.3.2 Motivation. Rayleigh–Benard convection in horizontal fluid layers is a problem of fundamental as well as practical importance. The flow pattern associated with this configuration shows a sequence of transitions from steady laminar to unsteady flow and ultimately to turbulence. This configuration has been studied by analytical and computational techniques as well as by experiments to understand the physics involved in the transition phenomena. Although extensive work has been reported, many questions remain to be answered. Many of the global features observed by numerical solutions are supported by experimental observations. However, a closer comparison in terms of thermal fields and convection patterns remains to be carried out. With renewed interest in understanding nonlinear systems and simultaneously the availability of powerful computers, there has been a revival of interest in Rayleigh–Benard convection. The experimental technique has also been strengthened by the availability of optical methods to visualize the flow phenomena and computers for data storage, processing, and analysis.

Interferometric study of Rayleigh–Benard convection for two Rayleigh numbers (13900 and 40200) is reported in the present work. The cavity is square in plan and the aspect ratio employed leads to an intermediate aspect ratio box. The aspect ratio is defined as the ratio of the horizontal dimension to the height of the cavity. The fluid considered is air. Results have been presented for flow patterns that develop at long-time, that is after the initial transients have been eliminated. Interferograms collected from several line-of-sight projections have been processed to reconstruct the complete three-dimensional temperature field. The multiplicative algebraic reconstruction technique in a modified form called AVMART has been used as the preferred tomographic algorithm (Section 6.5).

7.3.3 Rayleigh–Benard Convection. The present state-of-understanding of Rayleigh–Benard convection is discussed below. In the simplest form, the flow configuration is comprised of a horizontal fluid layer confined between a pair of parallel horizontal plates. The fluid is differentially heated by maintaining the lower surface at a higher temperature compared to the top. This situation produces a top-heavy arrangement that is unstable. The dimensionless quantity that characterizes the buoyancy-driven flow is the Rayleigh number defined as

$$\mathrm{Ra} = \frac{g\beta(T_{\mathrm{hot}} - T_{\mathrm{cold}})h^3}{\nu\alpha} \tag{26}$$

When Ra is below a critical value, the gravitational potential is not sufficient to overcome the viscous forces within the fluid layer. For Rayleigh numbers above the critical value, a steady flow is established. Subsequently, flow undergoes a sequence of transitions, finally resulting in turbulence.

Transitions in Rayleigh–Benard convection depend on a Rayleigh number, a Prandtl number, and the cavity aspect ratio. Additionally, there is an effect of the geometric structure of the side walls being straight or curved [113]. The present discussion is restricted to a rectangular cavity. For a fluid layer with an infinite aspect ratio, the first transition, namely the onset of fluid motion, occurs at a Rayleigh number of 1708, irrespective of the Prandtl number. The associated flow pattern is in the form of hexagonal cells. The general effect of lowering the aspect ratio is to stabilize the flow due to the presence of the side walls and thus increase the critical Rayleigh number [116]. All subsequent transitions are Prandtl number dependent. The present discussion is devoted to Prandtl numbers in the range 0.7–7, for which some general conclusions can be drawn.

Flow patterns in rectangular cavities can be divided into three main categories, depending on the aspect ratio. These are small ($\approx$ 2–10), intermediate ($\approx$ 10–30), and large ($\approx$ 30–60) aspect ratio boxes. Transition and chaos in a small aspect ratio enclosure with water has been experimentally studied by Nasuno et al. [117]. Their data is in good agreement with the stability diagram of Busse and Clever [118]. In a large aspect ratio enclosure, it has been shown that flow beyond the critical Rayleigh number is

always time-dependent and nonperiodic (see Ahlers and Behringer [119]). In contrast, a large number of bifurcations have been recorded both experimentally as well as in numerical studies in small aspect ratio enclosures. Information regarding intermediate aspect ratio enclosures is sparse. The transition sequence appears to be via the formation of longitudinal rolls that are aligned with the shorter side, polygonal cells; roll-loss and displacement; and finally towards turbulence. The literature on convection in low and intermediate aspect ratio enclosures is briefly presented below.

When the Rayleigh number is close to the critical value for the onset of convection, hexagonal convection cells have been observed both experimentally and in computation [113]. With a further increase in the Rayleigh number, stable two-dimensional longitudinal rolls have been observed. Krishnamurti [120] is one of the earliest authors to conduct an experimental study and observe roll patterns. Much later, Kessler [121] obtained steady rolls formation through a numerical simulation. With further increase in the Rayleigh number, the two-dimensional rolls were seen to bifurcate slowly to three-dimensional rolls, showing variation in shape along the roll axis. The three-dimensional rolls were found to be steady over a range of Rayleigh numbers. For further increase in the Rayleigh number, a loss-of-roll phenomena was observed. Kirchartz and Oertel [116] have shown for a box of small aspect ratio the transition from four rolls to three rolls and finally to two rolls. Simultaneously, three-dimensional rolls become unstable and a periodic motion of the roll system begins along its axis. The critical Rayleigh number for the onset of oscillatory rolls is shown to be in the range of a Rayleigh number of 30000 for air (Pr = 0.71) [121]. This critical Rayleigh number increases with the increase of the Prandtl number. The frequency of oscillation is not a strong function of the Rayleigh number, but increases slowly with increase in the Rayleigh number. Kessler [121] has also observed the exchange of mass between different rolls. This is due to a periodic motion in the location of the vertically upward and downward flow.

The evolution of time dependence and the nature of bifurcations sequence in intermediate aspect ratio boxes is more complex compared to both low and high aspect ratio boxes. Hence there is no general agreement in the literature. Krishnamurti [122] has shown that convective flow for air in a box of aspect ratio of around 12 will become unsteady at a Rayleigh number greater than 9000. The unsteadiness referred to here was identified through the velocity field by introducing neutrally buoyant particles. This approach should be contrasted with interferometry, where the temperature field is recorded in terms of fringes of finite thickness. It is likely that a marginally unsteady flow field will continue to generate a stable set of fringe patterns. In broader terms, the stability boundaries identified by Krishnamurti [122] can be interpreted as the limit below which flow would be steady and above which the the possibility of unsteadiness is high. Steady flow can still be observed at a higher Rayleigh number for certain combinations of aspect ratios and length-to-breadth ratios. Flow reversal from unsteady to steady flow has been shown by the numerical study of Mukutmoni and Yang [123] for a small aspect ratio box. The intermediate aspect ratio box on the other hand is an approximation of the infinitely extended horizontal fluid layer only to a limited extent. Mukutmoni and Yang [102] have seen

in their numerical work that the side walls play a role even when the aspect ratio is large. Kolodner et al. [124] have reported the formation of stable rolls from experimental studies at the onset of convection. The Rayleigh number was increased by slowly heating the lower wall. The stable pattern was characterized by rolls of uniform size. The first bifurcation was observed around a Rayleigh number of 10200, where the rolls were seen to deform. The deformation in the size of the roll and time dependent oscillations were used to identify the transition Rayleigh numbers. The loss-of-roll phenomena, i.e., a reduction in the number of rolls was observed around a Rayleigh number of 11000. A ten-roll initial structure was found to have six rolls at a Rayleigh number of around 20400. The complete time dependence of the flow pattern was observed near a Rayleigh number of 30600. The six-roll pattern with time dependent flow reappeared at a Rayleigh number of 68000. Mukutmoni and Yang [102] have also shown the loss of roll phenomena as the Rayleigh number increased in an intermediate aspect ratio box. Maveety and Leith [125] have explored the relationship between heat flux characteristics and loss-of-roll structure via experiments in rectangular cavities of intermediate aspect ratio, with air as the working fluid. They have found the quadratic increase in heat flux to relax to a linear growth with increasing aspect ratio, mainly due to a loss of rolls.

The present study is concerned with mapping the full three-dimensional temperature field in an intermediate aspect ratio box, using interferometric projections followed by tomography. In an earlier study, the authors have reported experiments at a Rayleigh number of 34800, using interferograms of the central core of the fluid layer [79]. In the present work, Rayleigh numbers of 13900 and 40200 have been selected for the experiments. The fluid layer has been completely mapped and a larger number of projections have been employed. At these Rayleigh numbers, longitudinal rolls and polygonal cells are to be expected. The objective of the present work is to explore under these conditions the detailed thermal field in the fluid layer.

7.3.4 Experimental Details. The apparatus used to study convection in the horizontal layer of air is shown in Figure 43. The cavity employed was 500×500 mm^2 in plan, the vertical depth being adjustable. Two different vertical depths were used in the present study to generate the two Rayleigh numbers. For a Rayleigh number of 13900, the vertical depth was 20 mm. For the higher Rayleigh number of 40200, the vertical depth was increased to 26.8 mm. The aspect ratio was thus maintained at 25 and 18.6 respectively. The lowering of the aspect ratio was seen to reduce the extent of unsteadiness in the convection pattern at the higher Rayleigh number. The fluid layer was confined by two aluminium plates of 5 mm thickness above and below. The side walls comprised of two superposed layers of perspex sheets, each 10 mm thick. A small window in the side walls enabled the recording of interferograms. The top wall was cooled and the bottom wall was heated by pumping water continuously from constant temperature baths. Special attention was given to ensure that isothermal conditions prevailed at the aluminium plates. This was achieved by circulating a large volumetric flow rate of water over the highly conducting aluminium plates. To produce a Rayleigh number of 13900, the top wall is cooled to a temperature of

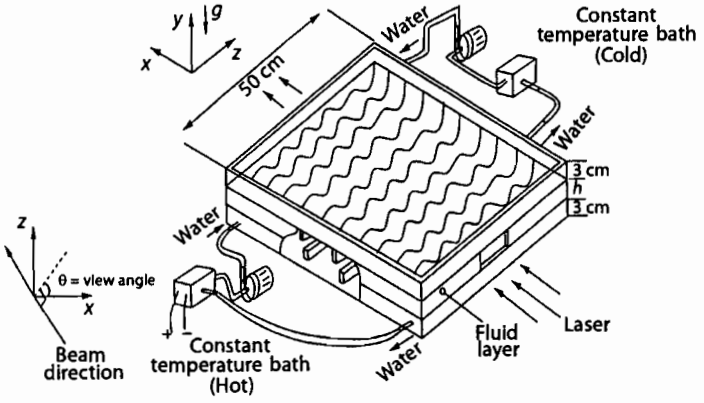

Figure 43 Schematic of the experimental apparatus.

13.4°C while the bottom wall is heated to a temperature of 30.5°C, for a vertical depth of 20 mm. For Ra = 40200, the temperature difference was increased to 21.1°C by cooling the upper plate to 12.4°C and heating the bottom plate to 33.5°C, the cavity height being 26.8 mm. The ambient temperature was 21.7°C in all the experiments. Both walls were maintained at their respective temperatures to within ±0.2°C for the complete duration of the experiment. The temperatures of the walls were continuously monitored using thermocouples connected to a 30-channel temperature recorder. The entire test cell was placed inside a chamber made of a plastic sheet to eliminate the influence of external air currents. The test cell was mounted over a traversing mechanism capable of both translational and rotational motion. The traversing mechanism was padded with a rubber sheet, 30 mm thick, to damp external vibrations. The interferometer was itself mounted on four pneumatic legs. A variety of tests were carried out to ensure that the convection patterns in the fluid layer were insensitive to external disturbances such as floor vibration and the flowing water. It was thus established that air convection was driven by the temperature difference alone. The hot and cold walls bounding the cavity were found to reach steady state in about 30 minutes whereas the convection pattern reached steady state in three to four hours. The experiment was conducted beyond four hours to eliminate the initial transients and obtain a dynamic steady state.

The interferometric fringes associated with the convective flow pattern can be interpreted as the line-of-sight projection of the refractive index field. This in turn depends on the temperature field in the fluid layer. Using the projection data, the three-dimensional temperature field has been determined using a tomographic algorithm. Reconstruction of the three-dimensional temperature field requires that the projection data employed be complete. In the present work, this requires the recording of interferograms for the entire width of the fluid layer along different view angles (Fig. 43). The laser beam diameter being 70 mm, the flow field of width 500 mm was mapped com-

pletely by translating the test cell with the traversing mechanism. View angles of 0°, 30°, 60°, 90°, 120°, and 150° have been considered in the present study for the Rayleigh number of 13900. In these experiments, the fringes near the solid surfaces were seen to be stationary. Hence, for a given projection angle, there was no difficulty in maintaining the continuity of fringes from one projection record to the next. Mild unsteadiness however was observed in the fringes near the central region of the fluid layer, midway between the two horizontal walls. To circumvent this difficulty, several images were recorded at a given position and those giving the best continuity were chosen for analysis. Axial tomography that has been applied to the present work requires that the axis of rotation be maintained strictly invariant from one projection to the next. This has been enforced in the experiments by matching the center of the test cell with the center of the traversing mechanism.

7.3.5 Uncertainty and Measurement Errors. Errors in the experimental data are associated with misalignment of the apparatus with respect to the light beam, image processing operations including filtering, thinning and assigning temperature to fringes, error amplification during three-dimensional reconstruction, and the intrinsic uncertainty in the convection process itself. Errors related to refraction effects have been found to be quite small. All experiments were conducted several times to establish the repeatability of the fringe patterns. Time-dependent movement of fringes was not a source of uncertainty in the present work at a Rayleigh number of 13900. However, at a Rayleigh number of 40200, two sets of convection patterns were seen to be formed. Analysis has been carried out for the fringe patterns that formed for the most part of the experiment. The associated uncertainty in the local Nusselt number was found to be ±20% with 95% confidence. At both Rayleigh numbers, the plate-averaged Nusselt number was found to be in good agreement with published correlations and is discussed in Section 7.3.8. The width-averaged temperature profile that represents energy balance across the cavity was also found to be unique and well-defined. Hence, the results obtained in the present work can be taken to be qualitatively meaningful.

7.3.6 Image Processing and Data Reduction. The three-dimensional reconstruction of the temperature field requires a noise-free set of projection data as input. Hence, prior to the calculation of the projection data in terms of the temperature, interferometric images have to be cleaned. Image processing operations employed in the present study are described in Section 4. The fringe thinning algorithm is described in Section 4.1.1.

The projection data of the temperature field in the fluid layer is available at this stage in the form of temperatures at locations defined by the fringe geometry. To apply a tomographic algorithm, the projection data is required over a uniform grid. In the present study, two-dimensional quadratic interpolation has been employed to transfer projection data from the fringe patterns to a uniform grid. The cavity height was discretized into 21 horizontal planes. The number of vertical columns at which interpolation was carried out for the 0° and 90° projections was 120. For the angular projections, the cavity width was effectively larger. However, the extreme ends of the

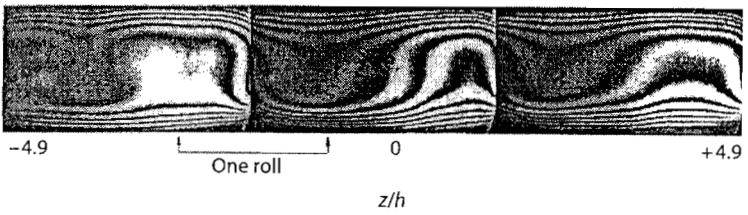

Figure 44 Original interferograms showing 5 full and 2 partial rolls at Ra = 13900, 90° projection.

cavity could not be used due to reduction in the path length of the light beam traversing the fluid layer. At these locations, there was a drastic reduction in the number of fringes and a corresponding increase in the fringe spacing. Hence, for angular projections, only 160 vertical columns covering 60% of the cavity width were considered. The error introduced in the projection data due to interpolation was found to be less than 0.01%.

Figure 44 shows a collection of original interferograms at a Rayleigh number of 13900 for a view angle of 90°. The roll formation, specifically five complete and two partial rolls are clearly seen here. For the cavity size studied, the number of rolls is in the range of 14–16. For compactness, thinned interferograms alone have been presented in this work. Figure 45 shows isotherms within the cavity for four different view angles at Ra = 13900. As discussed earlier, the isotherms completely corre-

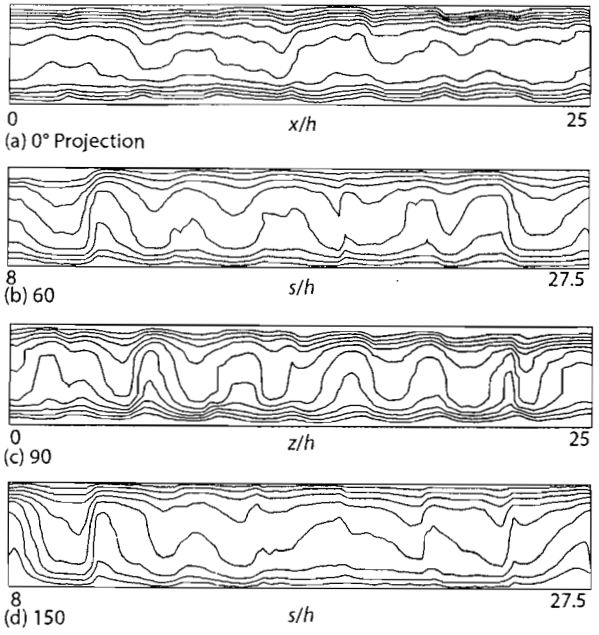

Figure 45 Thinned images of the cavity, Ra = 13900, (a) 0°, (b) 60°, (c) 90°, (d) 150° projections.

spond to the fringe skeleton of the 0° and 90° projections. At other view angles, the correspondence between fringes and isotherms is lost owing to changes in the path length traversed within the fluid layer. This is not a source of error since the geometric factor can be analytically accounted for. In the present work, the fringes have been mapped to temperatures over a grid and isotherms extracted from this data. Thus, thinned images for other view angles in Figure 45 show isotherms, determined from the interpolated grid values. Figure 46 shows thinned images of the fluid layer for a Rayleigh number of 40200 at view angles of 0° and 90°.

The correctness of fringe thinning, assigning fringe temperatures, and a check on the magnitude of interpolation errors have been examined by using the following result: At steady state, the width-average of the line integrals of temperature field plotted as a function of the vertical coordinate is independent of the projection angle. This is because the total energy transferred across the cavity is unchanged from one horizontal plane to the next. Figure 47 shows the variation of line integrals of the temperature field averaged over a horizontal plane as a function of the vertical coordinate measured from the cooled top wall for both 0° and 90° projections at a Rayleigh number of 13900. The corresponding graph for Ra = 40200 is shown in Figure 48. The S-shaped curve, characteristic of buoyancy-driven convection can be seen here. The curves for the two projections match closely and their slopes at the hot and cold walls are practically equal. The S-shaped curve for the angular projections have not been shown since the corresponding projection data does not span the entire width of the test cell. Temperatures in the 0° and 90° data have been subsequently corrected to ensure that between the two projections, the S-shaped curve is strictly unique. This step did not alter the isotherms in Figures 45 and 46 to any significant degree, but was expected to improve convergence of the tomographic inversion process.

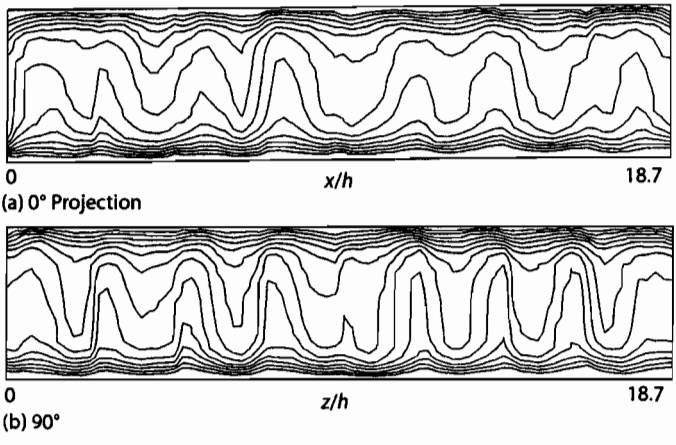

Figure 46 Thinned images of the cavity, Ra = 40200, (a) 0°, (b) 90° projections.

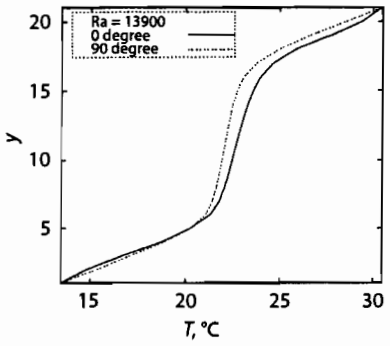

Figure 47 Width-averaged temperature profile in the cavity, Ra = 13900 ($y = 1$ is the top wall.)

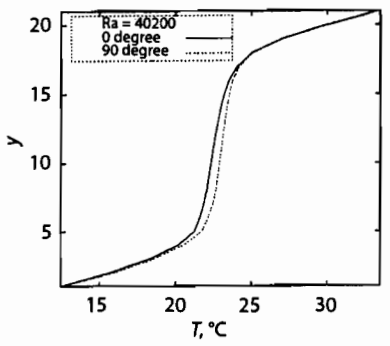

Figure 48 Width-averaged temperature profile in the cavity, Ra = 40200 ($y = 1$ is the top wall.)

7.3.7 Three-Dimensional Reconstruction Algorithm. The temperature data available on a Cartesian grid for each view angle represents the line integral of the temperature field in the fluid layer. Reconstruction of the three-dimensional temperature field from the projection data requires the use of tomographic algorithms. AVMART algorithm discussed in Section 6.5 has been used in the present analysis.

A check on the correctness of the reconstructed field was carried out along the following lines. For a Rayleigh number of 13900, six different sets of projections were collected. Of these, four projections were used to reconstruct the three-dimensional temperature field inside the cavity. The reconstructed field was used to compute the projections numerically at the two angles not included in the tomographic algorithm. These two projections could thus be used for direct comparison with the experimentally recorded interferograms. For the higher Rayleigh number of 40200, two complete sets of projections (0° and 90°) were recorded. Besides this, for view angles of 30° and 60°, projections of the near central region of the cavity over a width of 6.2 cm were collected to serve as a cross-check for the reconstructed field.

The comparison between the numerically generated projections and the experimentally recorded interferograms not utilized in reconstruction is now presented. The Rayleigh number is 13900, but similar checks were also carried out at Ra = 40200. The cross-checks have been carried out at view angles of 30° and 120° in terms of isotherms, Figure 49. The close match between the two sets of data confirms the correctness of the reconstructed temperature field. A similar cross-check was carried out in terms of local Nusselt numbers at these projection angles and the comparison was found to be good.

7.3.8 Results and Discussion. Results have been presented for two Rayleigh numbers, namely 13900 and 40200. The flow structure and roll pattern, temperature field over horizontal planes, and the wall Nusselt numbers have been reported. An earlier report of the present work at a Rayleigh number of 34800 with partial projection data

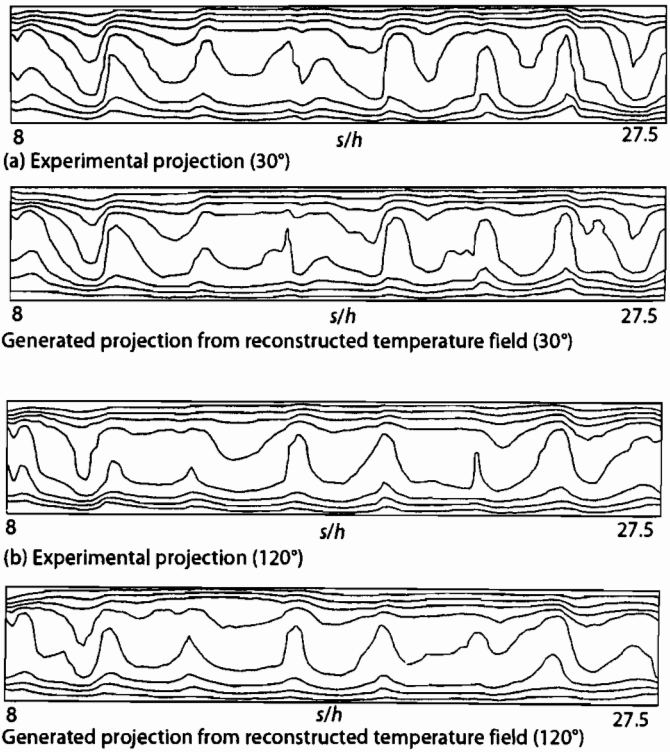

Figure 49 Comparison of experimentally obtained thinned images with generated projections for cross-check of reconstructed temperature field, (a) Ra = 13900, 30° projection, (b) Ra = 13900, 120° projection.

at two view angles has been reported elsewhere [79]. Experiments were conducted at a fourth Rayleigh number of 51800 as well. The flow field at this Rayleigh number was found to be completely unsteady with no noticeable periodicity. Hence images even at neighboring positions were seen to be uncorrelated. Tomographic interferometry of fully unsteady convection phenomena has been taken up as a topic for future research.

Convection at Ra = 13900. The experiments at a Rayleigh number of 13900 are considered first. Isotherms in the projection data at this Rayleigh number (Fig. 45) in the 0° and 90° projections indicate the formation of longitudinal rolls in the fluid layer. For a cavity square in plan, the orientation of the rolls is indeterminate in principle, and will depend on mild imperfections in the experimental apparatus and nonuniformities in the thermal boundary condition. In the present work, the roll axis is seen to be parallel to the 90° view angle. The rolls are stacked adjacent to one another, but the roll-width is not a constant. Despite the presence of a dominant flow pattern, the temperature field is fully three-dimensional, as can be seen from the lack of straightness of the isotherms in the 0° projection. At the onset of longitudinal rolls in the fluid layer, scale analysis suggests the formation of as many rolls as the aspect

ratio, 25 in the present experiment. The number of rolls seen in the projection data, Figure 45, is 15. The reduction in the number of rolls with increase in Rayleigh number finds support in the work of Kolodner et al. [124]. These authors have reported a decrease in the number of rolls from 10 to 6 in a 10:5:1 cavity for a Rayleigh number increasing up to 20000.

The loss-of-roll phenomena has been predicted using stability theory and summarized in Figure 2 of Busse and Clever [118]. This figure indicates that the movement of the flow state occurs along the stability boundary that separates skewed varicose (SV) instability from the knot (KN) instability in a direction of diminishing wavenumber. In the present set of experiments, the Rayleigh number was increased from zero to its final value in one step rather than in a gradual sequence. Hence, the transitions that would occur for a gradual change in Rayleigh number were not visible in the fluid layer. Thus the appearance of 15 rolls (instead of 25, as should happen if equal-sized square rolls were to be formed) at Ra = 13900 has been presented here, not as a transition point, but as a descriptor of the flow field.

For 25 rolls, the dimensionless wavenumber γ is π, while it decreases to 1.88 for 15 rolls. This places the flow regime in a state of oscillatory instability [118]. The mild unsteadiness in the fringe patterns can be associated with the oscillatory instability mechanism corresponding to a Rayleigh number of 13900 and a dimensionless wavenumber of 1.88.

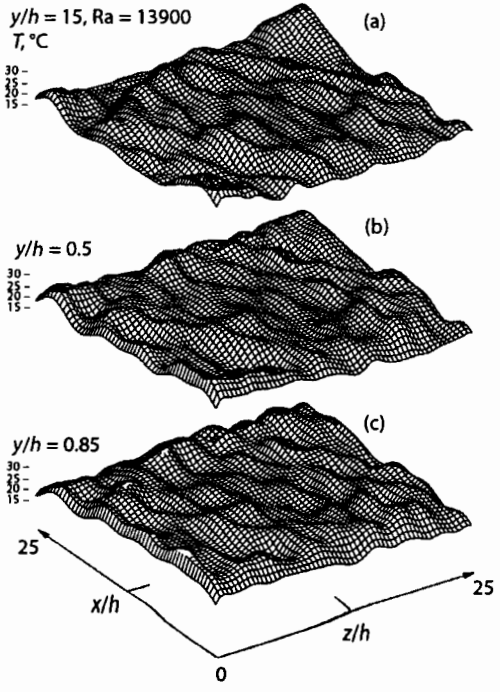

Figure 50 Temperature surfaces in the cavity at three horizontal planes, Ra = 13900, (a) y/h = 0.15, (b) y/h = 0.5, (c) y/h = 0.85.

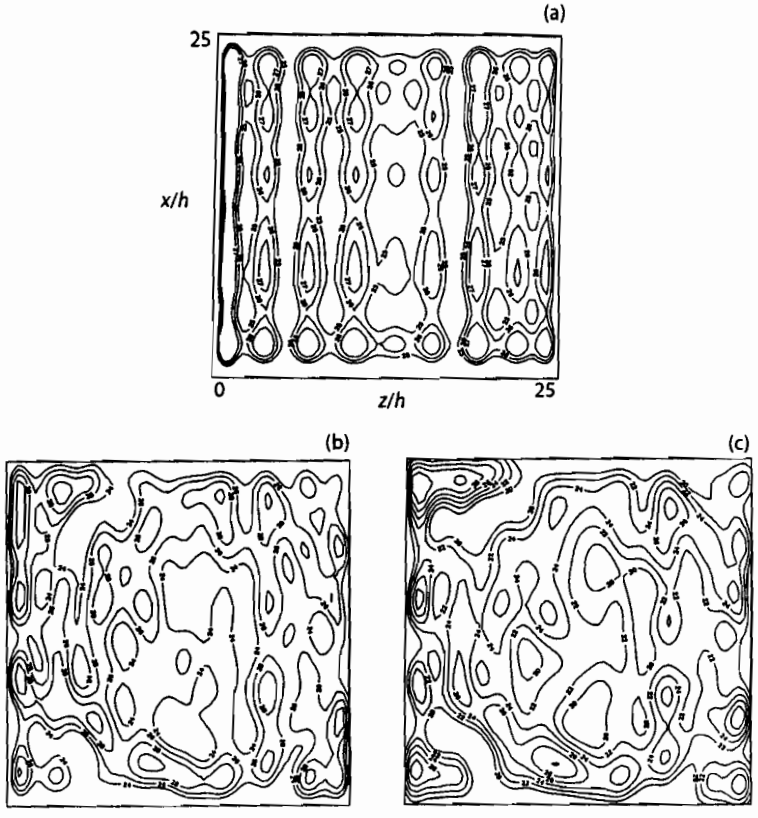

Figure 51 Isotherms on horizontal planes of the fluid layer, Ra = 13900. (a) 2-view $y/h = 0.85$, (b) 4-view $y/h = 0.85$, and (c) 4-view $y/h = 0.5$ tomography.

The temperature surfaces on three horizontal planes at which $y/h = 0.15$, 0.5, and 0.85 respectively, are shown in Figure 50. To preserve visual clarity, these surface plots have been partially filtered, without any noticeable loss of signal strength. The ordering of the horizontal planes is from the cooled top plate where $y = 1$. The nature of the temperature field is three-dimensional but is similar at all the three planes. One can see rolls spreading over the entire length of the cavity. While this is a qualitative trend, distortions can also be seen in the form of nonuniformity in roll width and straightness, and possible interference between neighboring rolls. These aspects are brought out in the isotherms over horizontal planes of the fluid layer (Figs. 51(a–c)). One can think of the isotherm patterns emerging from two-views (Fig. 51(a)) as the equivalent or the dominant trend, with other details surfacing from increasing view angles (see Natterer [88]). The patterns on two different planes obtained with the final set of four views (0°, 60°, 90°, and 150°) are shown in Figures 51(b–c). These figures have also been partially filtered for presentation. While

the unfiltered plots strictly satisfy the projection data (as in Fig. 49), the isotherms in Figure 51 are quite close. Hence, the resulting influence of the apparently three-dimensional flow field in Figures 51(b–c) is akin to longitudinal rolls. While Figures 51(b–c) show three-dimensionality in the flow field, the similarity in the geometry of isotherms suggests the formation of a stable structure in the fluid layer. The situation is analogous to chaotic convection superimposed on a set of stationary rolls observed by Gollub and Benson [126] at a Rayleigh number of 60000.

The local, the line-of-sight averaged (i.e., along a light ray) and the cavity-averaged Nusselt numbers have been computed at both the walls. The Nusselt number has been computed using the reconstructed field as well as the projection data. The average Nusselt number for the entire surface has been computed from the width-averaged temperature profile of the projection data. This corresponds to the slope of the S-shaped curve at the bounding planes (Fig. 47). The average Nusselt number at both plates has been reported for various angles of projection. The angular projections other than 0° and 90° do not include the entire width of the test cell, but it is expected that the average Nusselt number over the partial length will be representative of the entire width of the cavity. The average Nusselt number for each of the plates has also been compared with the experimental correlation reported by Gebhart et al. [89] in air, Equation (25).

A summary of all the Nusselt numbers referred to above is given in Table 15. The Nusselt numbers computed from interferometric measurements are within ±10% of the globally averaged value of 2.14. The individual plate-averaged Nusselt numbers are 2.16 and 2.12 as shown within brackets in Table 15. As stated earlier, interferometric projections at 30° and 120° were not utilized for reconstruction. The closeness of the average Nusselt numbers at these view angles with respect to other projections shows overall consistency in the measurements. The above equation gives a value of Nu = 2.59 at Ra = 13900. The Nusselt number obtained from the present set of experiments is thus approximately 17% below the Nusselt number based on the above correlation. The agreement is much closer at the higher Rayleigh number and is discussed later. Within experimental uncertainty, the comparison with previous experiments at the lower Rayleigh number may be taken to be favorable.

The temperature field derived from the interferograms suggest the formation of longitudinal rolls in the cavity. The presence of rolls can be deduced from the local

Table 15 Comparison of Average Nusselt Number with [89], Ra = 13900

Projection angle in degree	Nu (cold surface)	Nu (hot surface)	Nu (average) from all angles	Nu (reference)
0	2.18	1.94	2.12 (hot)	2.59
30	2.33	2.02	2.16 (cold)	
60	1.99	2.34	2.14 (cavity)	
90	2.00	2.17		
120	2.19	2.32		
150	2.27	1.95		

Nusselt number variation with distance. When the local Nusselt number is computed from the projection data, the value corresponding to the average computed along the light ray within the test cell is obtained. These line-of-sight Nusselt numbers are averaged along the direction of the light ray and are shown in Figure 52 for various projections angles for the top and the bottom plates. The rolls being parallel to the x-axis, the line-averaged Nusselt number along the z-axis that is the 0° projection is expected to show similar trends over both the walls. This is evident in Figure 52(a), where except for a small part of the test cell towards the ends, the local hot and cold wall Nusselt numbers are similar. Along the x-axis, that is the 90° projection, the local Nusselt numbers at the two walls are expected to show a phase shift. This corresponds to the inclination of the major axis of the roll cross-section with respect to the vertical direction. This shift is seen in Figure 52(b). Hence in a qualitative sense the variation of the line-averaged Nusselt number over the two plates supports the equivalent flow pattern in the cavity to be in the form of longitudinal rolls. The local Nusselt number along the direction of the 0° projection angle shows definite variations with distance. This suggests three-dimensionality in the longitudinal rolls which are no longer two-dimensional at the Rayleigh number studied. The loss of

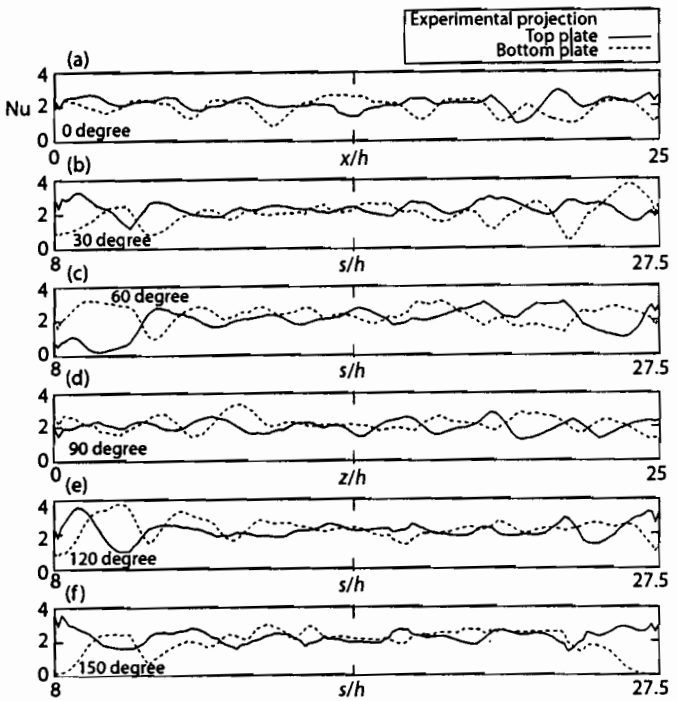

Figure 52 Experimentally obtained line-integrals of Nusselt numbers for both the walls, Ra = 13900, (a) 0°, (b) 30°, (c) 60°, (d) 90°, (e) 120°, (f) 150° projections.

two-dimensional structure in the rolls can also be confirmed from other projections (Figs. 52(c)–52(f)). Since the rolls identified in the projection data are parallel to the x-axis, projections symmetric with respect to the 90° axis will be identical at the limit of strict two-dimensionality. A comparison of projections obtained from symmetrically placed angles, namely (30, 150) and (60, 120) shows qualitative similarity. This strengthens the suggestion of rolls, but also highlights their unequal sizes and their three-dimensional nature along the roll axis.

The Nusselt number surface obtained from the reconstructed temperature field is shown for each of the hot and cold surfaces in Figure 53. Along the roll axis, the Nusselt number surfaces of the top and bottom plates are oppositely oriented. Heat transfer from the lower to the top plate by a buoyancy-driven roll is associated with the peaks and valleys of the Nusselt number surface.

Convection at Ra = 40200. Analysis of results from the experiments at a Rayleigh number of 40200 are presented next. In the higher Rayleigh number experiment, formation of a hot buoyant plume arising from the bottom plate and advancing towards the cold top plate has been observed. Since the discussion is based on two views, structures referred to below are to be interpreted as representative of the flow field. The temperature surfaces, namely the temperature variation over horizontal planes, are shown in Figure 54. Three horizontal planes, namely $y/h = 0.15$, 0.5, and 0.85, have been considered. A clearer picture emerges when isotherms at the corresponding planes over an assembly of four adjacent cells are examined. This is shown in Figure 55. Here, each cell corresponds to the portion of the cavity reconstructed from the interferograms. On assembly, the collection of temperature surfaces over the three planes clearly shows the structure of a rising plume. The repeating roll-like structure seen from both the 0° and 90° view angles suggests that a cubic cell exists inside the cavity. Mukutmoni and Yang [102] have shown the formation of an oscil-

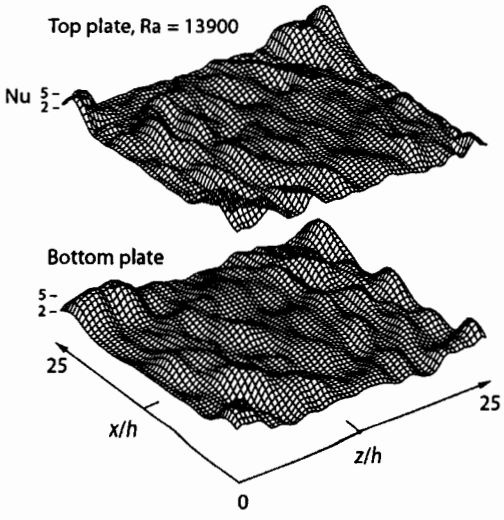

Figure 53 Nusselt number surfaces for top and bottom walls, Ra = 13900.

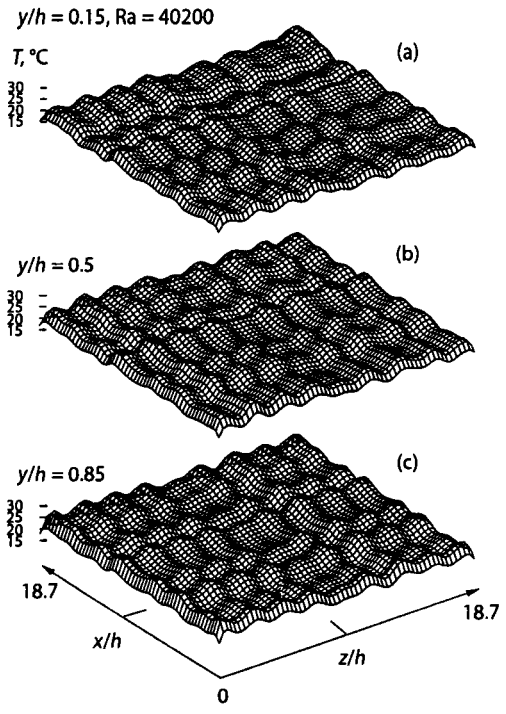

Figure 54 Temperature surfaces in the cavity at three horizontal planes, Ra = 40200, (a) $y/h = 0.15$, (b) $y/h = 0.5$, (c) $y/h = 0.85$.

latory polygonal planform structure for intermediate aspect ratio boxes for a fluid of Prandtl number equal to 3.5 at a Rayleigh number of 24000. The present observation that flow organizes in the form of cubic cells in the cavity is similar to their conclusion. It is also in agreement with the authors' previous study based on partial projection data with two view angles [79].

Figure 55 shows that the size of the heated region increases as one moves towards the heated lower wall. The buoyant plume rises from the center of the cluster of four adjacent repeated cubic cells. Each cubic cell can be visualized as being divided along its diagonal plane with high- and low-bulk-fluid temperatures on each side. Thus, the fluid rising along the center descends uniformly around the plume in the four quadrants. The assembly of four cells encloses a set of four rolls, all of which raise hot fluid jointly along the central vertical axis, which after being cooled, descends all around towards the lower surface. While it is possible to identify a cubic cell that is isolated from a thermal viewpoint (for example from the interferograms), it should be noted that the associated velocity field need not be isolated. In fact, the velocity fields in individual cubic cells will interact and an orderly pattern for flow can be discerned only over a collection of cells.

A flow model that integrates all aspects of the temperature contours is shown in a schematic diagram in Figure 56. This figure shows the hot mass of fluid rising in the form of a buoyant fountain from the center of the four adjacent cubic cells and dis-

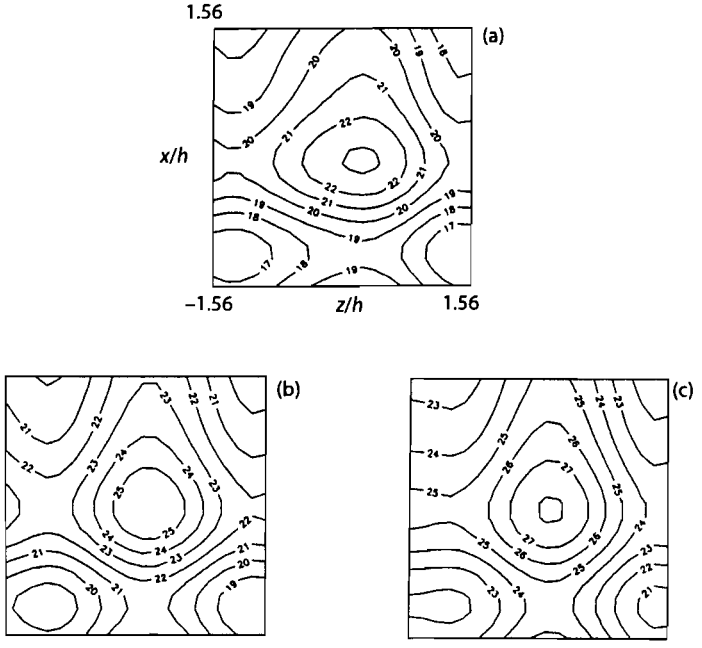

Figure 55 Isotherms in the cavity at three horizontal planes, Ra = 40200, (a) $y/h = 0.15$, (b) $y/h = 0.5$, (c) $y/h = 0.85$.

tributing the cold fluid in the four quadrants from above, almost symmetrically. When viewed from any direction this flow field will show a roll-like repeating structure. The plume cross-section is not seen to be of any definite shape, but is closer to an ellipse than a circle. This is simply because the cubic cell has unequal edges.

At a Rayleigh number of 40200, the average dimensionless wave-number of the dominant roll-pattern was found to be 2.52. The stability diagram of Busse and Clever [118] does not extend beyond Ra = 20000. However, an examination of the stability diagram for Pr = 7 (water) is possible though it is known that a higher Prandtl number has a stabilizing effect. The point Ra = 40200 and $\gamma = 2.52$ falls very close to the cross-roll stability boundary. The corresponding shadowgraph images are vividly shown by Busse and Clever [118], and Nasuno et al. [117].

The work of Busse and Clever [118] shows that the approach to cross-rolls in water is via skewed varicose and knot instabilities as the Rayleigh number is raised. In contrast, at Pr = 0.7 the sequence is skewed varicose, oscillatory, and with knot instabilities, but no data is really available for Ra > 15000. As discussed below, Lipps [127] has shown the formation of (semi) cross-rolls at Ra = 25000 in a small aspect ratio fluid layer. The formation of cubic cells as a dominant pattern, and a switch between this pattern and longitudinal rolls have been observed at Ra = 40200 in the present experiments. This suggests that the boundaries of the oscillatory, knot,

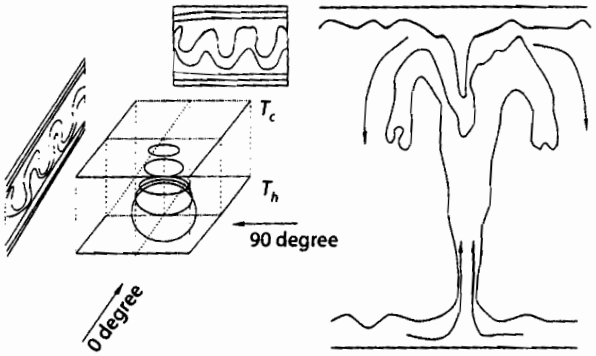

Figure 56 Schematic of the cubic cells and rising plume inside the cavity.

and cross-roll regimes (when extended) should be in the vicinity of this Rayleigh number in air. As in the case with Ra = 13900, one cannot comment on the route followed in the present experiments by the flow field to attain its final state on the stability diagram.

The analysis of the temperature field reported in the present study is based on the dominant fringe patterns. It was not possible to capture the momentary appearance of the secondary mode, but a visual examination showed it to be straight fringes, and hence equivalent to a longitudinal roll. The estimated time scale involved in the problem was estimated to be around ten seconds, corresponding to a frequency of 0.1 Hz and a Fourier number ($\alpha t/h^2$) of 0.25. Frequencies of a similar order of magnitude have been reported by Gollub and Benson [126] in their LDV study of RB convection at Rayleigh numbers up to 100 times the critical Rayleigh number for the onset of convection.

The experimental results are compared next with those of Lipps [127]. This is a numerical study of Rayleigh–Benard convection in air over the range $4000 < Ra < 25000$. The comparison is between the present experiments at Ra = 40200 (aspect ratio = 18) and the numerical predictions at Ra = 25000 (aspect ratio = 5–6). Thus the comparison is at best qualitative. Lipps [127] has reported time-dependent oscillations in the fluid layer whose characteristic time scales are position dependent. On the midplane of the fluid layer, this was in the range $0.05 < \tau < 0.2$. The mean flow itself had a periodicity of $\tau \approx 1.3$. The corresponding number for the present experiments based on visual judgement was 0.25, as mentioned in the previous paragraph. Despite this difference, typical isotherms shown by Lipps [127] are remarkably similar to the interferograms recorded in the experiments. Numerical calculations do not reveal plume formation, and instead, the author has identified a tongue-like structure spreading in the horizontal plane.

Lipps [127] has reported the appearance of a dominant flow pattern in the shape of a (semi) cross-roll followed by a disturbed flow regime, and the time scale for the

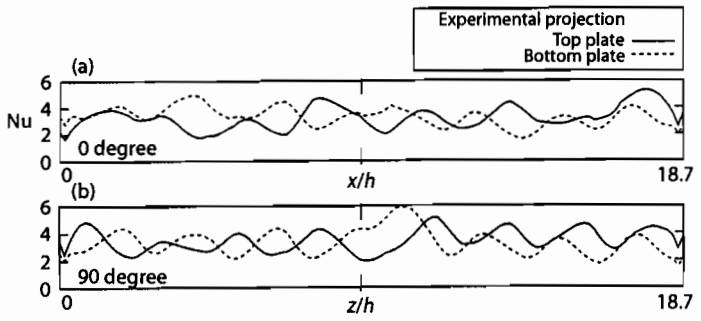

Figure 57 Experimentally obtained line-integrals of Nusselt numbers for both the Walls, Ra = 40200, (a) 0°, (b) 90° projections.

switch-over was $\tau = 1.3$. This result has a definite similarity with the experiments of the present study, in which the switching phenomenon has been reported. The time scale seen in the experiments (= 0.25) is smaller than 1.3, but can be explained as being due to

(a) a higher Rayleigh number which tends to lower the time scales, and

(b) a higher aspect ratio which can activate a whole range of wave numbers including small ones thus causing a lowering of τ.

Results for the Nusselt number at a Rayleigh number of 40200 are presented next. The Nusselt numbers averaged over the entire surface are given in Table 16. These have been compared with the correlation of Gebhart et al. [89] given above. The agreement between the Nusselt numbers of the present work and the correlation can be seen to be close. Specifically, the Nusselt number computed from the present set of experiments is within 1.5% of the empirical correlation.

The variation of the line-of-sight averaged Nusselt number with distance closely reflects the flow pattern in the cavity. As in the case of the lower Rayleigh number, these have been computed directly from the interferograms and are shown in Figure 57. Both 0° and 90° projections have been presented. A roll-like structure can be seen from both view angles and so the Nusselt number variation is expected to be oppositely oriented for the two active surfaces. This result is clearly brought out in Figure 57. The line-of-sight averaged Nusselt numbers were also computed from the reconstructed (fully three-dimensional) temperature field. The comparison between the reconstructed and the original local Nusselt numbers is presented in Figure 58. For the 0° and 90° view angles that have been employed in reconstruction, the comparison for both surfaces is excellent. The Nusselt number surfaces over the two bounding planes are shown in Figure 59. These surfaces are clearly oppositely oriented at the hot and cold walls. This confirms that when visualized from any angle, the resulting fringe pattern will be a roll-like repeating structure. It strengthens the suggestion made earlier that the flow field is in the form of a buoyant plume.

Table 16 Comparison of Average Nusselt Number with [89], Ra = 40200

Projection angle in degree	Nu (cold surface)	Nu (hot surface)	Nu (average) from all angles	Nu (reference)
0	3.22	3.30	3.32	3.28
90	3.48	3.30		

7.3.9 Closure. A three-dimensional temperature field in a differentially heated horizontal fluid layer has been reconstructed from its interferometric projections. Two different Rayleigh numbers namely 13900 and 40200, have been considered. The tomographic reconstruction technique that has been employed is AVMART. The algorithm converged without ambiguity to the final solution and did not display excessive sensitivity to the initial guess, relaxation factor, and noise in experimental data. The reconstructed field was seen to be fully consistent with the projection data. The reconstructed field was also seen to be in good agreement with the projection recorded, but not used in the tomographic algorithm. The three-dimensional field was seen to satisfy energy balance checks. The cavity-averaged Nusselt number computed from the interferometric projections was seen to be in reasonable agreement with published correlations.

At a Rayleigh number of 13900, the fringes were seen to be steady near the bounding walls, but mild unsteadiness was observed in the central horizontal layers. At the

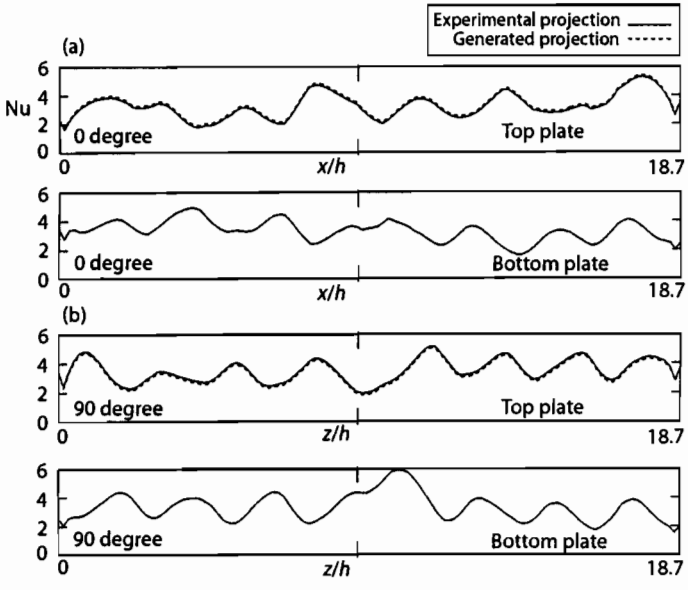

Figure 58 Comparison of experimentally obtained line-integrals of Nusselt numbers with generated line-integrals of Nusselt numbers, Ra = 40200, (a) 0°, (b) 90° projections.

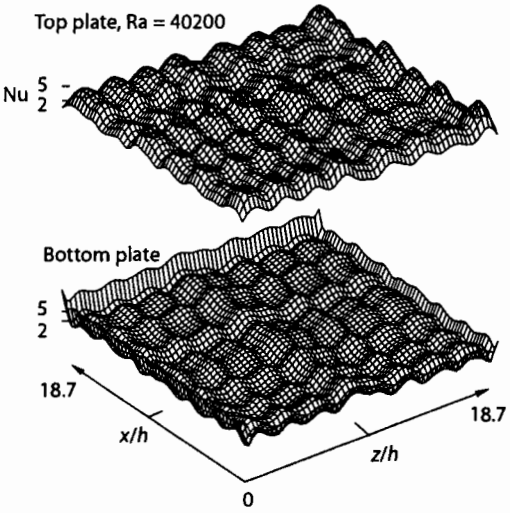

Figure 59 Nusselt number surfaces for top and bottom walls, Ra = 40200.

higher Rayleigh number of 40200, the unsteadiness was more pronounced, with flow switching between two well-defined states. The interferograms corresponding to the dominant mode have been recorded and analyzed in the present work.

At a Rayleigh number of 13900, the flow field was seen to be organized in the form of a three-dimensional structure. A two-view tomographic calculation showed a set of longitudinal rolls as a dominant pattern in the fluid layer. The rolls could be identified from the projection data. The number of rolls was smaller than that based on the aspect ratio consideration. The roll also displayed three-dimensionality along its axis. At a Rayleigh number of 40200, the thermal field was determined by cube-like cells that were spread all over the cavity. A collection of four cubic-cells was found to reveal a centrally located buoyancy-driven thermal plume rising from the hot plate and descending around it from the cold wall. The variation of the line-of-sight averaged Nusselt number as a function of a wall coordinate at each of the hot and cold surfaces was seen to be consistent with the proposed flow models.

8 CLOSING REMARKS

Mapping of thermal fields in fluids by interferometry has been described in the present article. By interpreting the interferograms as path integrals of the field variable, it has been shown that the three-dimensional field can be reconstructed using principles of tomography. Iterative algorithms based on the ART family have been found to be suitable for this purpose. Experimental results for buoyancy-driven convection in three configurations namely, a protruding heater, a two-dimensional square cavity, and a differentially heated horizontal fluid layer have been presented.

Interferometric tomography has good potential for applications to problems of far greater complexity. Examples are: (1) fully unsteady three-dimensional flow, (2) simultaneous reconstruction of fluid-fluid interfaces along with the temperature variation over them, (3) strongly refracting thermal fields where the reconstruction has to be performed with integrals evaluated over space curves, and (4) monitoring the growth of laser crystals from an aqueous solution by controlling the prevailing thermal fields. There is also the possibility of recovering the velocity field in the fluid medium from the complete temperature data. With advances being made in improving the spatial resolution and recording speed beyond video rates, it is now conceivable that interferometric tomography can be used to analyze turbulence structures, for example in buoyant flows, jets, and chemically reacting fluids. Color interferometry is a promising tool to improve spatial resolution since fringes will form corresponding to each wavelength of the laser (this approach has not been reported in the literature). Tomography by itself is a versatile tool to analyze data recorded by other measurement strategies that do not rely on changes in the refractive index. Projection data for example, can also be generated by reflection, absorption, and attenuation mechanisms.

Of great practical utility would be the extension of laser tomography to field-scale problems. Optical elements are needed here mainly to generate the projection data. Thus a field-scale problem is characterized by a large volume of data and the processing reduces to purely a numerical challenge. This aspect will be resolved with further improvements in computer technology. The use of lasers to process satellite images, and in turn provide a reference input to weather prediction codes, is an application that can deliver significant benefits to the society.

ACKNOWLEDGEMENTS

I thank Professor Prabhat Munshi for valuable discussions on tomography, and Dr. Debasish Mishra for being involved in a close technical collaboration. I acknowledge the assistance rendered by Mr. Sunil Verma for the literature on crystal growth from an aqueous solution. Part of the research reported in this article was financially supported by the Department of Science and Technology, New Delhi, India.

REFERENCES

1. W. Hauf and U. Grigull, Optical Methods in Heat Transfer, in J. P. Hartnett and T. F. Irvine Jr., (ed.), *Advances in Heat Transfer*, Vol. 6, pp. 134–362, 1970.
2. T. Y. Chu and R. J. Goldstein, Turbulent Convection in a Horizontal Layer of Water, *J. of Fluid Mechanics*, Vol. 60, pp. 141–159, 1973.
3. W. T. Lewis, F. P. Incropera, and R. Viskanta, Interferometric Study of Stable Salinity Gradients Heated from Below or Cooled from Below, *J. Fluid Mechanics*, Vol. 116, pp. 411–430, 1982.
4. R. J. Goldstein (Ed.), *Fluid Mechanics Measurements*, Hemisphere Publishing Corporation, New York, 1983; 2nd ed. 1996.

5. W. Lauterborn and A. Vogel, Modern Optical Techniques in Fluid Mechanics, in *Annual Review Fluid Mechanics*, Vol. 16, pp. 223–244, 1984.
6. F. Mayinger, Image-Forming Optical Techniques in Heat Transfer: revival by Computer-Aided Data Processing, *ASME J. Heat Transfer*, Vol. 115, pp. 824–834, 1993.
7. F. Mayinger (Ed.), *Optical Measurements: Techniques and Applications*, Springer-Verlag, Berlin, 1994.
8. A. K. Tolpadi and T. H. Kuehn, Measurement of Three-Dimensional Temperature Fields in Conjugate Conduction-Convection Problems Using Multidimensional Interferometry, *Int. J. Heat Mass Transfer*, Vol. 34-7, pp. 1733–1745, 1991.
9. D. Naylor and J. D. Tarasuk, Digital Image Processing of Interferograms for Local Convective Heat Transfer Measurements, *Proceedings of the 4th World Congress on Experimental Heat Transfer, Fluid Mechanics and Thermodynamics*, pp. 1609–1614, 1993.
10. K. Muralidhar, V. B. Patil, and R. Kashyap, Interferometric Study of Transient Convection in a Square Cavity, *J. of Flow Visualization and Image Processing*, Vol. 2-4, pp. 321–333, 1995.
11. H. H. Bartels-Lehnoff, P. H. Baumann, B. Bretthauer, and G. E. Meier, Computer-aided Evaluation of Interferograms, *Experiments in Fluids*, Vol. 16, pp. 46–53, 1993.
12. M. S. Chandrasekhara, D. D. Squires, M. C. Wilder, and L. W. Carr, A Phase-locked High-speed Real-time Interferometry System for Large Amplitude Unsteady Flows, *Experiments in Fluids*, Vol. 20, pp. 61–67, 1995.
13. S. Zhong and L. C. Squire, An Interferometric Study of Organized Structures in Wakes of Circular Cylinders, *Experiments in Fluids*, Vol. 20, pp. 91–99, 1995.
14. O. Dupont, J. L. Dewandel, and J. C. Legros, Use of Electronic Speckle Pattern Interferometry for Temperature Distribution Measurements through Liquids, *Optics Letters*, Vol. 20-17, 1995.
15. G. Dietz and I. Balkowski, Interferometry and Reconstruction of Strongly Refracting Fields in Two-dimensional Boundary-Layer Flow, *Experiments in Fluids*, Vol. 22, pp. 423–431, 1997.
16. M. Lehner and D. Mewes, *Applied Optical Measurements*, Springer-Verlag, Berlin, 1999.
17. J. A. Aparicio, J. L. Molpeceres, A. M. de Frutos, C. de Castro, and F. A. Frechoso, Improved Algorithm for the Analysis of Holographic Interferograms, *Optical Eng.*, Vol. 32-5, pp. 963–969, 1993.
18. R. D. Matukla and D. J. Collins, Determination of Three-dimensional Density Fields from Holographic Interferograms, *J. Applied Physics*, Vol. 42-1, pp. 1109–1119, 1971.
19. M. D. Shattuck, R. P. Behringer, G. A. Johnson, and J. G. Georgiadis, Onset and Stability of Convection in Porous Media: Visualization by Magnetic Resonance Imaging, *Physical Review Letters*, Vol. 75-10, pp. 1934–1937, 1995.
20. T. L. Spatz and D. Poulikakos, Holographic Interferometry Experiments on the Growth of Ice from a Horizontal Pipe, *Int. J. Heat Mass Trans.*, Vol. 34-7, pp. 1847–1859, 1991.
21. Y. B. Shen and D. Poulikakos, Real-Time Microholography for In Situ Concentration Measurements in the Vicinity of Growing Dendrites, *ASME J. of Heat Transfer*, Vol. 118, pp. 249–255, 1996.
22. H. Beer, *Interferometry and Holography in Nucleate Boiling*, in *Boiling Phenomena*, S. V. Stralen and R. Cole (eds.), pp. 821–843, Hemisphere Publishing Corp., New York, 1976.
23. R. E. Faw and T. A. Dullforce, Holographic Interferometry Measurement of Convective Heat Transport Beneath a Heated Horizontal Plate in Air, *Int. J. Heat Mass Transfer*, Vol. 24-5, pp. 859–869, 1981.

24. W. Ostendorf, F. Mayinger, and D. Mewes, A Tomographical Method using Holographic Interferometry for the Registration of Three Dimensional Unsteady Temperature Profiles in laminar and Turbulent Flow, *Proc. of the 8th Int. Heat Transfer Conference*, held at San Francisco, USA, pp. 519–523, 1986.
25. S. Bahl and J. A. Liburdy, Measurement of Local Convective Heat Transfer Coefficients using Three-dimensional Interferometry, *Int. J. Heat Mass Transfer*, Vol. 34, pp. 949–960, 1991.
26. T. A. W. M. Lanen, Digital Holographic Interferometry in Flow Research, *Opt. Comm.*, Vol. 79, pp. 386–396, 1990.
27. T. A. W. M. Lanen, E. M. Houtman, and P. G. Bakker, Quantitative Comparison between Interferometric Measurements and Euler Computations for Supersonic Cone Flows, *AIAA J.*, Vol. 33, pp. 210–216, 1995.
28. G. T. Herman, *Image Reconstruction from Projections*, Academic Press, New York, 1980.
29. Y. Censor, Finite Series-Expansion Reconstruction Methods, Proceedings of the IEEE, Vol. 71-3, pp. 409–419, 1983.
30. S. F. Gull and T. J. Newton, Maximum Entropy Tomography, *Applied Optics*, Vol. 25, pp. 156–160, 1986.
31. D. Verhoeven, Multiplicative Algebraic Computed Tomography Algorithms for the Reconstruction of Multidirectional Interferometric Data, *Optical Engineering*, Vol. 32, pp. 410–419, 1993.
32. P. M. V. Subbarao, P. Munshi, and K. Muralidhar, Performance Evaluation of Iterative Tomographic Algorithms applied to Reconstruction of a Three-dimensional Temperature Field, *Numerical Heat Transfer B (Fundamentals)*, Vol. 31-3, pp. 347–372, 1997.
33. R. Snyder and L. Hesselink, High Speed Optical Tomography for Flow Visualization, *Applied Optics*, Vol. 24-23, 1985.
34. C. K. Zoltani, K. J. White, and F. A. Dibianca, Multichannel Flash *x*-ray Tomography of Microsecond Events, *Applied Optics*, Vol. 24-23, 1985.
35. A. F. Gmitro and G. R. Gindi, Computed Tomography Videography: an Electrooptical System for Video-Rate Image Reconstruction, *Applied Optics*, Vol. 24-23, 1985.
36. G. W. Faris and R. L. Byer, Three-Dimensional Beam Deflection Optical Tomography of a Supersonic Jet, *Applied Optics*, Vol. 27-24, pp. 5202–5212, 1988.
37. R. Snyder, Instantaneous Three-dimensional Optical Tomographic Measurements of Species Concentration in a Co-Flowing Jet, *Report No. SUDAAR 567*, Stanford University, USA, 1988.
38. T. C. Liu, W. Merzkirch, and K. Oberste-Lehn, Optical Tomography Applied to Speckle Photographic Measurement of Asymmetric Flows with Variable Density, *Experiments in Fluids*, Vol. 7, pp. 157–163, 1989.
39. D. W. Watt and C. M. Vest, Turbulent Flow Visualization by Interferometric Integral Imaging and Computed Tomography, *Experiments in Fluids*, Vol. 8, pp. 301–311, 1990.
40. D. Mewes, M. Friedrich, W. Haarde, and W. Ostendorf, N. P. Cheremisinoff (ed.), Tomographic Measurement Techniques for Process Engineering Studies, Chapter 24, Vol. 3, Handbook of Heat and Mass Transfer, 1990.
41. Y. C. Michael and K. T. Yang, Three-Dimensional Mach–Zehnder Interferometric Tomography of the Rayleigh–Benard Problem, *ASME J. Heat Transfer*, Vol. 114, pp. 622–629, 1992.
42. S. Bahl and J. A. Liburdy, Three-Dimensional Image Reconstruction Using Interferometric Data from a Limited Field of View with Noise, *Applied Optics*, Vol. 30-29, pp. 4218–4226, 1991.
43. C. Soller, R. Wenskus, P. Middendorf, G. E. A. Meier, and F. Obermeier, Interferometric Tomography for Flow Visualization of Density Fields in Supersonic Jets and Convective Flow, *Applied Optics*, Vol. 33-14, pp. 2921–2932, 1994.

44. S. Sato and T. Kumakura, Interferometric Tomography Measurement of Spatial Temperature Profiles in Pre-mixed Flame (Application of Dual Plate Fourier Transform Interferometry), *Trans. of JSME*, Vol. 62-604, pp. 4241–4247, 1996 (in Japanese).
45. A. R. Verma, *Crystal Growth and Dislocations*, Butterworth, London, 1953.
46. I. Sunagawa, Studies of Crystal Surfaces, *Miner. Soc. America*, Sp. Paper 1, pp. 258–266, 1963.
47. I. Sunagawa, Morphology of Natural and Synthetic Diamond Crystal, in *Materials Science of the Earth's Interior*, Ed. I. Sunagawa, Terra Sci. Pub./D. Reidel, Tokyo/Dordrecht, pp. 303–330, 1984.
48. P. Bennema, J. P. van der Eerden, W. J. P. van Enckevort, B. van der Hoek, and K. Tsukamoto, Observation and Interpretation of Spirals for Spiral Growth from the Liquid State, *Phys. Stat. Sol.* (a), Vol. 55, p. 403, 1979.
49. K. Tsukamoto, In Situ Observation of Mono-Molecular Growth Steps on Crystals Growing in Aqueous Solution-I, *JCG*, Vol. 61, pp. 199–209, 1983.
50. K. Tsukamoto and I. Sunagawa, In Situ Observation of Mono-Molecular Growth Steps on Crystals Growing in Aqueous Solution-II. Specially Designed Objective Lens and Nomarski Prism for In Situ Observation by Reflected Light, *JCG*, Vol. 71, pp. 183–190, 1985.
51. K. Onuma, K. Tsukamoto, and I. Sunagawa, Role of Buoyancy Driven Convection in Aqueous Solution Growth: A Case Study of Barium Nitrate Crystals, *JCG*, Vol. 89, pp. 177–188, 1988.
52. K. Onuma, K. Tsukamoto, and I. Sunagawa, Effect of Buoyancy Driven Convection Upon the Surface Microtopographs of Barium Nirtate and Cadmium Iodide crystals, *JCG*, Vol. 98, pp. 384–390, 1989.
53. K. Onuma, K. Tsukamoto, and I. Sunagawa, Growth Kinetics of K-Alum Crystals in Relation to the Surface Supersaturations, *JCG*, Vol. 100, pp. 125–132, 1990.
54. K. Maiwa, K. Tsukamoto, and I. Sunagawa, Activities of Spiral Growth Hillocks on the (111) Faces of Barium Nitrate Crystals Growing in an Aqueous Solution, *JCG*, Vol. 102, pp. 43–53, 1990.
55. K. Onuma, K. Tsukamoto, and S. Nakadate, Application of Real Time Phase Shift Interferometer to the Measurement of Concentration Field, *JCG*, Vol. 129, pp. 706–718, 1993.
56. K. Onuma, T. Kameyama, and K. Tsukamoto, In Situ Study of Surface Phenomena by Real Time Phase Shift Interferometry, *JCG*, Vol. 137, pp. 610–622, 1994.
57. I. Sunagawa, K. Tsukamoto, K. Maiwa, and K. Onuma, Growth and Perfection of Crystals from Aqueous Solution: Case Studies on Barium Nitrate and K-Alum, *Prog. Crystal Growth and Charact.*, Vol. 30, pp. 153–190, 1995.
58. A. V. Bobylev and L. N. Rashkovich, An Interference Method of Measuring the Rates of Crystal Growth in Solution, and its Application to KH_2PO_4, *Sov. Phys. Crystallogr.*, Vol. 25-2, pp. 255–257, 1980.
59. L. N. Rashkovich, V. T. Leshchenko, and N. M. Sadykov, Growth Kinetics of TGS, *Sov. Phys. Crystallogr.*, Vol. 27-5, pp. 580–585, 1982.
60. L. N. Rashkovich, V. T. Leshchenko, A. T. Amandosov, and V. A. Koptsik, Interferometric Investigation of the Growth Rates of the 001 Faces of a Triglycine Sulphate Crystal at Various Supersaturations and Temperatures, *Sov. Phys. crystallogr.*, Vol. 28-4, pp. 454–458, 1983.
61. L. N. Rashkovich, A. A. Mkrtchyan, and A. A. Chernov, Optical Interference Investigation of Growth Morphology and Kinetics of (100) Face of ADP from Aqueous Solution, *Sov. Phys. crystallogr.*, Vol. 30-2, pp. 219–223, 1985.
62. L. N. Rashkovich and O. A. Shustin, New Optical Interference Methods for Studying the Kinetics of Crystallization in Solution, *Sov. Phys. Usp.*, Vol. 30-3, pp. 280–283, 1987.

63. L. N. Rashkovich and B. Y. Shekunov, Hydrodynamic Effects in Growth of ADP and KDP Crystals in Solution. I. Growth Kinetics, *Sov. Phys. Crystallogr.*, Vol. 35-1, pp. 96–99, 1990.
64. L. N. Rashkovich, B. Y. Shekunov, and Y. G. Kuznetsov, Hydrodynamic Effects in Growth of ADP and KDP Crystals in Solution. II. Morphological Stability of Faces, *Sov. Phys. Crystallogr.*, Vol. 35-1, pp. 99–102, 1990.
65. Y. G. Kuznetsov, A. A. Chernov, P. G. Vekilov, and I. L. Smol'skii, Kinetics of Growth of (101) Faces of KDP Crystals from Aqueous Solution, *Sov. Phys. Crystallogr.*, Vol. 32-4, pp. 584–587, 1987.
66. P. G. Vekilov and Y. G. Kuznetsov, Growth Kinetics Irregularities Due to Changed Dislocation Source Activity; (101) ADP Face, *JCG*, Vol. 119, pp. 248–260, 1992.
67. P. G. Vekilov, Elementary Processes of Protein Crystal Growth, *Prog. Crystal Growth and Charact.*, Vol. 26, pp. 25–49, 1993.
68. R. I. Ristic, J. N. Sherwood, and K. Wojciechowski, Assessment of the Strain in Small Sodium Chlorate Crystals and its Relation to Growth Rate Dispersion, *JCG*, Vol. 91, pp. 163–168, 1988.
69. R. I. Ristic, J. N. Sherwood, and K. Wojciechowski, The Assessment of Strain in Materials using Synchrotron Radiation Techniques and the Role of Strain in Growth Rate Dispersion, *J. Crystal Growth*, Vol. 144, pp. 87–90, 1994.
70. S. Kosugi, K. Maeno, and H. Honma, Measurement of Gas temperature Profile in Discharge Region of Excimer Laser with Laser Schlieren Method, *Jpn. J. Appl. Physics*, Vol. 32-3, pp. 4980–4986, 1993.
71. J. Koreeda, H. Yanagisawa, K. Maeno, H. Honma, S. A. Bystrov, V. I. Ivanov, and F. V. Shugaev, *Front Structures of Strong Shock waves in Air, Shock Waves*, pp. 263–268, 1995.
72. A. K. Agrawal, N. K. Butuk, R. G. Subramanyam, and G. DeVon, Three-Dimensional Rainbow Schlieren Tomography of a Temperature Field in Gas Flows, *Applied Optics*, Vol. 37-3, pp. 479–485, 1998.
73. S. A. Bystrov, H. Honma, V. I. Ivanov, J. Koreeda, K. Maeno, F. V. Shugaev, and H. Yanagisawa, Density Reconstruction from Laser Schlieren Signal in Shock Tube Experiments, *Shock Waves*, Vol. 8, pp. 183–189, 1998.
74. G. Brown and A. Roshko, On Density Effects and Large Structures in Turbulent Mixing Layers, *J. Fluid Mechanics*, Vol. 64, pp. 775–816, 1974.
75. M. Van Dyke, *An Album of Fluid Motion*, The Parabolic Press, California, 1982.
76. W. Schopf, J. C. Patterson, and A. M. H. Brooker, Evaluation of the Shadowgraph Method for the convective Flow in a Side-Heated Cavity, *Experiments in Fluids*, Vol. 21, pp. 331–340, 1996.
77. M. N. Darbhe and K. Muralidhar, Natural Convection Heat Transfer from a Discrete Protruding Surface, *Int. Communications in Heat and Mass Transfer*, Vol. 23-3, pp. 417–426, 1996.
78. D. Mishra, K. Muralidhar, and P. Munshi, Performance Evaluation of Fringe Thinning Algorithms for Interferometric Tomography, *Optics and Lasers in Engineering*, Vol. 30, pp. 229–249, 1998.
79. D. Mishra, K. Muralidhar, and P. Munshi, Interferometric Study of Rayleigh–Benard Convection using Tomography with Limited Projection Data, *Experimental Heat Transfer*, Vol. 12-2, pp. 117–136, 1999.
80. D. Mishra, K. Muralidhar, and P. Munshi, Isotherms in a Horizontal Differentially Heated Cavity at Intermediate Rayleigh Numbers, *International Communications in Heat and Mass Transfer*, Vol. 26-5, pp. 729–738, 1999.
81. D. Mishra, K. Muralidhar, and P. Munshi, A Robust MART Algorithm for Tomographic Applications, *Numerical Heat Transfer B (Fundamentals)*, Vol. 35-4, pp. 485–506, 1999.

82. D. Mishra, K. Muralidhar, and P. Munshi, Interferometric Study of Rayleigh–Benard Convection at Intermediate Rayleigh Numbers, *Fluid Dynamics Research*, Vol. 25-5, pp. 231–255, 1999.
83. D. W. Robinson, Automatic Fringe Analysis with a Computer Image-processing System, *Applied Optics*, Vol. 22-14, pp. 2169–2176, 1983.
84. S. Krishnaswamy, Algorithm for Computer Tracing of Interference Fringes, *Applied Optics*, Vol. 30-13, pp. 1624–1628, 1991.
85. K. Ramesh and R. P. Singh, Comparative Performance Evaluation of Various Fringe Thinning Algorithms in Photomechanics, *Electronic Imaging*, Vol. 4, pp. 71–83, 1995.
86. W. R. J. Funnell, Image Processing Applied to the Interactive Analysis of Interferometric Fringes, *Applied Optics*, Vol. 20-18, pp. 3245–3250, 1981.
87. R. C. Gonzalez and R. E. Woods, *Digital Image Processing*, Addison-Wesley Publishing Company, USA, 1993.
88. F. Natterer, *The Mathematics of Computerized Tomography*, John Wiley & Sons, New York, 1986.
89. B. Gebhart, Y. Jaluria, R. L. Mahajan, and B. Sammakia, *Buoyancy-Induced Flows and Transport*, Hemisphere Publishing Corporation, New York, 1988.
90. L. Lapidus and G. F. Pinder, *Numerical Solution of Partial Differential Equations in Science and Engineering*, John Wiley and Sons, New York, 1982.
91. B. P. Leonard and H. S. Niknafs, Sharp Monotonic Resolution of Discontinuities without Clipping of Narrow Extrema, *Computers and Fluids*, Vol. 19-1, pp. 141–154, 1991.
92. R. M. Lewitt, Reconstruction Algorithm-Transform Methods, *Proceedings of IEEE*, Vol. 71, pp. 390–408, 1983.
93. G. N. Ramachandran and A. V. Laxminarayanan, Three-Dimensional Reconstruction from Radiographs and Electron Micrographs: Application of Convolution instead of Fourier Transforms, *Proc. Nat.*, Acad. USA, Vol. 68, pp. 2236–2240, 1970.
94. P. Munshi, Application of Computerized Tomography for Measurements in Heat and Mass Transfer, *Proceedings of the 3rd ISHMT-ASME Heat and Mass Transfer Conference Held*, at IIT Kanpur (India) during 29–31 December 1997, Narosa Publishers, N. Delhi, 1997.
95. M. S. Kaczmarz, Angenaherte Auflosung Von Systemen Linearer Gleichungen, *Bull. Acad. Polonaise Sci. Lett. Classe Sci. Math. Natur. Serier*, Vol. A35, pp. 355–357, 1937.
96. K. Tanabe, Projection Method for Solving a Singular System, *Numerical Mathematics*, Vol. 17, pp. 302–214, 1971.
97. R. Gordon, R. Bender, and G. T. Herman, Algebraic Reconstruction Techniques (ART) for Three-dimensional Electron Microscopy and X-ray Photography, *J. of Theoretical Biology*, Vol. 29, pp. 471–481, 1970.
98. P. F. C. Gilbert, Iterative Methods for Three-dimensional reconstruction of an Object from its Projections, *J. Theoretical Biology*, Vol. 36, pp. 105–117, 1972.
99. A. H. Anderson and A. C. Kak, Simultaneous Algebraic Reconstruction technique (SART): a Superior Implementation of the ART Algorithm, *Ultrasonic Imaging*, Vol. 6, pp. 81–94, 1984.
100. R. Gordon and G. T. Herman, Three-dimensional Reconstructions from Projections: A Review of Algorithms, *Int. Rev. Crystallography*, Vol. 38, pp. 111–151, 1974.
101. K. Muralidhar and F. A. Kulacki, Stability of Mixed Convective Flow, *Int. J. Heat and Fluid Flow*, Vol. 8, pp. 228–234, 1987.
102. D. Mukutmoni and K. T. Yang, Pattern Selection for Rayleigh–Benard Convection in Intermediate Aspect Ratio Boxes, *Numerical Heat Transfer, Part A*, Vol. 27, pp. 621–637, 1995.

103. F. P. Incropera, Convetion Heat Transfer in Electronic Equipment Cooling, *ASME J. Heat Transfer*, Vol. 110, pp. 1097–1111, 1988.
104. S. V. Garimella and P. A. Eibeck, Heat Transfer Characteristics of an Array of Protruding Elements in Single Phase Forced Convection, *Int. J. Heat Mass Transfer*, Vol. 33, pp. 2659–2669, 1990.
105. K. A. Park and A. E. Bergles, Natural Convection Heat Transfer Characteristics of Simulated Microelectronic Chips, *ASME J. Heat Transfer*, Vol. 109, pp. 90–96, 1987.
106. B. H. Kang and Y. Jaluria, Natural Convection Heat Transfer Characteristics of a Protruding Thermal Source Located on Horizontal and Vertical Surfaces, *Int. J. Heat Mass Transfer*, Vol. 33, pp. 1347–1357, 1990.
107. T. Fujii and M. Fujii, The Dependence of Local Nusselt Number on Prandtl Number in the case of Free Convection along a Vertical Surface with Constant Heat Flux, *Int. J. Heat Mass Transfer*, Vol. 19, pp. 121–122, 1976.
108. K. M. Kelkar and D. Choudhary, Numerical Prediction of Periodically Fully Developed Natural Convection in a Vertical Channel with Surface Mounted Heat Generating Blocks, *Int. J. Heat Mass Transfer*, Vol. 36, pp. 1133–1145, 1993.
109. M. M. Yovanovich and K. Jafarpur, Models for Laminar Natural Convection from Vertical and Horizontal Isothermal Cuboids for all Prandtl numbers and Rayleigh Numbers below Ra, (Ed.) R. D. Boyd and P. G. Kroeger, Fundamentals of Natural Convection, *ASME-HTD*, Vol. 264, pp. 111, 1993.
110. E. R. G. Eckert and W. O. Carlson, Natural Convection in an Air Layer Enclosed between Two Vertical Plates with Different Temperatures, *Int. J. Heat and Mass Transfer*, Vol. 2, pp. 106–120, 1961.
111. T. H. Kuehn and R. J. Goldstein, An Experimental and Theoretical Study of Natural Convection in an Annulus between Horizontal Concentric Cylinders, *J. Fluid Mechanics*, Vol. 74, pp. 695–719, 1976.
112. D. M. Kim and R. Viskanta, Study of the Effects of Wall Conductance on Natural Convection in Differently Oriented Square Cavities, *J. Fluid Mechanics*, Vol. 144, pp. 153–176, 1984.
113. F. H. Busse, Transition to Turbulence in Rayleigh–Benard Convection in *Topics in Applied Physics, Hydrodynamic Instabilities and Transition to Turbulence*, Edited by Swinney H. L. and Gollub J. P., Springer-Verlag, Berlin, 1985.
114. J. K. Platten and J. C. Legros, *Convection in Liquids*, Springer-Verlag, Berlin, 1984.
115. I. Catton, The Effect of Insulating Vertical Walls on the Onset of Motion in a Fluid Heated from Below, *Int. J. Heat and Mass Transfer*, Vol. 15, pp. 665–672, 1972.
116. K. R. Kirchartz and H. Oertel (Jr.), Three-dimensional Thermal Cellular Convection in Rectangular Boxes, *J. of Fluid Mechanics*, Vol. 192, pp. 249–286, 1988.
117. S. Nasuno, M. Sano, and Y. Sawada, Saptial Instabilities and Onset of Chaos in Rayleigh–Benard System with Intermediate Aspect Ratio, *J. Physical Society of Japan*, Vol. 57, pp. 3357–3364, 1988.
118. F. H. Busse and R. M. Clever, Instabilities of Convection Rolls in a Fluid of Moderate Prandtl Number, *J. Fluid Mechanics*, Vol. 91, pp. 319–335, 1979.
119. G. Ahlers and R. P. Behringer, Evolution of Turbulence from Rayleigh–Benard Instability, *Phys. Rev. Lett.*, Vol. 40, pp. 712–716, 1978.
120. R. Krishnamurti, On the Transition to Turbulent Convection. Part 1: The Transition from Two To Three-dimensional Flow, *J. of Fluid Mechanics*, Vol. 42-2, Part 2, pp. 295–307, 1970.
121. R. Kessler, Nonlinear Transition in Three-Dimensional Convection, *J. of Fluid Mechanics*, Vol. 174, pp. 357–379, 1987.
122. R. Krishnamurti, On the Transition to Turbulent Convection. Part 2: The Transition to Time Dependent Flow, *J. of Fluid Mechanics*, Vol. 42-2, pp. 309–320, 1970.

123. D. Mukutmoni and K. T. Yang, Thermal Convection in Small Enclosures: An Atypical Bifurcation Sequence, *Int. J. of Heat and Mass Transfer*, Vol. 38-1, pp. 113–126, 1995.
124. P. Kolodner, R. W. Walden, A. Passner, and C. M. Surko, Rayleigh–Benard Convection in an Intermediate-Aspect-Ratio Rectangular Container, *J. of Fluid Mechanics*, Vol. 163, pp. 195–226, 1986.
125. J. G. Maveety and J. R. Leith, Heat Transfer in Rayleigh–Benard Convection with Air in Moderate Size Containers, *Int. J. Heat and Mass Transfer*, Vol. 41, pp. 785–796, 1998.
126. J. P. Gollub and S. V. Benson, Many Routes to Turbulent Convection, *J. Fluid Mechanics*, Vol. 100-3, pp. 449–470, 1980.
127. F. B. Lipps, Numerical Simulation of Three-Dimensional Benard Convection in Air, *J. Fluid Mechanics*, Vol. 75, pp. 113–148, 1976.